

World Renewable Energy Congress – Sweden

8–13 May, 2011
Linköping, Sweden

Editor

Professor Bahram Moshfegh

Copyright

The publishers will keep this document online on the Internet – or its possible replacement – from the date of publication barring exceptional circumstances.

The online availability of the document implies permanent permission for anyone to read, to download, or to print out single copies for his/her own use and to use it unchanged for non-commercial research and educational purposes. Subsequent transfers of copyright cannot revoke this permission. All other uses of the document are conditional upon the consent of the copyright owner. The publisher has taken technical and administrative measures to assure authenticity, security and accessibility.

According to intellectual property law, the author has the right to be mentioned when his/her work is accessed as described above and to be protected against infringement.

For additional information about Linköping University Electronic Press and its procedures for publication and for assurance of document integrity, please refer to its www home page: <http://www.ep.liu.se/>.

Linköping Electronic Conference Proceedings, 57
Linköping University Electronic Press
Linköping, Sweden, 2011

http://www.ep.liu.se/ecp_home/index.en.aspx?issue=057
ISBN: 978-91-7393-070-3
ISSN 1650-3740 (online)
ISSN 1650-3686 (print)

© The Authors

Volume 4

Fuel Cells

Table of Contents

Beyond the Simplicity: Optimizing the Hydrogen Production Process <i>Miguel A. Bernal Pampín, Laura Cristóbal Andrade and Pastora M. Bello Bugallo</i>	1135
The Effect of A Boron Oxide Layer on Hydrogen Production by Boron Hydrolysis <i>Tareq Abu Hamed, Bara Wahbeh and Roni Kasher</i>	1143
Case Study: Technical Assessment of the Efficiency Optimization in Direct Connected PV-Electrolysis System at Taleghan-Iran <i>Abolfazl Shiroudi, Seyed Reza Hosseini Taklimi and Nilofar Jafari</i>	1150
Demonstration Project of the Solar Hydrogen Energy System Located on Taleghan-Iran: Technical-Economic Assessments <i>Abolfazl Shiroud and Seyed Reza Hosseini Taklimi</i>	1158
Two Dimensional PEM Fuel Cell Modeling at Different Operation Voltages <i>Mohammad Ameri*, Pooria Oroojie</i>	1166
Effect of Type and Concentration of Substrate on Power Generation in a Dual Chambered Microbial Fuel Cell <i>A.A. Ghoreyshi, T.Jafary, G.D. Najafpour and F.Haghpourast</i>	1174
Bioelectricity Power Generation from Organic Substrate in a Microbial Fuel Cell Using Saccharomyces Cerevisiae as Biocatalysts <i>T. Jafary¹, G.D. Najafpour, A.A. Ghoreyshi, F. Haghparast, M. Rahimnejad and H. Zare</i>	1182
Performance and Economics of Low Cost Clay Cylinder Microbial Fuel Cell for Wastewater Treatment <i>Siva Rama Satyam B, Manaswini Behera and Makarand M. Ghangrekar</i>	1189
Development of Laccase and Manganese Peroxidase Biocathodes for Microbial Fuel Cell Applications <i>Sahar Bakhshian and Hamid-Reza Kariminia</i>	1197
Numerical Studies of PEM Fuel Cell with Serpentine Flow-Field for Sustainable Energy Use <i>Sang-Hoon Jang, GiSoo Shin, Hana Hwang, Kap-Seung Choi and, Hyung-Man Kim</i>	1205
Comparison of Three Anode Channel Configurations and Their Effects on DMFC Performance <i>S. SH. Khoshmanesh and S.Bordbar</i>	1211
Investigation of Electrical, Structural and Thermal Stability Properties of Cubic $(\text{Bi}_2\text{O}_3)_{1-x-y} (\text{Dy}_2\text{O}_3)_x (\text{Ho}_2\text{O}_3)_y$ Ternary System <i>Refik Kayali, Murivet Kasikci, Semra Durmus and Mehmet Ari</i>	1219
Alkaline Fuel Cell (AFC) Engineering Design, Modeling and Simulation for UPS Provide in Laboratory Application <i>L. Ariyanfar, H. Ghadamian and R. Roshandel</i>	1227

Beyond the simplicity: optimizing the hydrogen production process

Miguel A. Bernal Pampín, Laura Cristóbal Andrade, Pastora M. Bello Bugallo*

*Department of Chemical Engineering and Seminar of Renewable Energy (Aula de Energías Renovables),
University of Santiago de Compostela, Spain*

* Corresponding author. Tel: +34 881816757, Fax: +34981528050, E-mail: pastora.bello.bugallo@usc.es

Abstract: This paper presents the optimization of the consumption and production rates of a steam reforming plant using natural gas as raw material for generating hydrogen as principal product. Different strategies are applied to select the most adequate techniques and to obtain different configurations or alternatives for the process. The methodology used in this work includes both quantitative and qualitative analyses. The aim of this work is to apply various possible alternatives to control emissions and reduce energy inputs, according to the recommendations of the European IPPC Bureau and the United Nations Framework Convention on Climate Change. The actions are oriented towards reducing the consumption of the plant by improving process heat recovery and improving energy integration. The results will be focused on the energy consumption analysis for the different alternatives, showing the best option to design the plant, maximizing production and optimizing energy use. This approach produces large amounts of hydrogen, decreases environmental impacts and increases economical profits.

Keywords: Hydrogen production, Natural gas, Energy efficiency, Best Available Techniques

1. Introduction

The synthesis of hydrogen has been largely used to obtain ammonia and related derivatives. As a result of the growth of the industry during the last century, new processes and methods using hydrogen as raw material appeared. Some examples are Fischer-Tropsch processes, hydrogenation processes for the petrochemical industry, direct use of hydrogen as an energy vector, and others [1-6]. Nowadays this continuous improvement not only responds to compliance with the normative, but also to the demands and expectations of consumers. To get quality products at the lowest possible cost, it is necessary to implement optimization techniques that reduce material and energy use, taking advantage of the recent revolutionary technological changes related with energy optimization patterns. These technology advances can lead to more efficient processes that reduce energy use and pollutants emissions.

Environmental problems, such as global warming, may lead to restrictions on the use of energy in the near future. CO₂ emissions reduction goals can be achieved by introducing energy efficiency improvements in the production processes [7].

Hydrogen plants are major energy-demanding processes and important CO₂ releasers [1, 2, 8]. According to the latest surveys, the greenhouse gas emissions from the hydrogen industry were calculated to be around one hundred million tonnes CO₂ equivalent per year. In spite of that, this industry has already come a long way towards reducing energy use and related emissions by improving its performance.

An industrial sustainable system is characterized by minimal environmental exchanges, with a more rational use of the available resources. This implies the integrated reduction of the environmental impacts, acting over the effects derived from the activities (waste generation, air pollution, etc) and implementing measures related to resources exploitation and pollution prevention.

In this context the EU published in 1996 the IPPC Directive [9] (meaning Integrated Pollution Prevention and Control) that introduced, among others, the Best Available Techniques (BAT) and the Emission Limit Values (ELV) for the affected industrial potentially polluting sources.

On the other hand the United Nations created in 1988 the Intergovernmental Panel on Climate Change (IPCC). They published in 1996 the Kyoto Protocol fixing the objective of greenhouse gases reduction for the signatory countries. It includes the Clean Development Mechanisms, which enables developed countries to accredit units or credit emissions reduction when projects are financed in developing countries [10].

The world H₂ production is estimated to be around 45 million tonnes (500 million m³) per year. Around 96% of it is derived from fossil fuels. In 2000 crude oil was the dominant fossil fuel to produce H₂ (55%), followed by natural gas and coal. At present, 49% of the hydrogen is produced by reforming natural gas, 29% (Fig. 1).

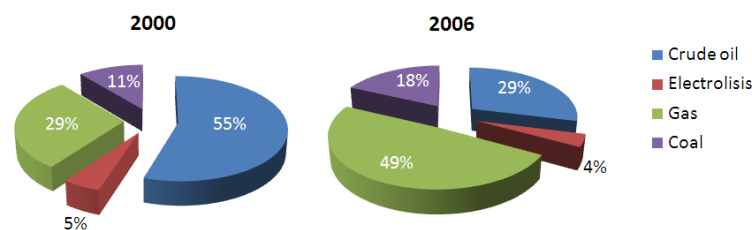


Fig. 1. Current worldwide H₂ production [11].

Natural gas has been selected as raw material in the steam reforming process as it is the least polluting alternative within the group of hydrocarbon feedstock. Comparatively, other processes consuming different raw materials have not been completely developed, so they imply high energy costs and show some technological limitations [6-8, 11, 12].

This paper presents the optimised design of a steam reforming plant using natural gas as raw material for producing hydrogen as principal product. Various possible alternatives are proposed to prevent and control emissions and reduce energy inputs. This work follows the recommendations of the European IPPC Bureau [13] and the United Nations Framework Convention on Climate Change [10].

2. Methodology

The methodology includes both quantitative and qualitative analyses that were developed and applied to meet the objectives of this work, which was oriented to prevent and control emissions and reduce energy demand in the case study. The qualitative analyses begins with a detailed description of the process, followed by the study of the main environmental impacts that leads to an inventory of the BAT, the evaluation of these techniques and finally the assessment of the possible improvements of the environmental performance of the plant achieved after the application of the selected techniques. On the other hand, quantitative analysis includes process modelling and simulation, solving material and energy balances for each configuration by using a process simulation tool, Aspen Plus HYSYS[®].

The qualitative and quantitative analyses carried out during this work were developed according to the sections included below.

2.1. Qualitative analysis

2.1.1. Detailed description of the process

In order to provide proper results, the process is divided into stages, including inputs and outputs of materials and energy (Fig. 2).

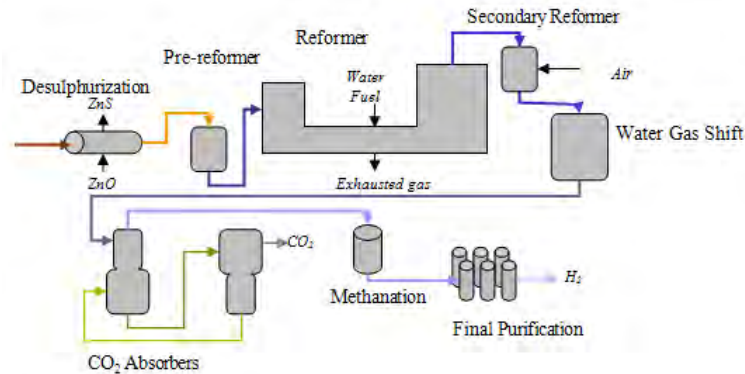


Fig. 2. Flow-sheet of the hydrogen production process.

2.1.2. Study of the main environmental impacts to be addressed by the process which can cause negative effects (atmospheric emissions, liquid effluents and solid wastes)

The reforming reaction is strongly endothermic so it is required a large input of heat, around 70%. Pumps and refrigeration from the CO₂ removal section account for 10% of the total energy needed [14]. Linked to the high-energy requirements, relevant greenhouse emissions are produced. For instance, within the hydrogen production field, the CO₂ generation from NH₃ production ranges from 1.52 to 3.06 t CO₂/t NH₃ produced [15]. On average, one-third of CO₂ emissions result from burning fuel and two-thirds from the use of hydrocarbon feedstock. Fig. 3 shows that energy consumption decreases with time in NH₃ plants.

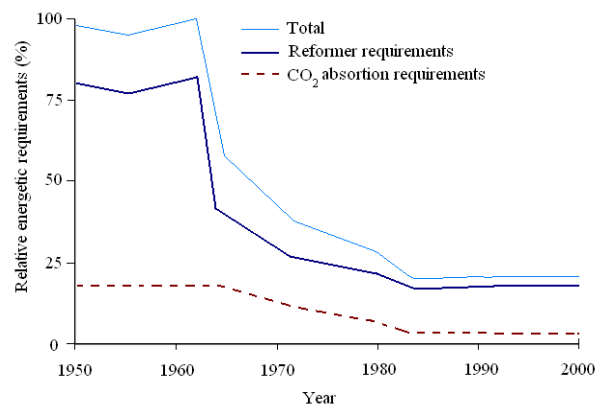


Fig. 3. Relative energy requirements as a function of time (adapted from [17]).

Due to the high temperatures of the combustion process, large amounts of NO_x are generated in the reformer and in the auxiliary boilers. The kind of burning fuel and the usage of hydrocarbon feedstock determine the quantity of SO_x emissions. Pollution problems related to water are associated to the formation of condensates or to the scrubbing of waste gases. Spent catalysts and molecular sieves are solid waste sources [16].

2.1.3. Inventory of BAT using different sources of background information available

The proposed techniques [18-23], which are candidate to be BAT for the analysed processes, are summarized in Fig. 4.

Stage	Techniques	Stage	Techniques
Reformer section	Selective Non-Catalytic Reduction (SNCR) at the primary reformer	Combustion	Burner regulation and control by monitoring and controlling fuel flow, air flow, oxygen levels and heat demand
	Low NOx burners		Proper furnace insulation to reduce wall heat losses (mid-term implementation)
	Pre-reforming		Clean heat transfer surfaces (short-term implementation)
	Extended preheating of the hydrocarbon/steam feed	Steam system	Pre-heat feed-water by using economisers
	Reduce steam-carbon ratio to 3.0		Reducing the amount of total dissolved solids in the boiler water to reduce blow down and energy loss (short-term implementation)
	Pre-heating of the combustion air with waste heat from the flue-gases going to the stack		Optimise deareator vent rate (mid-term implementation)
ATR system			
Converters	Pressure drop optimization of HTS and LTS converters	Heat recovery and cooling	Monitoring and maintenance of heat exchangers
CO ₂ removal system	Using MDEA technology	Pumping system	Control and maintenance
	PSA system		

Fig. 4. Inventory of the best available techniques.

2.1.4. Analysis of the previously reported measures

All the techniques are analysed in order to select those that are already implemented and those that are not, bearing in mind the improvement of global energy efficiency. To facilitate this task, a technical data sheet for each technique is done taking into account some of the items established by the EIPPCB [13]: technical description of the measure, benefits or environmental data, secondary effects, implementation, applicability and characterization.

2.1.5. Assessment of the possible environmental performance improvement of the plant by selected techniques.

After a careful evaluation of the understudy hydrogen plant, a retrofit was decided. According to the current methodology, a combination of the proposed measures is selected to assess the energy savings of the new flow-sheet. Thereby, in this paper the potentiality of the highlighted measures (Fig. 5.) is tested.

Stage	Techniques	Environmental achievements
Reformer section	T2.1 Extended pre-heating of the feed Reduction of steam/carbon ratio in the reformer feed Reduction of outlet temperature of the exhaust gases	Global energy savings Reduced NO _x emissions <200 mg/Nm ³
	T2.2 Pre-reforming	Energy reduction rates of 5-10% and energy savings
	T2.3 Pre-heating of combustion air	Energy savings
	T.ATR Substitution to ATR system	Total integration of the consumption
CO ₂ removal system	T.PSA Substitution to PSA system	Total saving of the energy consumed in absorption

Fig.5. Techniques selected for the reformer section.

2.2. Quantitative analysis

Aspen HYSYS 7.1 has been used to model the process in order to compare different possible configurations. The improvement of the process has been done progressively (Fig. 6). Once the model is ready (the base case and the retrofit), several simulations are carried out to obtain the main parameters of the equipment and flows.

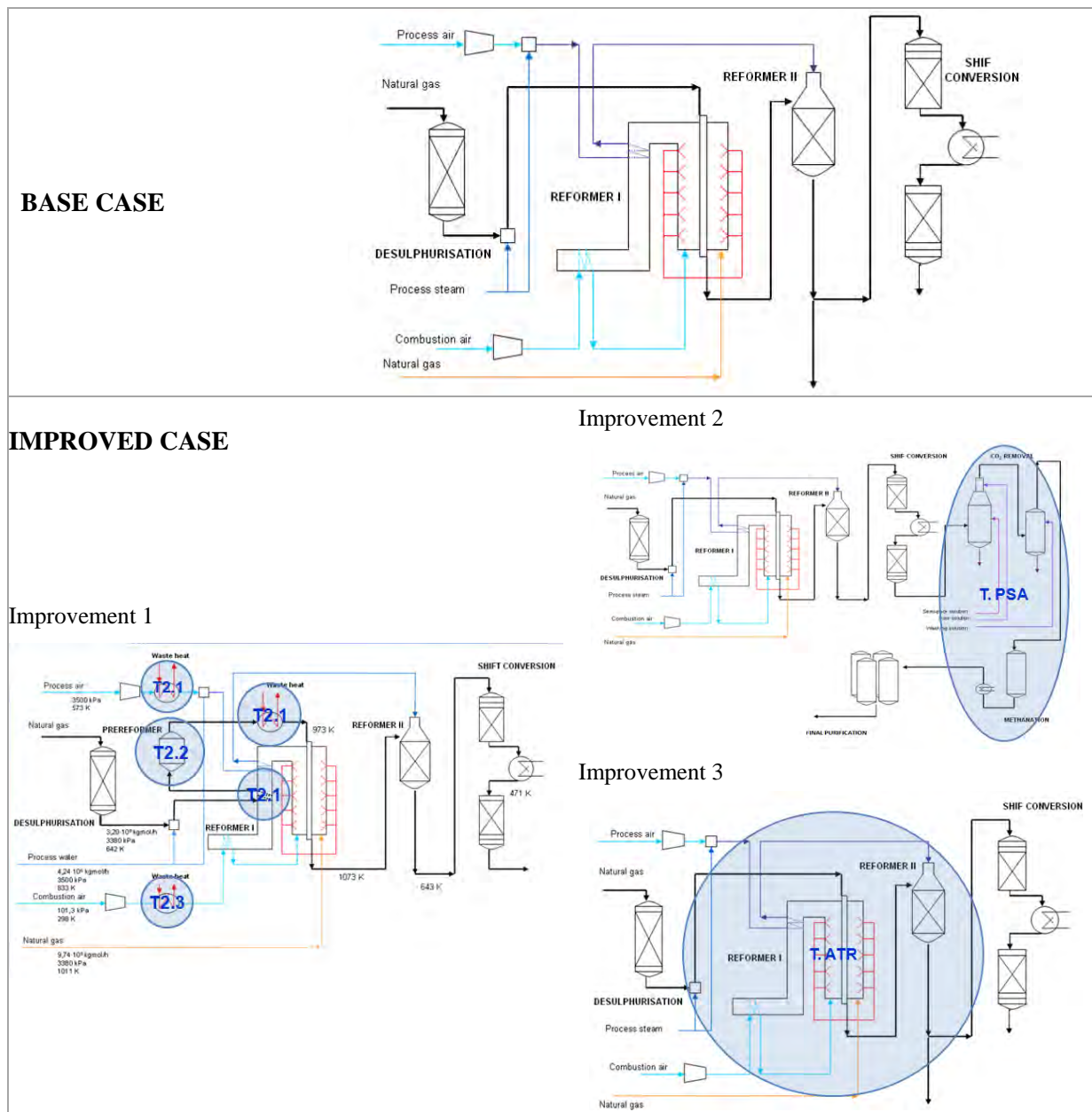


Fig. 6. Comparison of the base case with the improved case.

3. Results

Simulation results show that energy can be saved by implementing the selected techniques. The implementation of a pre-reforming reduces more than 10% the required energy input. Moreover, energy consumption is reduced 21.5%, regarding the base case, by implementing preheating of combustion air (Table 1). The final substitution of the purification stage by the PSA eliminates de energy requirements of the absorption stage (Table 2).

Table 1. Energy savings in the reforming section

Technique	Energy required in the reforming section	
	Before implementation	After implementation
T 2.2. Pre-reforming	107.2 MW	95.8 MW
T 2.3. Pre-heating of combustion air	95.8 MW	84.2 MW

Table 2. Energy savings in the purification section

Technique	Energy required in the purification section
T PSA. Substitution to PSA tech	5,000 MJ/t CO ₂ saved by eliminating absorption stage

Besides these data, Fig. 7 shows how energy consumption in the plant decreases by the progressive implementation of the selected techniques in the corresponding sections. The base case is not energetically integrated at all. The proposed techniques achieve the maximum energetic integration for this process, reducing 85.9% energy consumption (Fig. 8).

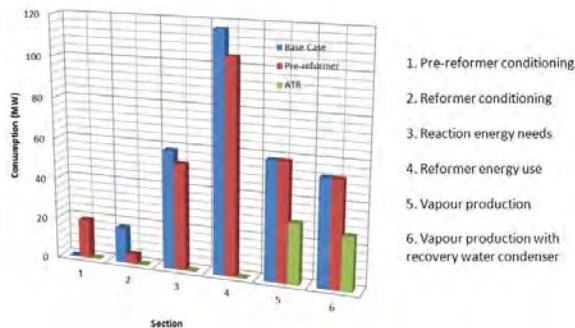


Fig. 7. Energy consumption evolution

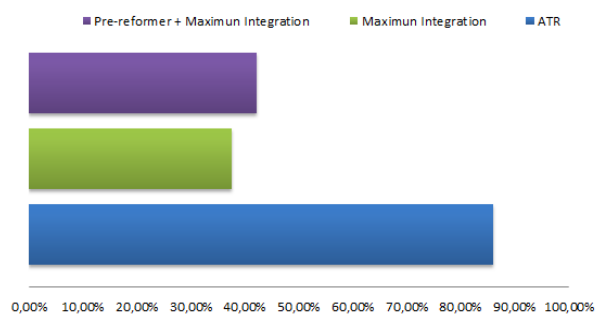


Fig. 8. Energy consumption reduction

4. Conclusions

This work shows an assessment of the potential measures to reduce and control emissions and energy use in a hydrogen plant. Consequently, a methodology was introduced including both quantitative and qualitative analysis. From the qualitative analysis, a list of specific measures was proposed. The achieved results showed that, despite being a mature technology, important energy efficiency improvements and CO₂ emissions reduction could be achieved. Therefore, the proposed methodology has turned out to be satisfactory.

The highlights are:

- The consumption in the primary reformer is reduced. Nevertheless, this option can cause problems if an integrated energy balance is not done properly.
- A pre-reforming installed prior to the first reformer reduces energy consumption.
- The substitution to ATR technique provides a significant reduction of the energy needs and improves the yield (steam needs are reduced to ratio V/C = 1).
- The substitution to PSA technique provides a reduction of energy needs, but it is necessary more adsorbent.

References

- [1] Ullmann's Encyclopedia of industrial chemistry, Gas production, G, 2007, pp.91-259.
- [2] Ullmann's Encyclopedia of industrial chemistry, Hydrogen, H, 2007, pp. 827-959.

- [3] A.C. Vosloo, Fischer–Tropsch: a futuristic view, *Fuel Processing Technology* 71, 2001, pp.149–155.
- [4] D.J. Wilhelm; D.R. Simbeck; A.D. Karp; R.L. Dickenson, Syngas production for gas-to-liquids applications: technologies, issues and outlook, *Fuel Processing Technology* 71, 2001, pp.139-148.
- [5] T. Rostrup-Nielsen, Manufacture of hydrogen, *Catalysis Today* 106, 2005, pp. 293–296.
- [6] J.I. Linares Hurtado; B.Y. Moratilla Soria, Hydrogen as an energetic vector (I/II) (in Spanish), 2007, available at <https://www.icaei.es/>.
- [7] I. Rafiqul; C. Weber; B. Lehmann; A. Voss, Energy efficiency improvements in ammonia production perspectives and uncertainties, *Energy* 30, 2005, pp. 2487-2504.
- [8] C. Koroneos; A. Dompros; G. Roumbas; N. Moussiopoulos, Life cycle assessment of hydrogen fuel production processes, *International Journal of Hydrogen Energy* 29, 2004, pp. 1443-1450.
- [9] European Commission, Council Directive 96/61/EC concerning integrated pollution prevention and control, *Official Journal of the European Communities* L 257, 1995, pp. 26-40.
- [10] United Nations Framework Convention on Climate Change, Reports of Clean Development Mechanism (CDM) project activities, available at <http://cdm.unfccc.int/>.
- [11] A. A. Evers FAIR-PR, <http://www.hydrogenambassadors.com/>, (accessed 10/12/2010).
- [12] Florida Solar Energy Center, Hydrogen basics, www.fsec.ucf.edu/, (accessed 10/12/2010).
- [13] European Commission, European IPPC Bureau (EIPPCB), <http://eippcb.jrc.es/>.
- [14] J. Ruddock; T.D. Short; K. Brudenell, Energy integration in ammonia production. *Sustainable World* 7, 2003, pp. 267-276.
- [15] The International Fertilizer Industry Association IFA, Fertilizer supply statistics, available from <http://www.fertilizer.org/ifa>.
- [16] The International Fertilizer Industry Association. IFA, Fertilizers and Climate Change, available from <http://www.fertilizer.org/ifa>.
- [17] R. Mendivil; U. Fischer; M. Hirao; K. Hungerbühler, A New LCA Methodology of Technology Evolution (TE-LCA) and its application to the production of ammonia (1950-2000), *International Journal of Life Cycle Assessment* 11 (2), 2006, pp. 98-105.
- [18] E. Worrell; K. Blok, Energy savings in the nitrogen fertilizer industry in the Netherlands. *Energy* 19 (2), 1994, pp. 195-202.
- [19] European Commission, Reference Document on Best Available Techniques for the Manufacture of Large Volume Inorganic Chemicals-Ammonia, Acids and Fertilisers, Institute for Prospective Technological Studies (IPTS), 2007, pp 35-94.
- [20] European Commission, Reference Document on Best Available Techniques for Energy Efficiency, Institute for Prospective Technological Studies (IPTS), 2008.
- [21] European Fertilizer Manufacturers Association EFMA, Best Available Techniques for Pollution Prevention and Control in the European Fertilizer Industry, Production of ammonia, Booklet 1, 2000.
- [22] U.S. EPA. (U.S. Environmental Protection Agency), Department of Energy, A Consumer's Guide to Energy Efficiency and Renewable Energy, Industry Plant Managers and Engineers, 2008, available at <http://www.epa.gov/>.

- [23] U.S. Department of Energy-Energy Efficiency and Renewable Energy, Industry plant Managers and Engineers: 20 Ways to Save Energy Now, 2008, available at <http://www.eere.energy.gov/>.

The effect of a boron oxide layer on hydrogen production by boron hydrolysis

Tareq Abu Hamed^{1,2*}, Bara Wahbeh³, Roni Kasher³

¹The Dead Sea and Arava Science Center, Tamar Regional Council, Israel

²Arava Institute for Environmental Studies, Hevel Eilot, Israel

³Ben-Gurion University of the Negev, Sde-Boqer, Israel

*Corresponding author. Tel: +97286356694, Fax: +97286356634, E-mail: tareq@arava.org

Abstract: Hydrolysis of boron is investigated as a part of a boron/boron oxide solar, water-splitting, thermochemical cycle. Boron was hydrolysed and boron oxide was gasified with steam in a tubular reactor. The influence of the reactor temperature and time on hydrogen conversion was measured at furnace set point temperatures of 873, 973 and 1073 K. The hydrogen production rate was measured by inline gas chromatography. The products were analyzed by X-ray diffraction. The average hydrogen production efficiency of 92% was obtained for both 973 and 1073 K. The formation of a boric acid layer on the reactor walls was attributed to the gasification of the boron oxide. The X-ray analysis shows 100% conversion of the boron to boron oxide and boric acid.

Keywords: hydrogen, thermochemical cycle, boron, oxide layer removal

1. Introduction

Hydrogen is an abundant and clean fuel with high energy density, making it a leading candidate in the search for an alternative to fossil fuels. However, the storage and transportation of hydrogen fuel for practical applications (e.g. internal combustion engine or fuel cells) remain among the most difficult problems to overcome before hydrogen can serve as a real alternative to fossil fuels [1]. Numerous methods for storage of hydrogen on-board vehicles have been considered, including compressed gas, liquid hydrogen and hydride compounds. Each method has significant and unresolved technical, safety and economic issues. Finding a feasible, on-board hydrogen storage solution is one of the major challenges in achieving a hydrogen economy. One such solution may be to produce the hydrogen on-board the vehicle at a rate that matches the rate of demand of the car engine. One method of on-board hydrogen production is to react a light metal with water. Boron is one of the most promising metal candidates for this purpose [2]. It is a light element with a molecular weight of 10.8g/mol. The reaction of boron with water yields a high hydrogen-to-metal ratio compared to other metals (see Table 1) [3]. Moreover, boron is very safe to store and to transport because its ignition temperature is high in dry or moist air and even in water.

Table 1. Theoretical H₂ produced by the hydrolysis of metals

Reaction	mole H ₂ /g-Fuel	STP L H ₂ /g-Fuel
2B + 3H ₂ O → 3H ₂ + B ₂ O ₃	0.139	3.00
2Al + 3H ₂ O → 3H ₂ + Al ₂ O ₃	0.056	1.25
Mg + H ₂ O → H ₂ + MgO	0.041	0.92
Fe + H ₂ O → H ₂ + FeO	0.018	0.40
Zn + H ₂ O → H ₂ + ZnO	0.015	0.34

The ignition and combustion processes of boron have been of great interest to many researchers because of its high heating value. Considerable experimental [4-5] and theoretical research [4-9] has been conducted with the objective of understanding the ignition and combustion of boron particles in oxygen. The data show the ignition of boron particles is

significantly delayed because of the formation of a layer of boron oxide (B_2O_3) on the surface of the boron.

Several studies prove that adding water to the oxygen environment can increase the oxidation rate. This finding is of particular significance to the proposed study. It is suggested that the increased oxidation rate is due to gasification of the protective B_2O_3 layer to boric acid (HBO_2). Smolanoff et al. [10] showed that the addition of water to the boron/oxygen reaction yields a higher reaction rate than when $HF(g)$, $CO_2(g)$, and $BF_3(g)$ are added. Data obtained by Krier et al. [11] show that the addition of water reduces the ignition delay time and reduces the ignition temperature for combustion of boron when compared to combustion in pure oxygen. Vovchuk et al. [12] measured B_2O_3 gasification rates in pure water and dry air atmospheres for temperatures as high as 1303 K. They found that the gasification rates for B_2O_3 in water vapor were significantly greater than those in air. Sontgen et al. [13] found that the addition of 3 to 8% water vapor to air significantly increased the oxidation rate at 803 K.

Data on the hydrolysis of boron in the absence of oxygen are limited. Experiments in steam by Rosenband et al. [14] were the first to demonstrate that the production of hydrogen by this method is feasible. Vishnevetsky et al. [15] considered the hydrolysis of boron in the absence of oxygen at moderate reactor temperatures (below 873 K). The hydrogen yield was 47 to 62% of the theoretical equilibrium value. It was confirmed that the reaction occurs only at temperatures above the melting point of boron oxide (723 K). Removal or thinning of the liquid oxide layer is attributed to a gasification reaction with steam that produces volatile metaboric acid. Limitations of the test apparatus excluded experiments above 873 K, where the gasification rate of boron oxide increases and higher hydrogen production yields are expected.

The objective of this paper is to investigate the effect of temperature on boron hydrolysis ($2B + 3H_2O \rightarrow 3H_2 + B_2O_3$) and to study the effect of boron oxide gasification reaction ($B_2O_3(l) + 3H_2O(g) \rightarrow 2H_3BO_3(g)$) on the hydrolysis process.

2. Methodology

The experimental setup is shown in Figure 1. A 100 cm long and 2.3 cm i.d. tubular, quartz reactor is placed inside a tubular furnace (40 cm long, concentric, cylindrical, electric ceramic heater). Steam was generated upstream in an electrical heater. The amount of steam generated was controlled by controlling the water flow via a peristaltic pump. Prior to each experiment, a crucible was loaded with weighed boron particles of 0.1 grams (amorphous, 97% pure) and placed in the reactor. Each time, the reactor was closed, evacuated and purged with N_2 . The nitrogen flow rate was 0.3 l/min during the whole experiment. When the desired temperature (873 K, 973 K, 1073 K) in the furnace was reached, the steam flow was directed into the reactor (0.54 mL/min, equivalent to 1 rpm in the peristaltic pump). During the experiment, the excess of steam was condensed into a water vapor trap. The outlet gas was analyzed continuously using an inline gas chromatograph (Varain 430 GC). The GC was fixed in automatic sampling mode and started to record data as soon as the steam valve was opened. Each run lasted 2 minutes.

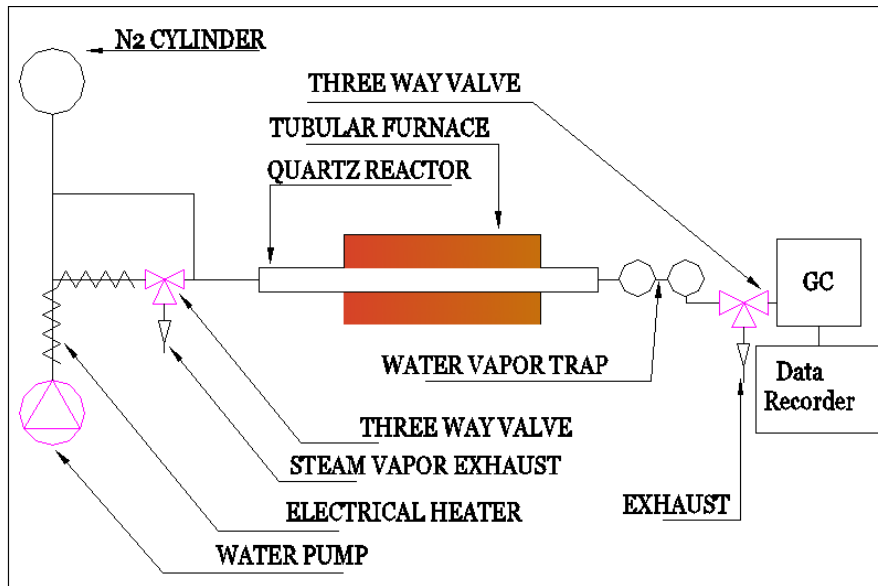


Fig. 1. Boron hydrolysis experimental setup

To examine the gasification of the oxide layer produced, small changes have been made to the experimental setup. A shorter quartz reactor (60 cm length, 2.3 cm i.d.) was placed in the tube furnace. The outlet of the quartz tube was open. Prior to each experiment, 4 crucibles were inserted into the reactor with the same amount of boron powder (0.1g) and placed in the reactor (dry and purged with N_2). During the experiment, boron crucibles were pushed out from the reactor into 500 mL flasks that contain nitrogen gas in order to prevent any further oxidation with air. This process was conducted on a regular time interval: 3 minutes between each crucible. Then the mass of the crucible was recorded.

3. Results and Discussion

Figures 2a and 2b show the hydrogen production at 973 and 1073 K. The hydrogen production efficiency at 973 K was 86 and 98% for run 1 and 2, respectively. At 1073 K, the efficiency was 93 and 90% for run 1 and 2 respectively. These values are much higher than the efficiency values obtained by Vishnevetsky et al., [15]. In both of the runs at both of the temperatures, the hydrogen production followed the same trend. The hydrogen production reached the maximum at $t = 8$ and 10 minutes for 973 and 1073 K, respectively.

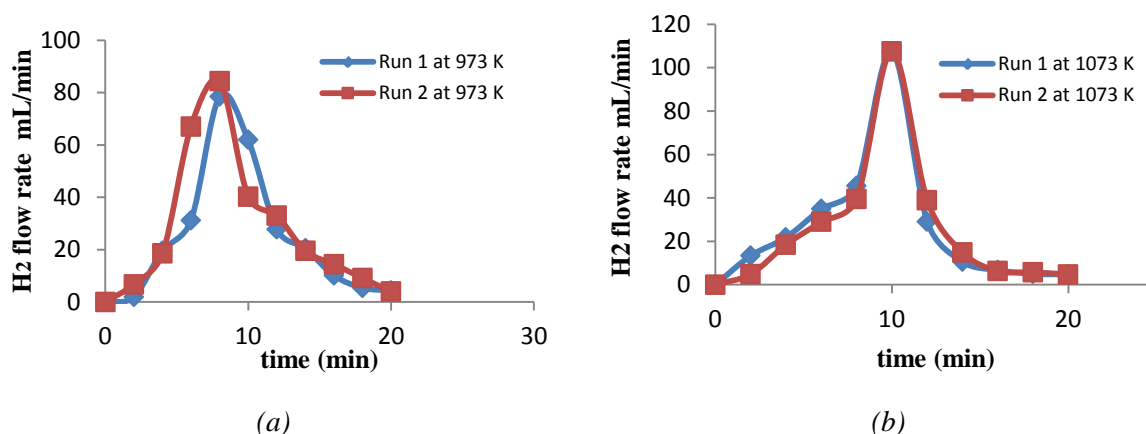


Fig. 2. Hydrogen production at a: 973 K and b: 1073 K

Figure 3 shows a comparison of the hydrogen production at 873, 973 and 1073 K. As seen from this figure, at 873 K, there was very low hydrogen production (efficiency only 5%) for

the period of the experiment. At 973 and 1073 K, the first detected hydrogen production was after 2 minutes. At 1073 K, the hydrogen production was higher than at 973K, but the efficiency was lower. Here, it is important to mention that the hydrogen analysis was performed every 2 minutes and that, most likely, there was more hydrogen produced than the values measured. The X-ray analysis shows that all the boron was converted to boron oxide and boric acid in the first 3 minutes.

In all runs, the hydrogen production started immediately after switching the steam valve on. This is confirmed by the visual observation of the condensation of boric acid and the gas chromatography analysis.

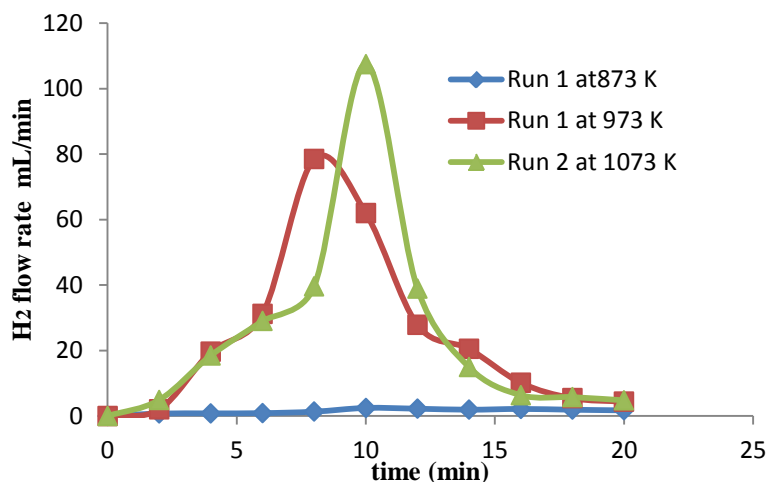


Fig. 3. H₂ production comparison for different temperatures

From the first minutes of the reaction, a formation of white, glittery particles was observed on the inner wall of the quartz tube outside the furnace where the temperature is 376 K. These particles start to condense on the tube directly after the steam valve is switched on (Figure 4a and 4b). These condensed particles continued to accumulate during the experiment and were very easy to remove. The X-ray analysis of these particles indicates that they are orthoboric acid (Figure 5). The formation of this layer is evidence of the gasification of boron oxide ($B_2O_3(l) + 3H_2O(g) = 2H_3BO_3(g)$) in parallel with the hydrolysis reaction.



Fig 4. The condensation of boric acid on the inner wall of the reactor during the hydrolysis experiment. a: at the beginning and b: at the end of the experiment.

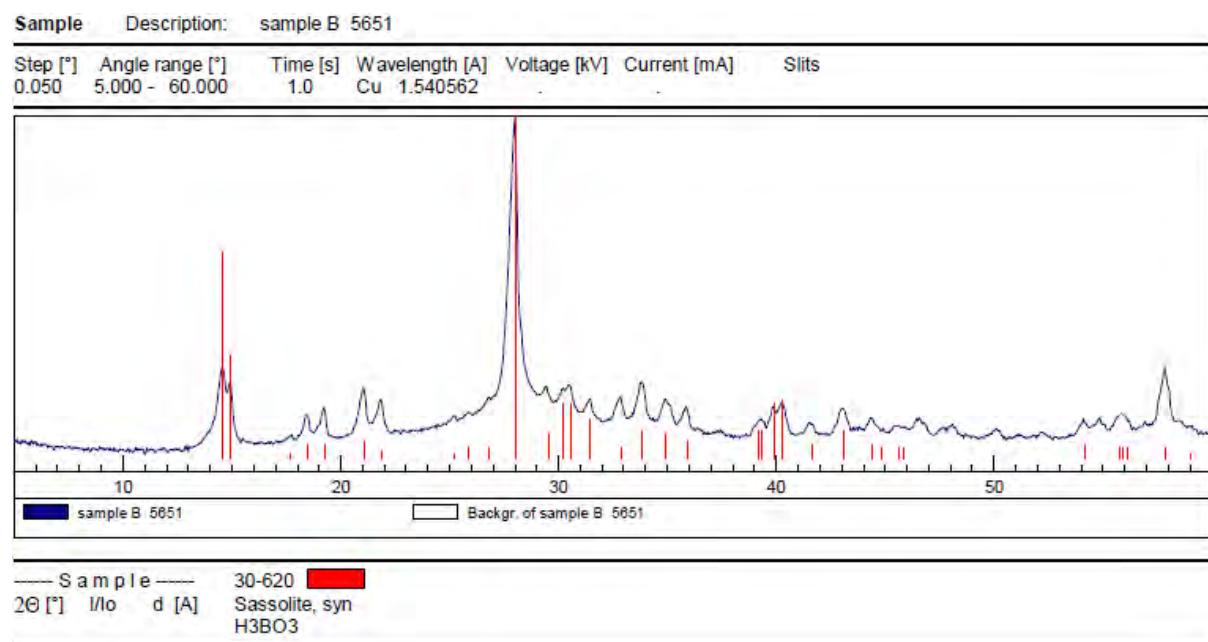


Fig 5. X-Ray analysis of condensed powder layer outside the furnace

Figure 6 shows the mass change during the hydrolysis of the boron powder at 973 K. Theoretically the hydrolysis of 0.1 grams of boron will generate 0.638 g of boron oxide; but the maximum weight recorded during the experiment was 0.229 g after 6 minutes of the reaction. This is due to the immediate gasification of the boron oxide layer. This gasification process was observed during the hydrolysis experiments: a white color deposition of boric acid was observed at $t = 1$ min of the hydrolysis experiment. After the sixth minute of the reaction, the weight of the particles in the crucible started to decrease. The X-ray analysis of the particles that remained in the crucibles shows 100% boron oxide after 3 minutes (Figure 7).

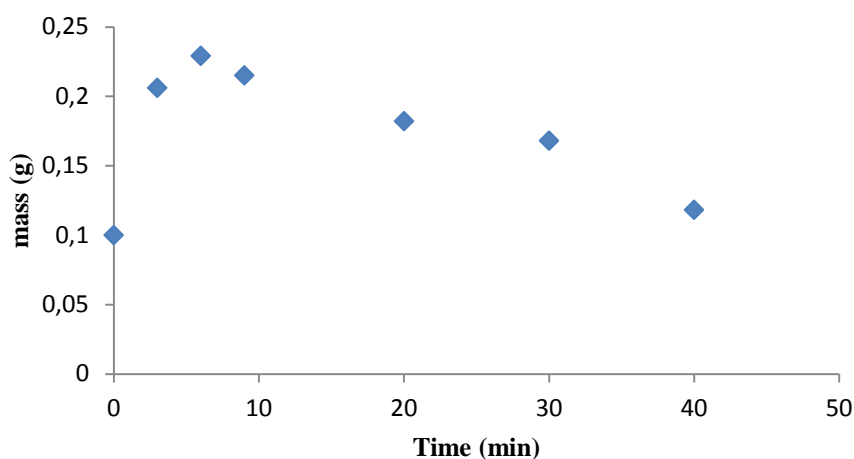


Fig. 6. Mass change in the boron sample during the hydrolysis process

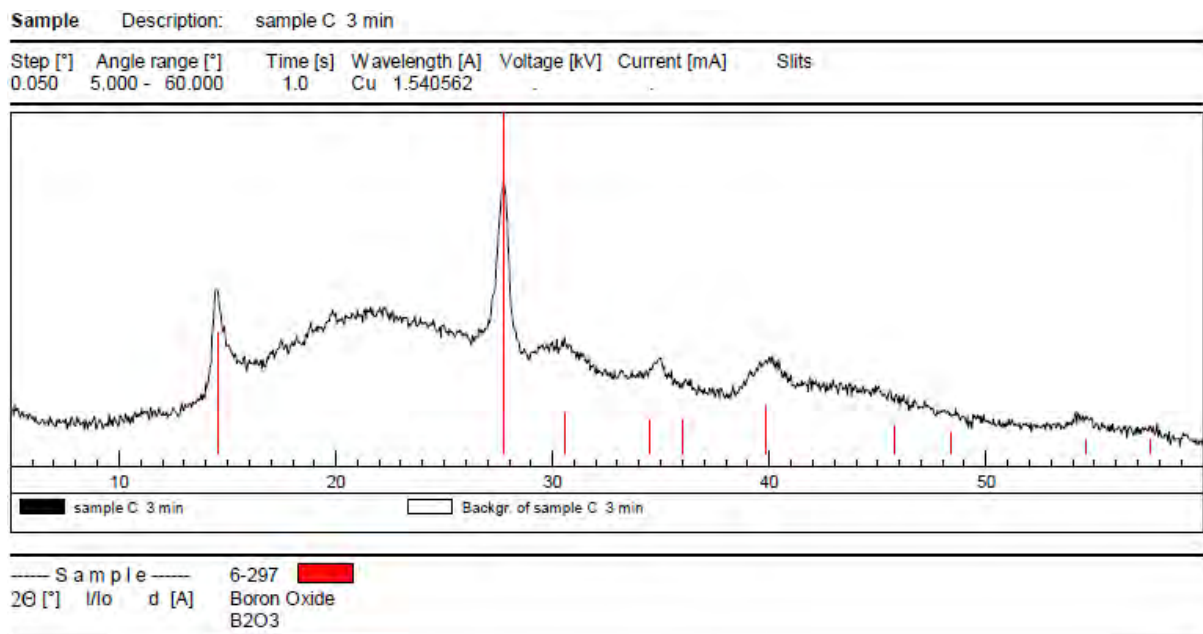


Fig 7. X-Ray analysis of particles remaining after the boron hydrolysis process ($t = 3$ min)

4. Conclusion

In this study, a tubular reactor was built and operated for the hydrolysis of boron and the gasification of boron oxide in nitrogen carrier gas. Hydrogen production was measured at furnace set point temperatures of 873, 973 and 1072 K. The primary objective of these initial experiments was to understand the boron hydrolysis process.

Hydrogen conversion was 92% for both 973 K and 1073 K. Very slow hydrogen production was observed at the temperature of 873K. Extensive deposition of boric acid was observed on the wall of the reactor outside the furnace where the temperature was 376 K.

The hydrolysis experiments show parallel processes of boron hydrolysis and boron oxide gasification. X-ray analysis of the particles remaining in the crucible shows 100% boron oxide. Thus, we conclude that the boron hydrolysis reaction is faster than the boron oxide layer gasification. In other words, the chemical reaction between the boron and the steam is much faster than the chemical reaction between the boron oxide and the steam. The use of the boron/boron oxide thermochemical cycle for hydrogen production shows an advantage over other cycles, due to the ease of removal of the oxide layer. By comparison, in the zinc/zinc oxide (ZnO) cycle, once a ZnO layer is formed, the hydrolysis reaction becomes limited by the diffusion of the reactants through the layer, which is harder to remove than the boron oxide layer [16].

References

- [1] G. Karim, Hydrogen as a spark ignition engine fuel, *International Journal of Hydrogen Energy* 28, 2003, pp. 569-577.
- [2] M. Epstein, Solar induced solid fuels for transportation, *Proceedings of the 12th International Symposium on Solar Power and Chemical Energy System*, 2004, Oaxaca, Mexico, paper No. 302.
- [3] T. Abu Hamed, J. Karni, M. Epstein, The use of boron for thermochemical storage and distribution of solar energy, *Solar Energy* 81, 2007, pp. 93-101.

- [4] C. L. Yeh, K. K. Kuo, Ignition and combustion of boron particles, *Progress in Energy and Combustion Science* 22, 1996, pp. 511-541.
- [5] C. C. Li, F. A. Williams, Ignition and combustion of boron particles in Combustion of boron-based solid propellants and solid fuels, Kuo, K. K., and Pein, R., Eds., Begell House Publishing Co. and CRC Press, Inc., 1993, pp. 248–271.
- [6] S. C. Li, F. A. Williams, Ignition and combustion of boron in wet and dry atmospheres, *Proceeding of the 23rd Symposium on Combustion*, 1990, pp. 1147–1154.
- [7] M. K. King, Boron ignition and combustion in air-augmented rocket afterburners, *Combustion Science and Technology*, 1972, pp. 155–164.
- [8] W. Zhou, R. A. Yetter, F. L. Dryer, H. Rabitz, R. C. Brown, C. E. Kolb. Comprehensive physical and numerical model of boron particle ignition. *Proceeding of the 26th International Symposium on Combustion*, 1996 pp. 1909–1917.
- [9] R. C. Brown, C. E. Kolb, S. Y. Cho, R. A. Yetter, H. Rabitz, F. L. Dryer, Kinetic model for hydrocarbon-assisted particulate boron combustion, *International Journal of Chemical Kinetics* 26, 1994, pp. 319–332.
- [10] J. Smolanoff, M. Sowa–Resat, A. Lapicki, L. Hanley, S. Ruatta, P. Hintz, S. L. Anderson, Kinetic parameters for heterogeneous boron combustion reactions via the cluster beam approach, *Combustion and Flame* 105, 1996, pp. 68–79.
- [11] H. Krier, R. L. Burton, S. R. Pirman, M. J. Spalding, Shock initiation of crystalline boron in oxygen and fluorine compounds. *Proceeding of the 30th American Institute of Aeronautics and Astronautics Thermophysics Conference*, 1995, paper No. 2095-2120.
- [12] Y. A. Vovchuk, A. N. Zolotko, L. A. Klyachko, D. I. Polishchuk, V. G. Shevchuk, Gasification of boron oxide, *Fizika Goreniya i Vzryva* 10, 1972, pp. 615-618.
- [13] R. Sontgen, A. Freidrich, A simple model of the oxidation kinetics of boron in a medium containing water vapor, in *Combustion of Boron Based Propellant and Solid Fuels*, K. K. Kuo and R. Pein, Eds., Begell House Publishing Co. and CRC Press, Inc., 1993, pp. 211-217.
- [14] V. Rosenband, A. Gany, Y.M. Timnat, Magnesium and boron combustion in hot steam atmosphere, *Defense Science Journal* 48, 1998, pp. 309-315.
- [15] I. Vishnevetsky, M. Epstein, T. Abu-Hamed, J. Karni, Boron hydrolysis at moderate temperatures – First step to solar fuel cycle for transportation, *Journal of Solar Energy Engineering* 130, 2008, pp. 14506-14511.
- [16] R. J. Weiss, H. C. Ly, K. Wegner, S. E. Pratsinis, A. Steinfeld, H₂ production by Zn hydrolysis in a hot-wall aerosol reactor, *AIChE Journal* 51, 2005, pp. 1966–1970.

Case study: Technical assessment of the efficiency optimization in direct connected PV-Electrolysis system at Taleghan-Iran

Abolfazl Shiroudi¹, Seyed Reza Hosseini Taklimi^{2,*}, Nilofar Jafari¹

¹Ministry of Energy-Renewable Energy organization of Iran (SUNA), Tehran, Iran

²Linköping University of Technology, Linköping, Sweden

* Corresponding author. Tel: +46 760830785, E-mail: seyho130@student.liu.se

Abstract: The use of PV array energy in supplying the electrolyzer systems is very suitable. During the daylight hours, the sunlight converts by PV array into electrical energy which will be used for electrolyzing process. Then hydrogen produced by the electrolyzer is compressed and stored in hydrogen vessel. This provides energy for the fuel cell to meet the load when the solar energy is insufficient. Solar hydrogen technology is relatively simple and the only raw material for the production of solar hydrogen is water. In this study technical results obtained from direct connection of 10 kW PV array with 5 kW electrolyzer systems for hydrogen production and storage at Taleghan site. Variations of the solar radiation intensity, hydrogen production rate, solar hydrogen efficiency and overall efficiency of solar hydrogen energy were considered as base of analyses. It is found that the minimum and maximum overall energy efficiency values of the system are 0.93 % and 5.01 %, respectively. The result shows a great potential in direct solar radiation for absorbing and converting it to other types of energy in Iran. Using solar energy required high initial investment, so converting solar energy to other types of energy with high efficiency systems is vital.

Keywords: Photovoltaic, Water Electrolysis, Hydrogen Production, System Efficiency, Taleghan

Nomenclature

E	calorific value of hydrogen..... $J.mt^{-1}$	T_r	PV cell reference temperature..... $^{\circ}C$
Q	hydrogen production rate $ml.sec^{-1}$	v	hydrogen production $m^3.hr^{-1}$
S	solar radiation intensity..... $W.m^{-2}$	β	Temperature coefficient of a solar cell in STC..... $^{\circ}C^{-1}$
A	PV array surface..... m^2		
I_e	current A		
T_c	the PV cell temperature $^{\circ}C$		

1. Introduction

As conventional fossil fuel energy sources diminish and the world's environmental concern about acid deposition and global warming increasing, renewable energy (RE) resources are attracting more attention as alternative energy sources [1]. The use of RE resources, which do not endanger the environmental balance, is a way to solve many of the environmental problems caused principally by the excessive use of fossil fuels. RE resources are free of pollution during their development and operation for power generation [2]. RE systems based on intermittent sources exhibit strong short term and seasonal variations in their energy outputs. Therefore, the need for storage of energy arises; storing the energy produced in periods of low demand to utilize it when the demand is high, ensuring full utilization of intermittent sources available [3]. Solar photovoltaic energy has been widely utilized in small size application and is the most promising candidate for research and development for large-scale use, as the fabrication of less costly photovoltaic devices becomes reality [1]. Hydrogen holds a preminent position among the solar fuel candidates because of its high energy content, low environmental effect, storage compatibility and distribution [4-6]. Solar hydrogen is described as a potential energy storage medium to offset the variability of solar energy [7]. The seasonal storage of solar energy in the form of hydrogen can provide the basis for a completely renewable energy system [8]. Hydrogen can be generated by using different

technologies, but only some of them are environmentally friendly. It is argued that hydrogen generated from electrolyzing water is a leading candidate for a renewable and environmentally safe energy carrier due to the following reasons [9]:

- Solar hydrogen technology is relatively simple and, therefore, the cost of such a fuel is expected to be substantially less than the present price of gasoline.
- The only raw material for production of hydrogen is water, which is a renewable resource.
- Large areas of the globe have access to solar energy which is the only required energy source for solar hydrogen generation.

Country of Iran with more than $4.5 \text{ kWh/m}^2 \cdot \text{day}$ radiations has a great potential for converting solar radiation to electricity. One of the efforts done in the field of constructing and utilization solar hydrogen plant is constructing stand-alone energy system PV-electrolyzer-fuel cell in Taleghan-Iran. The purpose is to demonstrate the technical feasibility of using hydrogen as solar energy storage medium. This small scale demonstrative energy system uses PV as the primary energy conversion technology, hydrogen as the storage medium and a fuel cell as the regenerative technology [10].

2. Methodology

In this study, we will evaluate overall efficiency from connection of 10 kW PV array with 5 kW alkaline electrolyzer systems for hydrogen production and storage at Taleghan renewable energies site. We assumed that water electrolysis operated during a sample day in summer season during 150 minutes (10:30 until 12:50). Variations of the solar radiation intensity, hydrogen production rate, solar hydrogen efficiency and overall efficiency of solar hydrogen energy in operating conditions were gathered and considered as base of analyses.

3. Results

3.1. Description of the solar hydrogen energy system

This energy system is located in a mountainous area with latitude N $36^\circ, 8'$, longitude E $50^\circ, 34'$ and altitude 1700 m. The system consists of a 10 kW photovoltaic (PV) array coupled to a 5 kW bipolar, alkaline electrolyzer, and a gas hydrogen storage tank. When the sun shines, PV power is available and directly supply the load. By this power electrolyzer produces hydrogen, which is delivered to the hydrogen storage tanks. When PV array cannot provide electricity, the 1.2 kW PEM fuel cell will begin to produce electricity. Hydrogen in storage tank prepares the feed of fuel cell for production of needed electricity [11].

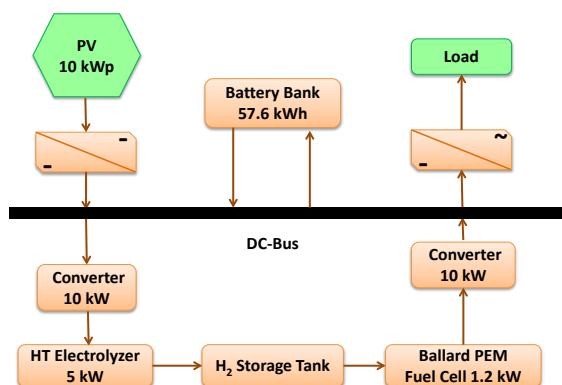


Fig. 1. Schematic of solar hydrogen energy system at the Taleghan site

Experimental results for the operation of directly coupled PV-electrolyzer in operating regime of electrolyzer for a sample day in summer are presented. The schematic of this energy system is given in Fig. 1.

3.2. Photovoltaic array

Solar energy is one type of the RE resources, which can be converted easily and directly to the electrical energy by PV converters. The PV module is a polycrystalline silicon type with maximum output of 45 W, an open circuit voltage of 20.5 V and 10 kW PV array consists of 224 solar panels MA36/45 modules installed at the Taleghan site. The PV array has a fixed inclination of 45 degree with horizontal and it is mounted such that the module is facing south direction [12]. Each module is 462 mm wide and 977 mm long for an area of 0.45 m² per module and total surface of 101.1 m² (2×7×16×0.45 ≈101.1 m²). This angle corresponds to the optimum tilting in spring for the installed PV and is the latitude of Taleghan area. The power also depends on temperature, wind speed, and age of cells. The efficiency (η_e) of a solar cell is a function of the cell temperature (T_c) and it is defined as:

$$\eta_e = \eta_r [1 - \beta(T_c - T_r)] \quad (1)$$

Where η_r is the efficiency of a solar cell at standard conditions, T_c the temperature of PV cell (°C), T_r the PV cell reference temperature, and β is the temperature coefficient of a solar cell in STC (that for PV module is a polycrystalline silicon is 0.0004 °C⁻¹) [13-14].

Table 1. Parameters related to solar radiation, ambient temperature and power system vs. time

Time	Insolation (W/m ²)	Ambient temp. (°C)	Module temp. (°C)	Power system (kW)	Efficiency system (%)
6 a.m.	26	19	20	0.2989	11.45
7 a.m.	79	20	22	0.9045	11.41
8 a.m.	176	20	24	1.9988	11.32
9 a.m.	387	21	29	4.3236	11.13
10 a.m.	553	22	33	6.1016	10.99
11 a.m.	677	24	38	7.3760	10.86
12 a.m.	738	25	40	8.0086	10.81
13 p.m.	731	26	41	7.9306	10.81
14 p.m.	680	27	41	7.4087	10.86
15 p.m.	585	25	37	6.4277	10.95
16 p.m.	402	23	31	4.4912	11.13
17 p.m.	201	20	26	2.2642	11.22
18 p.m.	96	17	21	1.0770	11.32
19 p.m.	36	16	17	0.4138	11.45
20 p.m.	6	15	15	0.0692	11.50

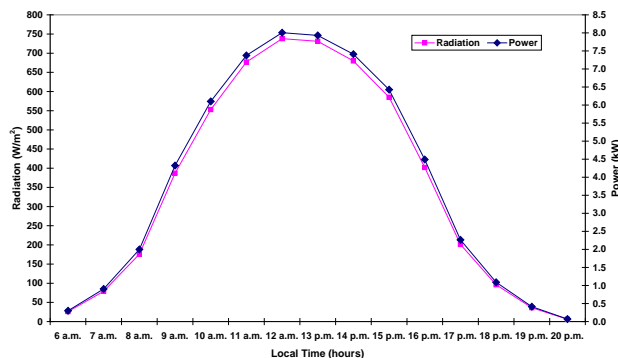


Fig. 2. Variations of the solar radiation intensity and power of 10 kW PV vs. time for a sample day

According to data received such as solar radiation intensity, ambient temperature, modules temperature, can be produced solar modules and system efficiency in the period 6 a.m. till

8 p.m. in sample day at Taleghan site was calculated. Parameters related to solar radiation intensity, ambient temperature, modules temperature, power system and solar cell efficiency versus time for sample day are given in Table 1. Variations of the solar radiation intensity, producing power system, efficiency and cell temperature of PV array against to time for a sample day are given Figs. 2 and 3.

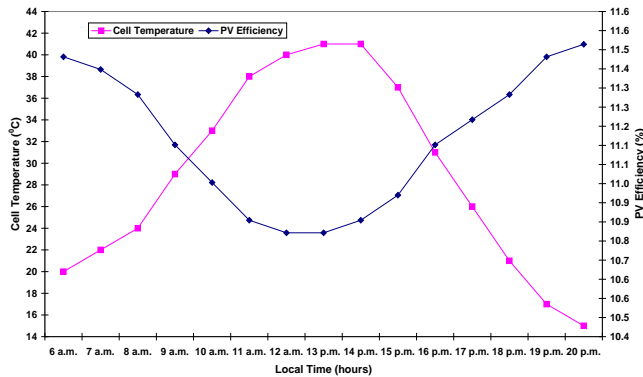


Fig. 3. Variations of efficiency of PV arrays and cell temperature vs. time for a sample day

3.3. Battery bank

It is known that a solar hydrogen system needs a storage system to provide energy for the cases of inappropriate weather conditions, instantaneous overload conditions, or demand for energy after sunset [15-16]. Sun irradiance is stochastic variables by nature. Energy storage such as in a battery is required for storing energy from PV array for the back up and stand by power source. The battery type is lead-acid because of the low cost and good electrical performance under various conditions [17-18]. The selection of a proper size of the battery bank for these types of applications requires a complete analysis of the battery's charge and discharge requirements [19-20]. The lead-acid batteries have the longest life and the least cost per amp-hour of any of the choices [21]. The battery system is made up of forty-eight deep discharge lead-acid batteries which are installed at the capacity of 57.6 kWh (12V×100 Ah × 48 cell). Each battery has an average lifetime of five years. When the electrolyzer is turn off, the excess energy generated from PV array is used to charge the batteries. If electrolyzer needs more power, the rest of power for operation is supplied by the batteries.

3.4. Inverter

A 10 kW Sunny Boy 2500U model inverter is a single-phase AC power source that is connected between the battery bank and utility grid at 195-251 V_{AC}. The battery voltage decrease when the AC loads increase. The inverter is based on a power unit that operates with a very high efficiency and optimal reliability. For more specifications, see Table 2 [22].

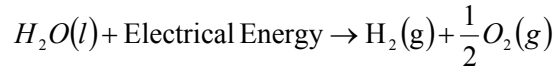
Table 2. Inverter technical characteristics (Sunny Boy model 2500)

P _{nominal}	2200 W _p	Max. AC-power	2500 W
Max input voltage	600 V	Peak inverter efficiency (η_{max})	93-94.4%
Max input current	11.2 A	AC input frequency	49.8-50.2 Hz
PV-voltage range MPPT	250-600 V	V _{AC}	198-251 V

3.5. Hydrogen unit

Water electrolysis technology has the highest energy efficiency in non-fossil fuel based hydrogen production and is ideally suited for coupling with intermittent renewable energy resources [19]. In general, there is a good match between the polarization curves of PV cells

and water electrolysis. However electricity from PV is expensive and hydrogen produced from such electricity is even more expensive, but this technology is well developed and matured for a large scale electricity and hydrogen generation [23]. The decomposition of water into hydrogen and oxygen can be achieved by passing an electric current between two electrodes separated by an aqueous electrolyte. The total reaction for splitting water is [24]:



In this pilot, the electrolyzer is a bipolar and alkaline type manufactured by the Hydrotechnik (Germany). The electrolyzer module consists of 10 cells in series. The nominal operating point is rated load, 250 amperes and rated voltage, 25 V_{max}. The electrolyte (KOH) concentration inside the cells is about 28 wt. %; the amount of hydrogen produced in one hour by the electrolyzer is found by the formula:

$$v = 0.000419 \times I_e \times A \times n = 4.12 \times 10^{-3} \cdot I_e \quad (\text{m}^3/\text{hr}) \quad (2)$$

where I_e is the current (in Ampere), A is a coefficient, n is number of electrolytic cells, and v is the hydrogen production in m³/hr. Hydrogen is stored at 10 bars in a tank to feed the fuel cell at low solar radiation levels and hence supply the required load power [25]. The maximum stable rate of hydrogen production was about 1 Nm³/hr. The electrolysis efficiency is about 70 %, based on the HHV (Higher heat Value) [26].

$$P_{out} = 1 \left(\frac{\text{m}^3}{\text{hr}} \right) \times \frac{1(\text{mol } H_2)}{22.4(\text{lit})} \times \frac{285830(\text{J})}{1(\text{mol } H_2)} \times \frac{1(\text{hr})}{3600(\text{sec})} \times \frac{1000(\text{lit})}{1(\text{m}^3)} = \frac{285830000}{80640} = 3544\text{W}$$

$$\eta = \frac{P_{out}}{P_{in}} = \frac{3544(\text{W})}{5000(\text{W})} = 0.7089 \quad (3)$$

The oxygen output still contains small amounts of hydrogen gas and vast amounts of water vapor. It was not used in this system and was released into the atmosphere [27]. The hydrogen from the electrolyzer is sent into a low pressure tank (buffer tank) that is kept at a pressure lower than the hydrogen output pressure of the high pressure tank as shown in Fig. 4.

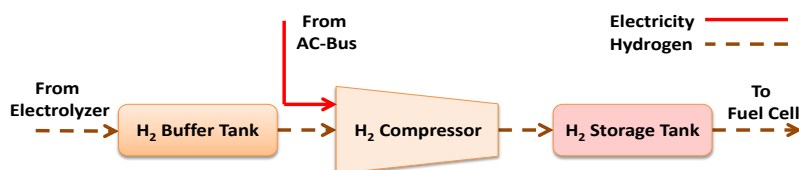


Fig. 4. Schematic of hydrogen storage system

Compression occurs during compressor cycles in which the hydrogen is continuously removed from the low-pressure tanks beginning at the current pressure of the low-pressure tank and ending when the pressure drops to a specified minimum supply pressure. The volume of hydrogen vessel is 1 m³ and maximum pressure is 10 bars. It is known that a stand-alone photovoltaic system needs a storage system to provide energy for the cases of inappropriate weather conditions, instantaneous overload conditions, or demand for energy after sunset [28]. Due to simple operation, high efficiency and ability to provide power quickly from a standby configuration, a PEM fuel cell was chosen for this project. This system manufactured by Ballard power system Inc.(Canada) that has 30 cells and provides up to 1.2 kW of unregulated DC power at a nominal output voltage. The output voltage varies

with power, ranging from about 43 V at system idle to about 26 V_{DC} at full load. It has the capability to operate at low temperature and has short start-up period [29]. Overall system efficiency for the direct coupling system calculated according to the following equation:

$$\eta_{overall} = \frac{Q \cdot E}{S \cdot A} \quad (4)$$

where A is the PV array total surface (m²), Q is hydrogen production rate (ml/sec), E is the calorific value of hydrogen (J/ml), and S is solar radiation (W/m²) [30].

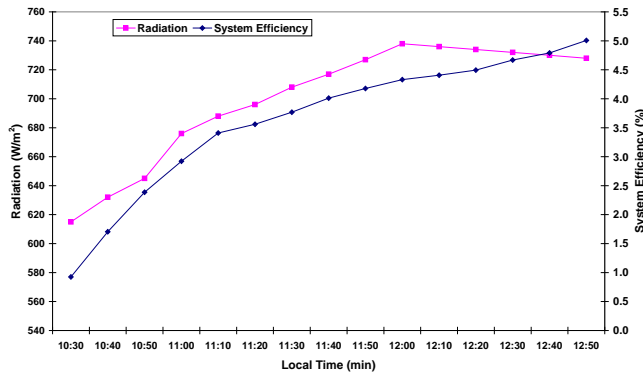


Fig.5. Variations of solar radiation intensity and solar hydrogen efficiency for a sample day

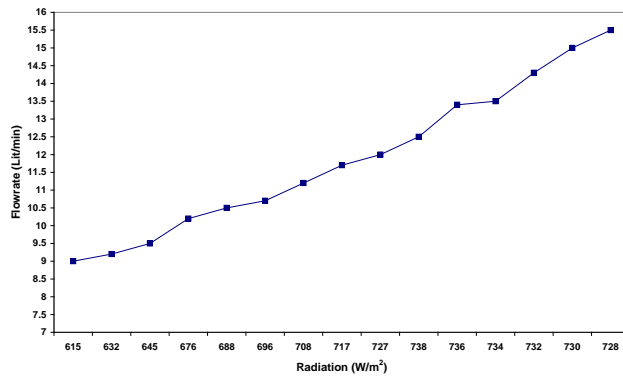


Fig.6. Variations of HPR vs. solar radiation

Hydrogen gas has the highest calorific value. When one gram of hydrogen is burnt completely, it produces 150 kJ. Thus the calorific value of hydrogen is 150 kJ/g (≈ 12.6 J/mol) [31]. We assumed that water electrolysis operated during a sample day in summer season during 150 minutes (10:30 a.m. until 12:50 a.m.).

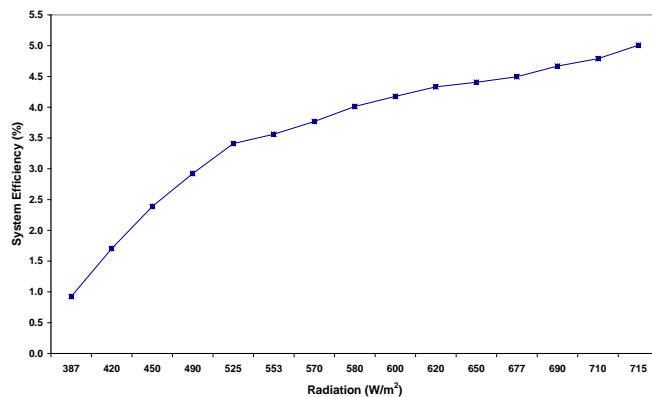


Fig.7. Variations of solar hydrogen system efficiency vs. solar radiation

Overall efficiency of solar hydrogen system in this time is shown that in Table 3; also variations of the solar radiation intensity and solar hydrogen efficiency versus time are shown in Fig. 5 and variations of hydrogen production rate and solar hydrogen energy system efficiency versus solar radiation intensity are shown in Figs.6 and 7. The effects of hydrogen production rate and solar radiation on the overall efficiency system are also given in Table 3 and are plotted in Fig. 7. The increase in overall efficiency was from 0.93 to 5.01 % with the increase in current from 25 to 250 amperes, module temperature from 34 to 41°C and hydrogen production rate from 9 to 15.5 lit/min.

Table 3. Parameters related to solar radiation, ambient temperature and power system vs. time

Time	Voltage (V)	Current (A)	Hydrogen Production rate (lit/min)	Insolation (W/m ²)	Ambient Temp. (°C)	Module Temp. (°C)	Overall Efficiency System (%)
6 a.m.	20.2	25	9.0	615	23	34	0.93
7 a.m.	21.4	50	9.2	632	23	35	1.70
8 a.m.	21.8	75	9.5	645	23.5	36	2.39
9 a.m.	22.3	100	10.2	676	24	38	2.92
10 a.m.	22.6	125	10.5	688	24	38.5	3.41
11 a.m.	22.7	137.5	10.7	696	24.5	39	3.56
12 a.m.	22.8	150	11	708	24.5	39	3.77
1 p.m.	22.9	162.5	11.5	717	24.5	39.5	4.01
2 p.m.	23	175	12	727	25	40	4.18
3 p.m.	23.1	187.5	12.5	738	25	40	4.33
4 p.m.	23	200	13	736	26	40	4.41
5 p.m.	22.8	212.5	13.5	734	26.5	40	4.49
6 p.m.	22.7	225	14	732	26.5	40	4.67
7 p.m.	22.4	237.5	15	730	27	40.5	4.79
8 p.m.	21.7	250	15.5	728	27	41	5.01

4. Conclusions

- The coupling of PV field and an electrolyzer allows converting renewable electricity into time-stable storage. The time of storage can be unlimited and there is no loss of energy in stored energy. Using a fuel cell provide a silent electricity generator which has no environmental impact.
- The replacement of conventional technologies like batteries by new hydrogen technologies including using fuel cells in RE based stand-alone power systems is technologically feasible. It reduces emissions, noise and fossil fuel dependence and increases renewable energy penetration.
- New energy generators for stand-alone applications are expected to increase the comfort of people. The actual solutions are either limited by a low autonomy inducing reduction of the electricity consumption during worst seasons or noisy and using fossil energy.
- Iran country located on solar belt and has a great potential in direct natural solar radiation. Solar energy required high initial investment, so converting solar energy to other types of energy with high efficiency systems is vital.

References

- [1] K. Ro, S. Rahman, IEEE Transactions on Energy Conversion 13(3), 1998, pp. 276-281.
- [2] A.M. Ramirez, P.J. Sebastian, S.A. Gamboa, M.A. Rivera, O. Cuevas, J. Campos, Int J Hydrogen Energy 25, 2000, pp. 267-271.

- [3] W. Isherwood, J.R. Smith, S.M. Aceves, G. Berry, W. Clark, R. Johnson, D. Das, D. Goering, R. Seifert, *Solar Energy* 25, 2000, pp. 1005-1020.
- [4] M. Momirlan, T.N. Veziroglu, *Renewable and Sustainable Energy Reviews* 3, 1999, pp. 219-231.
- [5] M. Momirlan, T.N. Veziroglu, *Renewable and Sustainable Energy Reviews* 6, 2002, pp. 141-179.
- [6] A. Midilli, M. Ay, I. Dincer, M.A. Rosen, *Renewable and Sustainable Energy Reviews* 9, 2005, pp. 255-271.
- [7] G.J. Conibeer, B.S. Richards, *Int J Hydrogen Energy* 32, 2007, pp. 2703-2711.
- [8] Ø. Ulleberg, *Solar Energy* 76, 2004, pp. 323-329.
- [9] J. Nowotny, C.C. Sorrell, L.R. Sheppard, T. Bak, *Int J Hydrogen Energy* 30, 2005, pp. 521-544.
- [10] S. Galli, M. Stefanoni, *Int J Hydrogen Energy* 22(5), 1997, pp. 453-458.
- [11] D.B. Nelson, M.H. Nehrir, C. Wang, *Renewable Energy* 31, 2006, pp.1641-1656.
- [12] Technical Catalogue of Solar Module, MA36/45, Optical Fiber Fabrication Co, Iran.
- [13] M.D. Siegel, S.A Klein, W.A. Beckman, *Solar Energy* 26, 1981, pp. 413-418.
- [14] C. Soras, V. Makios, *Solar Cells* 25(2), 1988, pp. 127-142.
- [15] B. Wichert, M. Dymond, W. Lawrance, T. Friese, *Renewable Energy* 22(1-3), 2001, pp. 311-319.
- [16] E. Koutroulis, K. Kalaitzakis, *Renewable Energy* 28(1), 2003, pp. 139-152.
- [17] A. Urbina, T.L. Paez, R.G. Jungst, *Intersociety Energy Conversion Engineering Conference and Exhibit*, 2000, pp. 995-1003.
- [18] P.C. Butler, J.T. Crow, P.A. Taylor, *the 19th International INTELEC*, 1987, pp. 311-318.
- [19] K.E. Cox, K.D. Williamson, *Hydrogen: its technology and implications*, Ohio: CRC Press Inc, 1977.
- [20] G.W. Vinal, *Storage Batteries*, 4th edition, New York, N.Y.: John Wiley, 1967.
- [21] *Solar Electric Products Catalog*, 2005.
- [22] www.SMA.de.
- [23] S.A. Sherif, F. Barbir, T.N. Veziroglu, *Solar Energy* 78, 2005, pp. 647-660.
- [24] M.J. Khan, M.T. Iqbal, *Renewable Energy* 30, 2005, pp. 421-439.
- [25] Th.F. El-Shatter, M.N. Eskandar, M.T. El-Hagry, *Renewable Energy* 27, 2002.
- [26] *Instruction for erection operation and maintenance for hydrogen generation and compression plant EV05/10 system DEMAG*, 1998.
- [27] R. Perez, *Home Power* 22, 1991, pp. 26-30.
- [28] E. Koutroulis, K. Kalaitzakis, *Renewable Energy* 28(1), 2003, pp. 139-152.
- [29] Nexa™ (310- 0027) *Power Module User's Manual*, MAN5100078, 2003.
- [30] G.E. Ahmad, E.T. El-Shenawy, *Renewable Energy* 31, 2006, pp. 1043-1054.
- [31] <http://home.att.net/~cat6a/fuels-VII.htm>.

Demonstration project of the solar hydrogen energy system located on Taleghan-Iran: Technical-economic assessments

Abolfazl Shiroudi¹, Seyed Reza Hosseini Taklimi^{2,*}

¹Ministry of Energy-Renewable Energy organization of Iran (SUNA), Tehran, Iran

²Linköping University of Technology, Linköping, Sweden

* Corresponding author. Tel: +46 760830785, E-mail: seyho130@student.liu.se

Abstract: One of the most attractive features of hydrogen as an energy carrier is that it can be produced from abundant material like water. The use of electrolysis to produce hydrogen from water is an efficient method from small to large scales. Energy for supplying water electrolysis systems can be provided by photovoltaic arrays. During the daylight hours, the sunlight on the photovoltaic arrays converts into electrical energy which can be used for electrolyzer. The hydrogen produced by the electrolyzer is compressed and stored in hydrogen vessel and provides energy for the fuel cell to meet the load when the solar energy is insufficient. This study investigates a stand-alone power system that consists of 10 kW PV arrays as power supply and 5 kW electrolyzer. They have been integrated and worked at Taleghan site in Iran. Result was simulated and optimized by using HOMER simulation tools and techno-economic analysis of system presented in this paper.

Keywords: Hydrogen, PV array, Electrolyzer, Fuel cell, HOMER

1. Introduction

Renewable energy (RE) sources are attracting more attention as alternative energy sources nowadays. Depletion of energy sources and global warming play big role in this movement [1]. RE sources can open a new ways to solve these environmental issues. They usually free of pollution during development and operation for power generation [2]. Integration of RE with energy storage would provide a better system reliability making it suitable for remote stand-alone applications [3]. Among these sources, solar energy is an important kind of them. Solar photovoltaic (PV) energy has been widely utilized in small size application and is the most promising candidate for research and development for large-scale use, as the fabrication of less costly PV devices becomes a reality [1]. Seasonal solar energy which stores in the form of hydrogen can provide the basis for a completely renewable energy system. One of the most promising applications is stationary stand-alone power systems, particularly those located in remote areas where the cost of transporting fuel is high [4]. There is a growing awareness that hydrogen is the fuel of the future. Solar hydrogen is a leading candidate for a renewable and environmentally safe energy carrier [5]. Iran with more than 4.5 kWh/m².day radiations has a great potential for attracting and converting it to electricity. One of the efforts done in the field of constructing and utilization solar hydrogen plant is constructing stand-alone power system PV- electrolyzer- fuel cell in Taleghan site. The current paper evaluates the techno-economic aspects of PV-Electrolyzer-Fuel cell system. Hybrid optimization model for electric renewable (HOMER) was used as the simulation and optimization tools. The schematic of the plant at Taleghan site is given in Fig. 1.

2. Methodology

Hybrid systems based on the synergy between RE sources and conventional energy systems can be a reliable solution for remote sites to provide their need of energy. In this study, first PV cells hourly data of Electricity production gathered. Specification of each units in system such as PV array, water electrolysis, hydrogen storage tank, a fuel cell and a Power Management Unit (PMU) collected and they used for design and calculating primary model of HOMER. Then model optimized by software and the results of techno-economic analysis of

integration between PV panels, alkaline water electrolysis and hydrogen storage tank are presented.

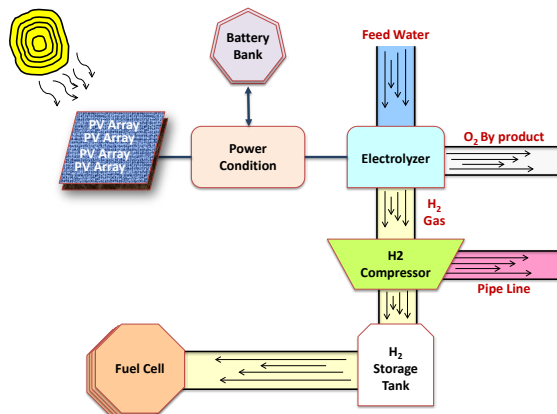


Fig. 1. Schematic of the PV-Electrolyzer-Fuel cell energy system at the Taleghan site

3. Result

3.1. Description of the system

This stand-alone energy system is located in altitude 1700 m and consists of a 10 kW_p PV array coupled to a 5 kWe bipolar, alkaline electrolyzer, a gas hydrogen storage tank (1 m³), battery banks, converters DC/AC and a PMU. When the sun shines, PV power is available and it used directly to supply the load. Then electrolyzer turns on for producing hydrogen, which is delivered to the hydrogen storage tanks. In absent of solar the 1.2 kW Proton Exchange Membrane (PEM) fuel cell will begin to produce energy for the load using hydrogen from the hydrogen storage tank to produce the necessary electricity [6]. The PMU is in charge of the conversion and the dispatching of the energy between each component. It is composed of many converters and an inverter as well as a PLC, programmed to optimally switch on or off system components [7].

3.1.1 PV array

Solar energy is one type of the RE resources, which can be converted easily and directly to the electrical energy by PV converters. The PV array consists of 224 solar panels MA36/45 modules configured into 14 independent sub arrays. The array is broken into sub arrays that are each individually controlled. Each sub-array consists of 16 modules, which connected in parallel of seven modules in series. The nominal power rating for the array is 10 kW_p. The PV module is a polycrystalline silicon type with maximum output of 45 W. Each module is 462 mm wide and 977 mm long for an area of 0.45 m² per module and total surface of 101.1 m² (2×7×16×0.45=101.1 m²).

Table 1. Photovoltaic Module Electrical characteristics (MA 36/45)

Nominal power	45 w	Short circuit current	2.96 A
Nominal load voltage	20.5 v	Current at maximum power point	2.74 A
Voltage in maximum power point	16.7 v	Nominal efficiency	0.115

The tilt angle is fixed at 45 degree with horizontal in south direction [8]. The specifications of the modules in the standard condition (1000 W/m² radiation & 25 °C temperature), are listed in Table 1 [9].

3.1.2 The Battery Bank

Due to the stochastic nature of photovoltaic system, energy storage is needed to supply the load "on demand" by storing energy during periods of high bright sun. When the total output of the PV array is more than the energy demand, the battery bank is charged. The battery used in this system consists of 57.6 kWh (12V×100Ah×48cell). The 48 V battery bank originally consisted of 57.6 kWh of storage in (12×4) sealed, valve-regulated, deep-cycle batteries.

3.1.3 The Inverter

These units turn DC power into conventional AC power, as well as offer the ability to provide backup power during a power outage. When you need to use an electrical appliance, but only have access to DC power, an inverter is perfect. The inverter used in this project is a Sunny Boy model 2500U. It is based on a power unit that operates with a very high efficiency and optimal reliability. It is designed for strings with 18 to 24 standard modules connected in series. For more detailed specifications, see Table 2 [10].

Table 2. Inverter technical characteristics (Sunny Boy model 2500)

P_{nominal}	2200 W _p	Max. AC-power	2500 W
Max input voltage	600 V	Peak inverter efficiency (η_{max})	93-94.4%
Max input current	11.2 A	AC input frequency	49.8-50.2 Hz
PV-voltage range MPPT	250-600 V	V _{AC}	198-251 V

3.1.4 Electrolyzer

Water electrolysis technology has the highest energy efficiency in non-fossil fuel based hydrogen production and is ideally suited for coupling with intermittent RE sources. In this method, electricity is used to split water into hydrogen and oxygen [11]. Water electrolysis is particularly suitable to be used in conjunction with PV array. The electrolyzer used in this project is a bipolar alkaline type. The electrolyzer module consists of 10 cells in series. The nominal operating point is rated load, 250 amperes and rated voltage, 25 V_{max}. The electrolyte (KOH) concentration inside the cells is about 28 wt. %. It had a maximum power of 5 kW and yielded about 1 Nm³/h hydrogen at normal conditions and a purity of 99.9 %. Under nominal condition, the efficiency of system is 70 %.

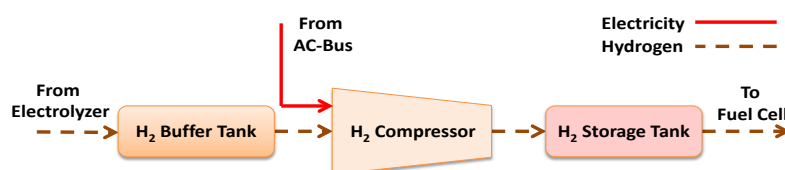


Fig. 2. Schematic of hydrogen storage system

The oxygen gas is far from pure as it leaves the electrolyzer's cells. The oxygen output of the electrolyzer still contains small amounts of hydrogen gas and vast amounts of water vapor [12-13]. The hydrogen from the electrolyzer is sent into a low-pressure tank (buffer tank) that is kept at a pressure lower than the hydrogen output pressure of the high-pressure tank as shown in Fig. 2. The intermediate reservoir system is used so that the compressor is only run when sufficient excess energy is available eliminates the use of energy from the fuel cell or enlargement of the battery bank to power the compressor. Compression occurs during compressor cycles in which the hydrogen is continuously removed from the low-pressure tanks beginning at the current pressure of the low-pressure tank and ending when the pressure

drops to a specified minimum supply pressure. The hydrogen gas is then compressed by about 10 bars by the compressor and sent for storage to hydrogen vessel.

3.1.5 Fuel cell

A fuel cell is an energy conversion device, which converts the chemical energy of a fuel and oxidant, often hydrogen and oxygen, to electrical energy. Fuel cells are similar to batteries, however, unlike battery a fuel cell must be continuously provided with fuel, rather than deriving energy from materials contained within the cell, and the products of the electrochemical reaction must be removed from the cell. They can achieve operating efficiencies approaching 60 % nearly twice the efficiency of conventional internal combustion engines [14]. The outputs of the fuel cell are DC electricity and water. Fuel cells are a very attractive option to be used with intermittent sources of generation like the PV. Their feasibility in coordination with PV systems has been successfully demonstrated for both grid-connected and stand-alone applications [15]. A PEM fuel cell was chosen because of its passive operation, high efficiency, silent and its ability to provide power quickly from a standby configuration. In this project, The Nexa™ system has 30 cells and provides up to 1.2 kW of unregulated DC power at a nominal output voltage of 26 V_{DC}. The output voltage varies with power, ranging from about 43 V at system idle to about 26 V at full load [16].

3.1.6 Hydrogen Storage

Hydrogen as an energy carrier must be stored to overcome daily and seasonal discrepancies between energy source availability and demand. Hydrogen storage has an economic advantage over lead acid batteries for long-term storage. Currently, pressurized tanks are still the most cost-effective means of hydrogen storage for most applications [17]. It is known that a stand-alone energy system needs a storage system to provide energy for the cases of inappropriate weather conditions, instantaneous overload conditions, or demand for energy after sunset [18]. In this project, hydrogen gas produced in the electrolyzer at 10 bars. This gas is stored in one hydrogen storage tank (1 m³) with a rated working pressure of 10 bars.

3.2. Advantages of the PV-Electrolysis system

There are three main reasons why the PV efficiency is lower than we had hoped. First, the MA36/45 modules are rated at 45 W but when we tested them, the average output was lower than the manufacturer claimed. Second, the various wiring connections required by code add up to an appreciable voltage drop. And finally, the electrolyzer operating voltage usually doesn't exactly match the maximum power voltage of the array. The match between the electrolyzer and PV array is an important aspect of solar hydrogen system design [19].

Advantages of the PV-Electrolysis system:

- PV modules are sold with a warranty that guarantees the power generation for typically 25 years [10].
- PV modules are an ideal power supply for an electrolyzer. The output voltage of a PV array is DC and is roughly constant with illumination level. This is a good match to the electrolyzer, which requires a constant voltage of at least 1.9 V_{DC} (for the generic considered). Increasing PV current would increase the overall volume of hydrogen produced, although it would also slightly lower the production efficiency [20].
- The water electrolysis and PV array can be sized independently and located separately.

In this system, consumption power consists of 5 kW water electrolysis and 1.5 kW hydrogen compressors. In eight hours continuous working of electrolyzer, hydrogen compressor work just three hours; therefore total of demand energy in one-work days equal to:

$$E_{total} = (P_{elec} \times h_1) + (P_{pump} \times h_2) = [(5kW) \times (8hours)] + \left[(1.5kW) \times \left(6 \times \frac{1}{2} hours\right) \right] = 44500Wh / days \quad (1)$$

The average annual global radiation for Taleghan region is 4.5 kWh/m²; Therefore power of PV system in this pilot equal to:

$$P_{PV} = \frac{44500Wh / days}{4500Wh / m^2} = 9.88kW \approx 10kW \quad (2)$$

The Depth of discharge (DOD) is defined as the amount of energy that has been removed from a battery or battery pack and usually expressed as a percentage of the total capacity of the battery. In this case, 30 % DOD means that 30 % of the energy has been discharged, so the battery now holds only 70 % of its full charge [21]. In this pilot, we used type of sealed lead acid with technical properties, 12 V and 100 Ah.

$$\text{Bank capacity} = 44500(Wh / days) \times \%130(DOD) = 57850Wh \quad (3)$$

$$\text{Bank capacity} = \frac{57850Wh}{12V} = 4820Ah \quad (4)$$

$$\text{No.Battery} = \frac{4820Ah}{100A} = 48.2 \approx 48 \quad (5)$$

3.3. Simulation solar hydrogen system with HOMER tools

National Renewable Energy Laboratory's software HOMER is used to select an optimum energy system. It also performs sensitivity analysis to evaluate the impact of a change in one or more of input parameters. Some required input information for HOMER are electrical loads, renewable resources, component technical/costs, constraints, controls, type of dispatch strategy, etc. [22]. The schematic of this system is shown in Fig. 3. Several simulation have been made by considering different capacities of PV panels, hydrogen tank, electrolyzer, battery bank, converter, fuel cell and primary load that the results of simulation, optimization and analysis for this system are described in the following sections:

- A cost of 342 \$/45 W was used, resulting in a total capital cost of 76000 \$ for a 10 kW PV array. PV array operation and maintenance (O&M) cost is considered practically zero and their lifetime is 20 years. After some preliminary runs with HOMER, it was decided that the most suitable PV size to be considered was 10 kW.
- A battery bank with a capacity of 1200 Ah (12 V, 100 A) per unit was installed. The total capacity of batteries installed was 57.6 kWh and the estimated lifetime was 5 years. The total capital cost of the battery bank was 4896 \$. Sizes of batteries considered in the optimization were: 48 and 0 kWh (no batteries).
- An AC-DC power converter unit has been installed in PV-Hydrogen system of Taleghan site. Power conditioning capital cost is around 600-800 €/kW [23]. A cost of 1350 \$/kW was chosen for Taleghan site. A lifetime of 20 years was assumed and a converter efficiency of >94%.
- The cost of hydrogen production unit integrated to the proposed PV-hydrogen cost was 2700 \$ per Nm³/h H₂. The introduction of this unit sizes (0-6.5 kW) was investigated with HOMER. The lifetime of this unit was considered as equal to 10 years.
- The capital cost of Nexa system (1.2 kW) is 5000 \$/kW for the stand-alone energy system in Taleghan site (because of its very small-scale). Fuel cell lifetime was 1500 operating

hours. Three different PEM fuel cell size (1-1.2 kW) were considered in the calculations performed with HOMER and electrical efficiency assumed constant at 38 %.

- Compressed gas storage is used for this study. Small-quantity prices are around 1500 \$/kg. A hydrogen storage tank options was investigated in the optimization process, namely 1 Nm³ (≈1kg) and the lifetime were also considered 20 years [23].
- This system has an average AC load of 31 kWh/days, with the peak load of 2.9 kWh/days. HOMER allows input of the operating reserve for the system. Result of here required the operating reserve to be 10 % of the hourly load, plus 25 % of PV power output.

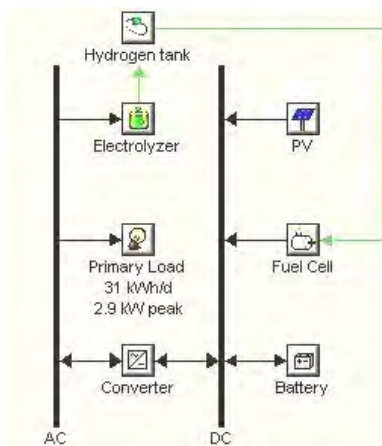


Fig. 3. Schematic of PV-Electrolyzer-Fuel cell power system

3.4. PV-hydrogen system optimization results

Actual load profile and meteorological data from the operation of the PV-fuel cell system in Taleghan site were used in this study. Hourly solar radiation measurements for a period of one year were imported into HOMER tools in order to calculate monthly average values of clearness index and daily radiation [24]. According to data from Taleghan area, the solar radiation is high, especially between June and August. The annual average global radiation is 4.5 kWh/m².day with an annual average clearness index of 0.62 and the average daily radiation is 5.095 kW h/m². The existing system was simulated in order to evaluate its operational characteristics, namely annual electrical energy production; annual electrical loads served, excess electricity, RE fraction, capacity shortage, unmet load etc. some environmental impact parameters of the system. A load-following control strategy was followed in the simulation. Under this strategy, whenever a power generator is needed it produces only enough power to meet the demand. Load following strategy tends to be optimal in systems with a surplus of renewable energy. An annual interest rate of 10 % and a project of 20 years were used in the economic calculations [24].

Table 3. Electrical production and demand for the stand-alone system

Annual Electric Energy Production		Annual Electric Energy Consumption		Other	
PV Array	18025 kWh (99%)	AC Primary Load	11116 kWh (98%)	Excess Power	4109 kWh/years
Fuel Cell	101 kWh (1%)	Electrolyzer Load	392 kWh (2%)	Capacity Shortage	157 kWh/years
Renewable Fraction	100%	Total	11508 kWh	CO ₂ Emissions	0.0619 kg/year

The results of the simulation showed that this system had a total annual electrical energy production of 18126 kWh, the RE fraction of which was ≈ 1 (i.e. 18025 kWh were produced

by the PV array). All results related to the electric energy production and electric energy consumption is summarized in Table 3. Latter is attributed to high nighttime load, which enable the operation of fuel cell because PV energy stored in batteries is not adequate to serve the load overnight. To increase renewable energy penetration excess energy can be stored in the form of compressed hydrogen and drive a PEM fuel cell.

Table 4. Distribution of annualized costs for the main components of the stand-alone energy system

Component	Initial Capital (\$)	Annualized Capital (\$/year)	Annualized Replacement (\$/year)	Annual O&M (\$/year)	Annual Fuel (\$/year)	Total Annualized (\$/year)
PV Array	76000	8927	0	0	0	8927
Fuel Cell	5000	587	88	12.1	0	687
Battery	4896	575	320	0	0	895
Converter	13650	1603	0	0	0	1603
Electrolyzer	8100	951	272	0	0	1223
Hydrogen Tank	1500	176	0	0	0	176
Other	0	0	0	0.2	0	0

The Electrical production and demand of this system are listed in Table 3. When excess PV energy is available, power is supplied first to the batteries, and then to an electrolyzer, which generate hydrogen for storage. By using HOMER it can be decided whether to use energy from the battery, fuel cell, or both based on the replacement cost and O&M of the devices. PV-Hydrogen system components are described in more detail in the following sections. Total annualized costs for each component of the stand-alone energy system are shown in Table 4. This is attributed to the fact that the lifetime of batteries is only 5 years, and the system lifetime is 20 years. Therefore the battery bank needs to be replaced several times during the project. The total net present cost (NPC) of this system at Taleghan site is around 115034 \$ and cost of energy (COE) of the proposed hydrogen system is 1.216 \$/kWh.

4. Conclusions

The replacement of conventional technologies, namely batteries by hydrogen technologies including fuel cells in RE resources based stand-alone power systems is technologically feasible. It reduces emissions, noise and fossil fuel dependence and increases RE penetration. The coupling of PV field and electrolyzer allows converting at high efficiency renewable electricity. There is no loss whatever the storage time and no need of consumption to avoid storage destruction. Using a fuel cell to get back to electricity induces a low efficiency but allows building a silent energy generator consuming no materials. New energy generators for stand-alone applications are expected to increase the comfort of people. The actual solutions are either limited by a low autonomy inducing reduction of the electricity consumption during worst seasons or noisy and using fossil energy. The coupling of a PV field and an electrolyzer allows converting at high efficiency renewable electricity into time-stable storage from pure water. Using a fuel cell to get back to electricity allows building a noiseless energy generator consuming no materials. The gas storage induces a complete autonomy during all the years and should increase the use of the renewable production. Iran country located on solar belt, so it has great potential in direct natural insolation for consuming and converting it to other types of energy. Using solar energy required high initial investment, so converting solar

energy to other types of energy with high efficiency systems is vital. Photovoltaic technology provides a reliable energy for producing hydrogen by electrolysis. Constructing this project illustrates photovoltaic system reliability, availability and being disputable in rural areas and end point of electricity yield. (Conclusion extract from) system operation conclusions shows equal real outputs, which calculated data and this, will be a start for gathering and processing information from operational parameters, in software.

References

- [1] K. Ro, S. Rahman, IEEE Transactions on Energy Conversion 13 (3), 1998, pp. 276-281.
- [2] A.M. Ramirez, P.J. Sebastian, S.A. Gamboa, M.A. Rivera, O. Cuevas, J. Campos, Int J Hydrogen Energy 25, 2000, pp. 267-271.
- [3] W. Isherwood, J.R. Smith, S.M. Aceves, G. Berry, W. Clark, R. Johnson, D. das, D. Goering, R. Seifert, Solar Energy 25, 2000, pp. 1005-1020.
- [4] Ø. Ulleberg, Solar Energy 76, 2004, pp. 323-329.
- [5] S.A. Sherif, F. Barbir, T.N. Vezirouglu, Solar Energy 78, 2005, pp. 647-660.
- [6] D.B. Nelson, M.H. Nehrir, C. Wang, Renewable Energy 31, 2006, pp. 1641-1656.
- [7] S. Busquet, F. Domain, R. Metkemeijer, D. Mayer, Ecole des Mines de Paris-Centre d'Énergétique, Rue Claude Daunesse, Les Lucioles-BP 207, F-06904 Sophia Antipolis.
- [8] Technical Catalogue of Solar Module MA36/45, Optical Fiber Fabrication Company, Iran
- [9] H. Moghbelli, R. Vartanian, International Conference on Renewable Energy for Developing Countries, 2006.
- [10] www.SMA.de
- [11] K.E. Cox, K.D. Williamson, Hydrogen: its technology and implications, Ohio: CRC Press Inc., 1977.
- [12] P. Hollmuller, J. Joubert, B. Lachal, K. Yvon, Int. J. Hydrogen Energy 25, 2000.
- [13] R. Perez, Home Power 22, 1991, pp. 26-30.
- [14] Fuel Cell Handbook, 6th ed., National Energy Technology Lab, U.S. DOE, Pittsburgh, PA, 2002.
- [15] S. Rahman and K. Tam, IEEE Transactions on Energy Conversion 3 (1), 1988, pp. 50-55.
- [16] Nexa™ (310-0027) Power Module User's Manual, MAN5100078, 2003.
- [17] J. Cotrell, W. Pratt, NREL/TP-500-34648, 2003.
- [18] E. Koutroulis, K. Kalaitzakis, Renewable Energy 28 (1), 2003, pp. 139-152.
- [19] P. Lehman, C. Parra, Solar Today, the American solar energy society, 1994, pp: 20-22
- [20] N. Nagai, M. Takeuchi, T. Kimura, T. Oka, Int. J Hydrogen Energy 28, 2003, pp. 35-41.
- [21] Solar Electric Products Catalog, August 2005.
- [22] NERL. Hybrid Optimization Model for Electric Renewable (HOMER) Available freely at (<http://www.nrel.gov/international/tools/HOMER/homer.html>).
- [23] E.I. Zoulias, N. Lymberopoulos, Renewable Energy 32, 2007, pp. 680-696.
- [24] RETScreen™ database, URL: www.etscreen.net.

Two Dimensional PEM Fuel Cell Modeling at Different Operation Voltages

Mohammad Ameri*, Pooria Oroojie

Energy Eng. Department, Power & Water University of Technology, Tehran
* Tel: +98 2173932653, Fax: +98 2177311446, E-mail: ameri_m@yahoo.com

Abstract: This paper presents a comprehensive, consistent and systematic mathematical modeling for PEM fuel cells that can be used as the general formulation for the simulation and analysis of PEM fuel cells. As an illustration, the model is applied to an isothermal, steady state, two-dimensional PEM fuel cell at different operation voltages to investigate the fuel cells performance parameters such as the mass concentration, the velocity distribution of reactant, current density distribution, and polarization curve. The model includes the transport of gas in the gas flow channels, electrode backing and catalyst layers; the transport of water and hydronium in the polymer electrolyte of the catalyst and polymer electrolyte layers; and the transport of electrical current in the solid phase. Water and ion transport in the polymer electrolyte has been modeled using the generalized Stefan–Maxwell equations. Moreover, the reactant gas flow in the gas channel has been modeled by continuity and the steady state incompressible Navier-Stokes equations. All of the model equations are solved with finite element method using commercial software package COMSOL Multi physics. The results from PEM fuel cell modeling at different operation voltages are then compared with each other and finally according to the results, the strategy to improve fuel cell performance with the target of reducing cost is introduced.

Keywords: PEM fuel cell, Mathematical modeling, Finite element, COMSOL multi physic

1. Introduction

Fuel cells and hydrogen technology represent the most promising alternative pathway for automotive and stationary applications. The PEMFC offers low to zero emission from sub-watt to megawatt power generation, for applications in transportation, industries and portable supplies units [1, 2]. In this paper, we focus on the role of computational tools in order to verify some experimental results and demonstrate the better performance of PEMFC constructed by application of optimizations techniques. Experimental research and numerical simulation have been used in fuel cell design in order to improve the performance of fuel cells. The experimental data will be useful to validate the model.

The search for reliable computational models is a challenge because it involves several transport phenomena: multi-component, multi phase and multi-dimensional flow processes, electrochemical reactions, convective heat and mass transport in flow channels, diffusion of reactants through porous electrodes, transport of water through the membrane and transport of electrons through solid matrix. The Computational Fluid Dynamic (CFD) is a very useful tool to simulate hydrogen and oxygen gases flow channels configurations, reducing the costs of bipolar plates' production and optimizing mass transport [3-5].

The computational models are efficient in predicting the cell performance under a variety of design parameters. Fuel cell models can be classified into 1D, 2D and 3D according to dimensions. The accuracy of 1D model [6,7] is sacrificed due to some assumptions made in order to simplify the problem to 1D. A 3D model simulates the reactant gas flow in the directions along the flow channel and perpendicular to the flow channel simultaneously, which results in more accurate results but requires longer computational time and larger computing capacity facility [8, 9]. A 2D fuel cell model [10,11] combines the benefits of 1D and 3D models and gains its popularity in PEM fuel cell modeling due to its higher computational efficiency compared to 3D models and better simulation accuracy compared to 1D model. A two-dimensional mathematical model of a PEM fuel cell can be conducted in two different modes: parallel or perpendicular to the gas flow direction in the gas channel

while the other modeling dimension is across the membrane in both cases. Models conducted in the first mode (parallel to the gas flow direction) consider the influence of fluid behavior in the channel; while in the second mode (perpendicular to the gas flow direction) the interdigitated flow pattern can be easily investigated. The goal of the present work is to develop 2D isothermal, steady state PEM fuel cell models in perpendicular to the gas flow direction to investigate the performance of fuel cells such as the mass concentration and velocity distribution of reactants, polarization curve, output power density at different operation voltages so that one can examine the influence of operation voltage on those items.

2. Modeling

Fig. 1 schematically shows a 3D single PEMFC and its various components including the membrane, flow channels, gas diffusion layers and catalyst layers on both anode and cathode sides. To conduct a 2D simulation, there are two options to choose the modeling geometry: one is in x-z plane as shown in Fig. 2(a), and the other is in x-y plane as shown in Fig. 2(b). The geometry which is shown in Fig. 2 (b) will be studied in this paper.

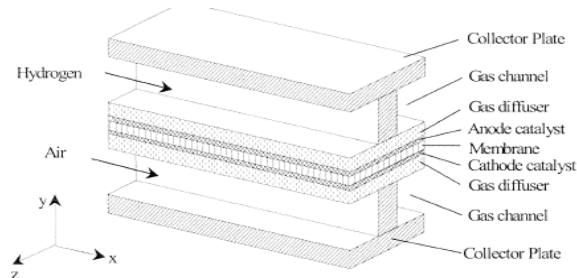


Fig.1. Three dimensional diagrams of a PEMFC and its various components.

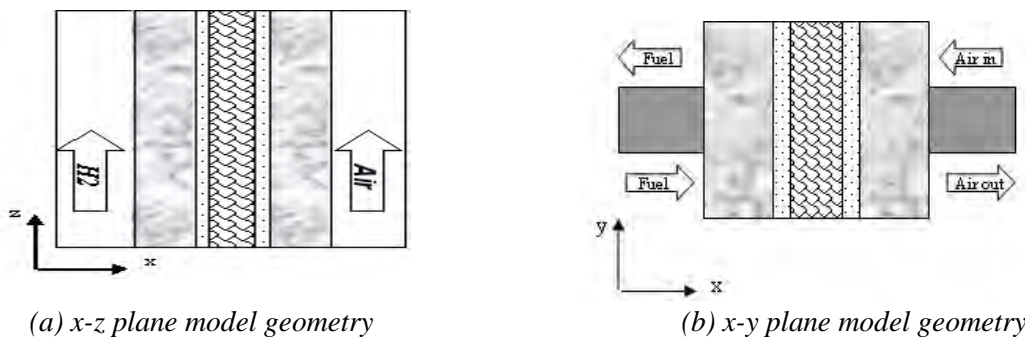


Fig.2. Two-dimensional PEM fuel cell modeling geometry.

2.1. Model Definition

The modeled section of the fuel cell consists of three domains: an anode (Ω_a), a proton exchange membrane (Ω_m), and a cathode (Ω_c) as indicated in Fig. 3(a). Each of the porous electrodes is in contact with an interdigitated gas distributor, which has an inlet channel ($\partial\Omega_{a, \text{inlet}}$), a current collector ($\partial\Omega_{a, \text{cc}}$), and an outlet channel ($\partial\Omega_{a, \text{outlet}}$). The same notation is used for the cathode side. The model geometry is shown in Fig. 3(b).

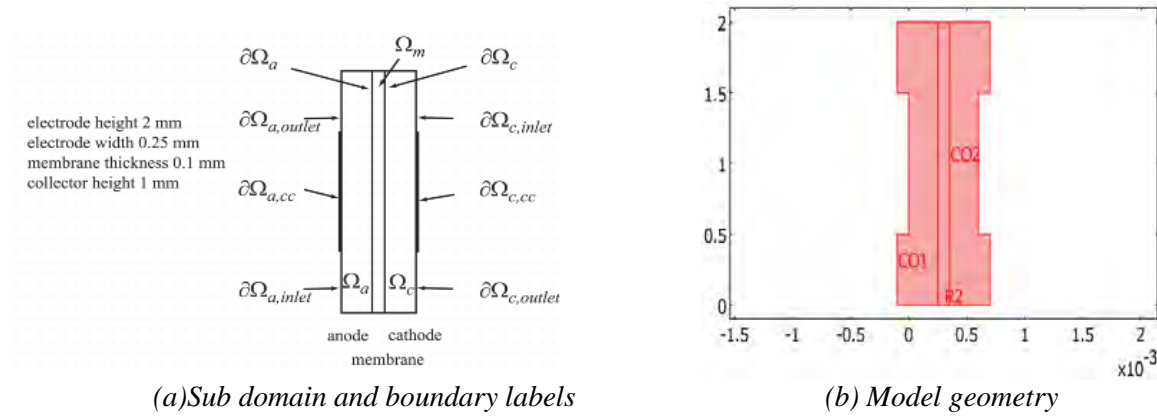


Fig.3. Model geometry with sub-domain and boundary labels.

2.2. Governing Equations

2.2.1. Flow Channels

Based on the model assumptions, the reactant gas flow in the gas channel is governed by the continuity equation to insure the mass conservation as well as the steady state incompressible Navier-Stokes equation to describe the momentum conservation of Newtonian fluids. The multi-component diffusion and convection in flow channels are described by the Maxwell-Stefan equation. It solves for the fluxes in terms of mass fraction. The general form of the Maxwell-Stefan equation is shown below.

$$\frac{\partial}{\partial t} \rho \omega_i + \nabla \cdot [-\rho \omega_i \sum_{j=1}^N D_{ij} \left\{ \frac{M}{M_j} (\nabla \omega_j + \omega_j \frac{\nabla M}{M}) + (x_j - \omega_j) \frac{\nabla P}{P} \right\} + \rho \omega_i u] = R_i \quad (1)$$

Where D_{ij} (m^2/s) is the diffusion coefficient; R_i ($kg/m^3 \cdot s$) is the reaction rate and it is zero in the flow channel; x is the mole fraction; ω is the mass fraction; M (kg/mol) is the molecular mass; The subscript i (or j) represents each species of hydrogen and water on the anode side, and oxygen, water, nitrogen on the cathode side. On the cathode side, the transport equations are solved for two species since the third species can always be obtained from the mass balance equation given as the following:

$$w_{N_2} = 1 - w_{O_2} - w_{H_2O} ; w_{H_2O} = 1 - w_{H_2} \quad (2)$$

2.2.2. Gas diffusion layers and catalyst layers

Since gas diffusion layers (GDL) and catalyst layers are porous media, the velocity distribution is therefore formulated by Darcy's law and mass conservation equation.

$$u = -\frac{\kappa}{\mu} \nabla p \quad (3)$$

$$\nabla \cdot (\rho u) = S \quad (4)$$

Where κ (m^2) is the permeability; and μ ($Pa \cdot s$) is the dynamic viscosity. S is the source term, $kg/(m^3 \cdot s)$. The continuity equation for the gas flow mixture describes the sum of all the involved gas species at each side. The source term, S , accounts for the total consumption and

production during the electrochemical reactions. In the catalyst layer, the reaction rate R_i corresponding to each species is given as:

$$R_{H_2} = -\frac{j_a}{2F} M_{H_2}; R_{O_2} = -\frac{|j_c|}{4F} M_{O_2}; R_{H_2O} = \frac{|j_c|}{4F} M_{H_2O} \quad (5)$$

2.2.3. Current transport

The continuity of current in a conducting material is described by:

$$\nabla \cdot i = \nabla \cdot i_s + \nabla \cdot i_e = 0 \quad (6)$$

Protons travel through the ionic conductor (the membrane) to form an ionic current denoted by i_e while electrons can only be transferred through the solid matrix of electrodes which results in an electronic current denoted by i_s . The potential equations for both solid and electrolyte phases are obtained by applying Ohmic's law to Eq. (6).

$$\text{Electron transport: } \nabla \cdot (-\sigma_s \nabla \phi_s) = S_s; \text{ Proton transport: } \nabla \cdot (-\sigma_e \nabla \phi_e) = S_e \quad (7)$$

Where ϕ is the phase potential, V; σ (s/m) is the effective electric conductivity; S (A/m^3) is the current source term; the subscript s denotes the property of a solid phase and e denotes the property of an electrolyte phase. The source terms in the electron and proton transport equations, result from the electrochemical reaction occurring in the catalyst layers of anode and cathode sides.

$$\begin{aligned} \text{Anode Catalyst Layer: } S_e = j_a; S_s = -j_a, \\ \text{Cathode Catalyst layer: } S_e = j_c; S_s = -j_a \end{aligned} \quad (8)$$

Where j_a and j_c are the transfer current density corresponding to the electrochemical reaction at the anode and cathode catalyst layers, which is formulated by the agglomerate model. In the catalyst layers, the agglomerate is formed by the dispersed catalyst, and this zone is filled with electrolyte. Oxygen is dissolved into the electrolyte and reaches the catalyst site. The agglomerate model describes the transfer current density as following [12]:

Anode:

$$\begin{aligned} j_a = -\frac{6(1-\varepsilon)FD_H^{agg}}{(R^{agg})^2} (C_H^{agg} - C_H^{ref} \exp(-\frac{2F}{RT}\eta)) \cdot \\ (1 - \sqrt{\frac{j_{o,a^s}}{aFC_H^{ref} D_H^{agg}} R^{agg}} \coth \sqrt{\frac{j_{o,a^s}}{aFC_H^{ref} D_H^{agg}} R^{agg}}) \end{aligned} \quad (9)$$

Cathode:

$$\begin{aligned} j_c = R \frac{12(1-\varepsilon)FD_O^{agg}}{(R^{agg})^2} C_O^{agg} \cdot (1 - \sqrt{\frac{j_{o,c^s} (R^{agg})^2}{4FC_O^{ref} D_O^{agg}} \exp(-\frac{0.5F}{RT}\eta)}) \cdot \\ \coth \sqrt{\frac{j_{o,c^s} (R^{agg})^2}{4FC_O^{ref} D_O^{agg}} \exp(-\frac{0.5F}{RT}\eta)} \end{aligned} \quad (10)$$

where C^{agg} (mol/m^3) is the gas concentration at the surface of the agglomerates; C_{ref} (mol/m^3) is the dissolved gas concentration at a reference state; D^{agg} (m^2/s) is the diffusion coefficient of the dissolved gas inside the agglomerate; R^{agg} (m) is the agglomerate radius; j_0 (A/m^2) is the exchange current density; s (m^2/m^3) is the specific surface area; η (V) is the electrochemical over potential which is expressed by the potential difference between solid matrix and electrolyte and is defined as:

$$\begin{aligned} \text{Anode side : } \eta &= \phi_s - \phi_e ; \text{ Cathode side: } \eta = \phi_s - \phi_e - U_{oc} \\ \text{Open-Circuit Potential: } U_{oc} &= 1.23 - 0.9 \times 10^{-3} (T-298) \end{aligned} \quad (11)$$

The dissolved gas concentration at the surface of the agglomerates is corresponding to the molar fraction in the gas phase through Henry's Law:

$$C^{agg} = \frac{C_{gas} P}{H} \quad (12)$$

Where H ($\text{Pa} \cdot \text{m}^3 / \text{mol}$) is the Henry's constant.

2.3. Numerical Procedure

COMSOL Multiphysics, which is a commercial solver based on the finite element technique, is used to solve the governing equations. The stationary nonlinear solver is used since the source terms of the current conservation equation make the problem non-linear. Furthermore, the convergence behavior of this non-linear solver is highly sensitive to the initial estimation of the solution. To accelerate the convergence, the following procedures are adopted. The Conductive Media DC module is firstly solved based on the initial setting. Secondly, Darcy's Law and Incompressible Navier-Stokes modules are solved together using the results from the previous calculation as initial conditions. After the previous two modules converge, all the coupled equations including Maxwell-Stefan Diffusion and Convection module are solved simultaneously until the convergence is obtained.

3. Results and Discussion

Using the aforementioned procedures, the x-y geometry as described in Fig. 2(b) simulated in different voltages. The parameters values that used in this study are extracted from [13]. The x-y model represents the PEM fuel cell with interdigitated channels on the bipolar plate. Fig.4 shows the current density curve obtained from the x-y model at the anode active layer for a given operation voltage of 0.7.

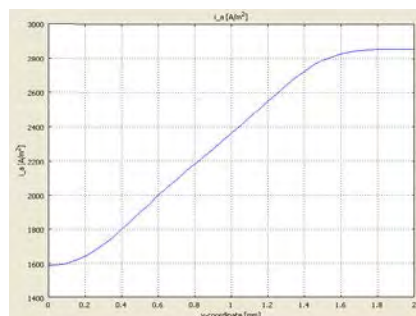


Fig.4. Current-density distribution at the anode active layer.

The current density is uneven with the highest density in the cell's upper region. This means that the oxygen-reduction reaction rate in the cathode determines the current-density distribution. The maximum current density arises close to the air inlet. Figure 5 shows the current distribution in the PEM fuel cell for a given operation voltages of 0.7 and 0.6. There are significant current spikes present at the corners of the current collectors and this trend will be more sensible at low voltages. The convective fluxes generally dominate mass transport in the cell. To study the convective effects, the velocity field is plotted in Fig.6. The flow-velocity magnitude attains its highest values at the current collector corners and it is more evident at lower operation voltages.

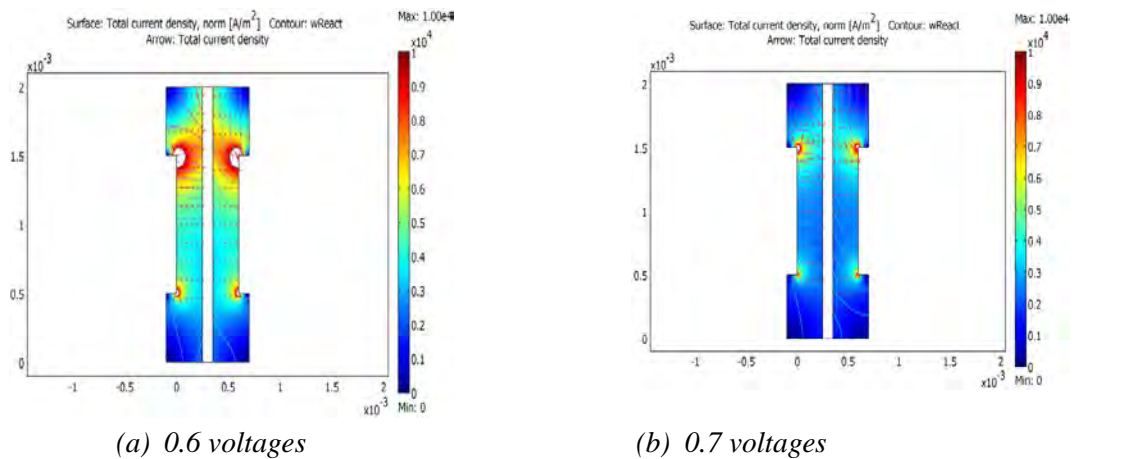


Fig.5. Current density (surface plot) and current vector field (arrow plot).

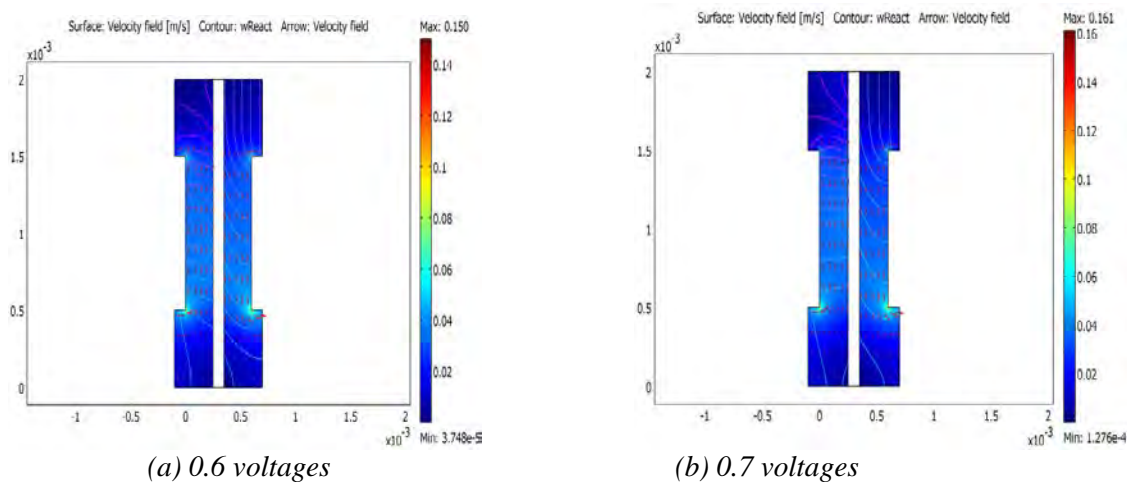


Fig.6. Gas velocity field in the anode and cathode compartments.

Figure 7 shows the reactant (oxygen and hydrogen) weight fractions in the cathode and anode gases. It is interesting to note that the hydrogen fraction increases as the anode gas flows from the inlet (at the bottom) to the outlet (at the top). This is the result of the electro osmotic drag of water through the membrane, which results in a higher flux than the consumption of hydrogen. This means that the resulting convective flux of anode gas towards the membrane causes the weight fraction of hydrogen to go up. In the cathode gas, there is an expected decrease in oxygen content along the flow direction and a small change in the oxygen flow gives a substantial change in cell polarization. Figure 8 depicts the water mass fraction in the anode and cathode gases as well as the diffusive flux of water in the anode. It is clear that water is transported through diffusion and convection to the membrane on the anode side.

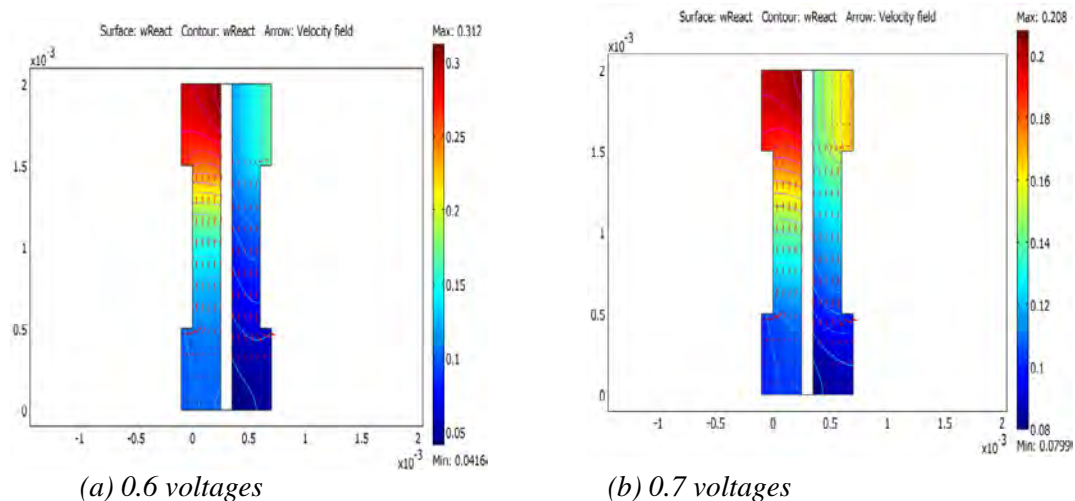


Fig.7. Normalized Reactant mass fractions, on the anode side (left) and cathode side (right).

The results show a minimum occurs at the upper corner of the membrane on the anode side that limit fuel cell performance. If the anode gas becomes too much dry, the membrane dries out, resulting in a decrease in ionic conductivity and failure of fuel cell. On the other hand, at the cathode side the water levels increase with the direction of flow and a local maximum in water current occurs at the lower corner of the membrane. This may also be critical since the water droplets can clog the pores and effectively hinder gas transport to the active layer.

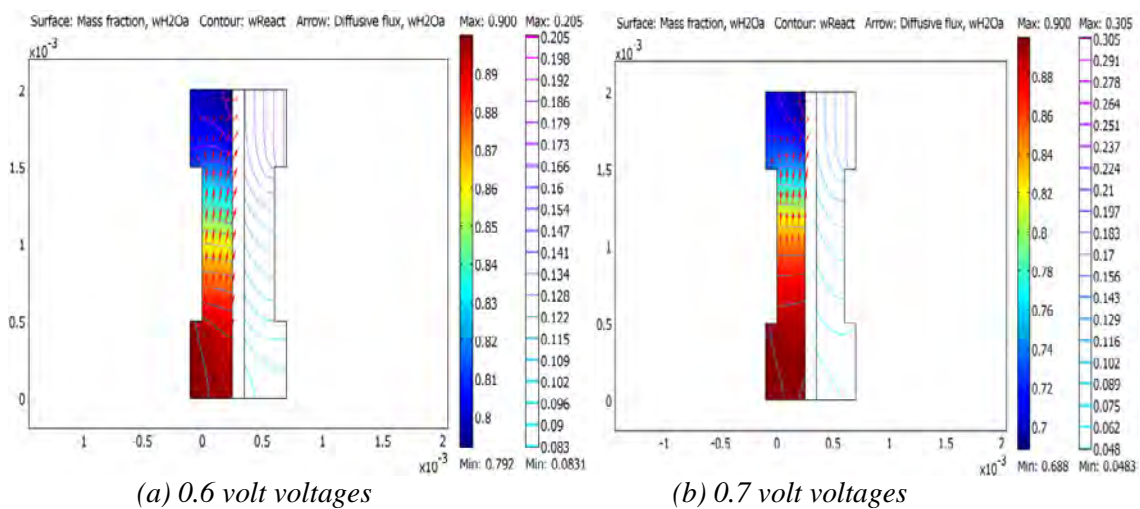


Fig.8. Water mass fraction in the anode (left, surface plot) and the cathode (right, contour plot). The arrows visualize the diffusive flux vector field on the anode side.

4. Conclusion

Two-dimensional, single-phase and isothermal models of PEM fuel cells have been developed at two different operation voltages. The model is able to investigate the transport phenomena and electrical potential distribution for the various PEM fuel cell components including the gas channels, gas diffusion layers, catalyst layers and membrane. The current density curve has been presented. The x-y model used to study the fuel cell with interdigitated channels design, shows that the fuel mass fraction decreases faster when the cell works at low voltage and high current density. The potential distribution indicates a major potential drop across the membrane. Moreover, a higher over potential on the cathode catalyst layer is noted. A minimum water mass fraction at upper corner of the membrane on anode side, reveals that

this phenomenon is more sensible at low voltages. The flow velocity magnitude attains its highest value at the current collector corners and it is more intensified at low voltages.

References

- [1] N. Djilali, Computational modeling of polymer electrolyte membrane (PEM) fuel cells, *Challenges and Opportunities Energy*, 2006, pp.1006-1016.
- [2] E.F. Cunha, A.B. Andrade, E. Robalinho, M.L.M. Bejarano, E. Cekinski, M. Linardi, Modeling and simulation of PEM fuel cell's flow channels using CFD techniques, *Proceeding of International Nuclear Atlantic Conference*, 2007, pp.107-123.
- [3] P.T. Nguyen, T. Berning, N. Djilali, Computational model of PEM fuel cell with serpentine gas flow channels, *Journal of Power Sources*, 130, 2004, pp.149-157.
- [4] S. Karvonen, T. Rottinen, J. Saarinen, O. Himanen, Modeling of flow field in polymer Electrolyte membrane fuel cell, *Journal of Power Sources*, 161, 2006, pp. 876-884.
- [5] G. Squadrito, O. Barbera, I. Gatto, G. Giacoppo, F. Urbani, E. Passalacqua, CFD analysis of the flow field scale-up influence on the electrodes performance in a PEFC, *Journal of Power Sources*, 152, 2005, pp. 67-74.
- [6] T.E. Springer, T.A. Zawodzinske, S. Gatteadold, Polymer Electrolyte Fuel Cell Model, *Journal of Electrochem Soc.*, 138, 2000, pp. 2334-2342.
- [7] V. Gurau, F. Barbir, H. Liu, An Analytical Solution of a Half-Cell Model for PEM Fuel Cell, *Journal of the Electrochemical Society*, 147, 2000, pp. 2468-2477.
- [8] T. Berning, D.M. Lu, N. Djilali, Three-dimensional computational analysis of transport phenomena in a PEM fuel cell, *Journal of Power Sources*, 106, 2004, pp. 284-294.
- [9] K. Haraldsson, K. Wipke, Evaluating PEM fuel cell system models, *Journal of Power Sources*, 126, 2004, pp. 88-97.
- [10] D.J. Nelson, M.R. Spakovsky, Single domain PEMFC model based on Siegel Siegel agglomerate catalyst geometry, *Journal of Power Sources*, 115, 2003, pp. 81-89.
- [11] A. Biyikoglu, Review of proton exchange membrane fuel cell models, *International Journal of Hydrogen Energy*, 30, 2007, pp. 1181-1212.
- [12] K. Broka, Characterization of the Components of the Proton Exchange Membrane Fuel Cell, Technical licentiate Thesis, Royal Institute of Technology, Stockholm, Sweden, 1995, pp. 93-107.
- [13] H. Meng, C.Y. Wang, Model of Two Phase Flow and Flooding Dynamics in PEMFC, *Journal of the Electrochemical Society*, 152, 2005, pp.1733-1741.

Effect of type and concentration of substrate on power generation in a dual chambered microbial fuel cell

A.A. Ghoreyshi^{1,*}, T.Jafary¹, G.D. Najafpour¹, F.Haghpour¹

¹Chemical Engineering Department, Babol University of Technology, Babol, Iran

* Corresponding author. Tel: 00981113234204, Fax: 00981113234204, E-mail: aa_ghoreyshi@nit.ac.ir

Abstract: Microbial fuel cell, as a new technology for energy generation, has gained a lot of attention in converting a wide range of organic and inorganic substrates to bioelectricity in recent years. Substrate as the fuel of MFCs has an effective role on the performance of MFCs. To investigate the effect of type and concentration of substrate on the MFC performance, glucose and date syrup were examined over a concentration range of 2-20 g.l⁻¹. Date syrup or any waste of date could be used as a natural substrate while glucose is considered as a synthetic carbon source. In this research a two-rectangular chambered MFC separated by a Nafion 112 proton exchange membrane, was constructed. The anodic compartment was inoculated by *saccharomyces cerevisiae* as biocatalyst. 200 $\mu\text{mol.l}^{-1}$ of neutral red as the anodic mediator and 300 $\mu\text{mol.l}^{-1}$ of potassium ferricyanide as oxidizer were added to anode and cathode chambers, respectively. The results has shown that 3 g.l⁻¹ date syrup-fed- MFC had the highest power density, 51.95 mW.m⁻² (normalized to the geometric area of the anodic membrane, which was 9 cm²), corresponding to a current density of 109.0384 mA.m⁻² and a MFC voltage of 967 mV.

Keywords: Microbial fuel cell, Substrate, Glucose, Date syrup, Power density.

1. Introduction

The microbial fuel cells convert the chemical content in organic and inorganic compounds to electricity via catalytic activity of microorganisms as the biocatalyst. Oxidation of substrate in anode chamber by microorganisms results in proton and electron production. Protons are transferred to cathode chamber through proton exchange membrane [1-3]. Depending on the type of electron transfer mechanisms, MFCs are categorized to two main groups, i.e. MFCs using mediator and mediator less MFCs [4].

Proton exchange system [5], electrode type and distance [6], temperature [7], pH [8], inoculums [9] and substrate [10, 11] as the main effective parameters on MFCs performance were investigated by many researchers. The substrate, as a key parameter, influences the integral composition of the bacterial community in the anode biofilm, and the MFC performance including the power density (PD) and Coulombic efficiency (CE) [12]. MFCs have been solely considered as a bioelectricity generation method, until different wastewaters were utilized as the fuel in anode chamber for the wastewater treatment [13]. Wide varieties of substrates ranging from pure compounds to complex mixture of organic matters present in wastewater have been used in MFCs as the carbon source for bioelectricity generation as well as wastewater treatment purposes. Acetate [14] and glucose [15] as the most common substrates, sucrose [16], xylose [17] and various types of wastewater like synthetic [18], domestic [19], brewery [20], swine [21] and paper recycling wastewater [22] with different concentrations have been studied by many researchers. But it is difficult from literature to compare MFCs performances, due to different operating conditions such as surface area, type of electrodes and different microorganisms used. The main purpose of this article was to investigate the effect of two types of substrates, i.e. glucose and date syrup, as well as their concentration on the MFC electrical performance in a dual chambered fuel cell. Date is one of the main products of desert regions and its application as a substrate for MFCs in environmental biosensors in remote areas could be considered. A comparison was made by

the measurement of polarization curve under various concentrations for both types of substrates. Different concentrations ranging from 2- 20 g.l⁻¹ were chosen, while all other conditions kept constant.

2. Methodology

Saccharomyces cerevisiae PTCC 5269 was supplied by Iranian Research Organization for Science and Technology, Tehran, Iran. The microorganisms were grown in an anaerobic jar. The general medium for seed culture of both, Glucose-fed and date syrup-fed MFCs, consisted of yeast extract, NH₄Cl, NaH₂PO₄, MgSO₄ and MnSO₄: 3, 0.2, 0.6, 0.2 and 0.05 g.l⁻¹, respectively. Glucose and date syrup as the carbon sources were added to this medium in a range 1-20 g.l⁻¹. Due to high concentration of date syrup, date syrup was pretreated with different methods to break all its complex mixture to glucose. It was diluted, hydrolyzed with hydrochloric acid and then autoclaved for several times till getting constant sugar content. These processes convert all its sugar content to glucose. The medium then was sterilized, autoclaved at 121°C and 15psig for 20 min.

The medium pH was initially adjusted to 6.5 and the inoculum was introduced into the media at ambient temperature. The inoculated cultures were incubated at 30°C. The bacteria were fully grown for the duration of 24 hours in 100 ml flux without any agitation. Substrate consumption was calculated based on determination of the remained sugars in the culture. All chemicals and reagents used for the experiments were analytical grades and supplied by Merck (Germany). The pH meter, HANA 211(Romania) model glass-electrode was employed for the pH measurements of samples in the aqueous phase. The initial pH of the working solutions was adjusted by addition of dilute HNO₃ or 0.1M NaOH solutions. DNS reagent was developed to detect and measure substrate consumption using colorimetric method [23] and cell growth was also monitored by optical density using spectrophotometer (Unico, USA).

The fabricated cells in the laboratory scale were made of Plexiglas material. The volume of each chamber (anode and cathode chambers) was 800 ml with working volume of 600 ml (75% of total volume). The sample port was provided for the anode chamber, wire point inputs and inlet port. The selected electrodes in MFC were graphite felt in size of 50×35×2 mm. Proton exchange membrane (PEM; NAFION 112, Sigma–Aldrich) was used to separate two compartments. The Nafion area separated the chambers was 3.79 cm². Nafion as a proton exchange membrane was subjected to a course pretreatment to take off any impurities that was boiling the film for 1h in 3% H₂O₂, washed with deionized water, 0.5 M H₂SO₄, and then washed with deionized water. The anode and cathode compartments were filled by deionized water when the biological fuel cell was not in use to maintain membrane for good conductivity. Natural Red and Ferricyanide were supplied by Merck (Germany). These chemicals in optimum concentrations (200 μmol.l⁻¹ & 300 μmol.l⁻¹) were used as mediators in anode and cathode of MFC, respectively.

S.cerevisiae used as a biocatalyst in microbial fuel cell for production of bioelectricity from carbohydrate source. This microorganism was grown under anaerobic condition in biofuel cell. Fixed incubation time and enriched media was used. The obtained data has shown that *S.cerevisiae* had good ability for consumption of substrate at anaerobic condition

The schematic diagram and illustration of the fabricated experimental set up with auxiliary equipments are shown in Fig. 1.

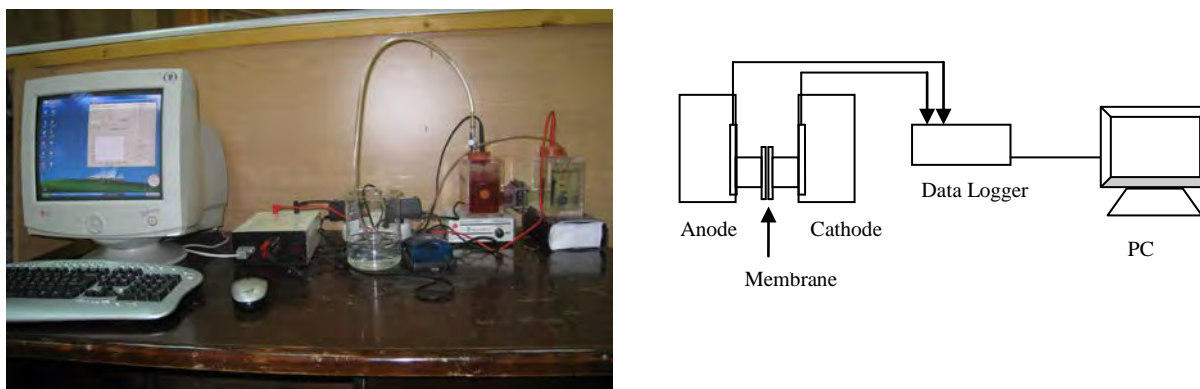


Fig. 1. The schematic diagram and illustration of the fabricated experimental set up with auxiliary equipments

3. Results and discussion

As the MFC were inoculated with *S.cerevisiae*, the voltage was continuously monitored by a data acquisition system to reach the constant open circuit voltage (OCV). It took 42, 57, 67, 65, 58, 48 and 30 hours for glucose with concentration of 1, 3, 5, 7, 10, 20 and 30 g.l⁻¹ to reach constant voltage of 922, 957, 970, 955, 920, 800mV respectively, These results were 64, 67, 72, 68, 64, 52 and 40 hours for the same concentrations of date syrup with the constant OCV of 988, 985, 948, 922, 916, 656 mV respectively. The results indicated that an increase in the substrate concentration increased the time needed to reach constant OCV at low concentration of 1-5 g.l⁻¹ for glucose and 1-3 g.l⁻¹ for date syrup.

Polarization curves were recorded by the data acquisition system after the mentioned time duration when the constant OCV was achieved. Fig. 2 shows polarization curves of the MFC at the glucose concentration range of 1-20 g.l⁻¹. As the glucose concentration increased from 1 to 5g.l⁻¹, power and current density gradually increased. However when the glucose concentration increased from 7 to 20g.l⁻¹, it was observed that the power and current density were considerably decreased. That was because the most of glucose remained unconsumed at high concentrations. The increase in time duration to reach constant OCV at low concentrations of 1-5 g.l⁻¹ for glucose and 1-3 g.l⁻¹ for date syrup, and subsequently the decrease at higher concentrations, 7-20 g.l⁻¹ for glucose and 5-20 g.l⁻¹ for date syrup, can be also attributed to the substrate inhibition effect. Indeed, all carbon sources available in the substrate solution at low concentrations were consumed resulted in longer time for attaining constant OCV. However as the substrate concentration increased, the constant OCV was achieved earlier with lower outputs, due to limitation in consuming carbon content in the substrate at higher concentration by microorganisms.

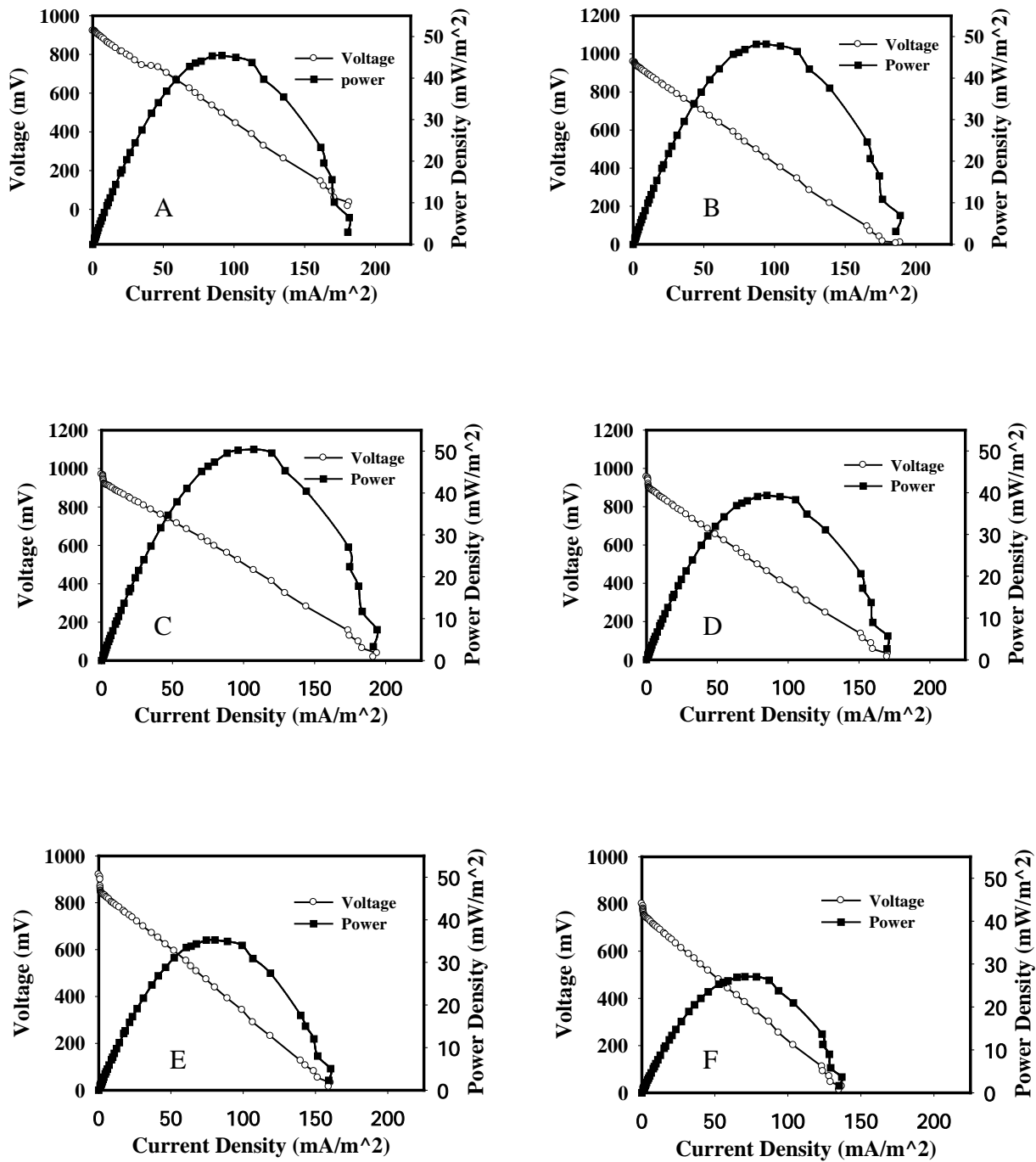


Fig. 1. Effect of different glucose concentrations on polarization curves

A) 1 g.l⁻¹, B) 2 g.l⁻¹, C) 5 g.l⁻¹, D) 7 g.l⁻¹, E) 10 g.l⁻¹, F) 20 g.l⁻¹

Fig. 3 shows polarization curves for the date syrup at the same concentration range. Comparing the results shown in Figure 2 and 3, the best results were achieved at the concentration 3 g.l⁻¹ of date syrup with the maximum power 53.7031 mW.m⁻² and current density 110.86 mA.m⁻². These results were followed by 5 g.l⁻¹ of glucose (50.41 mW.m⁻², 107.16 mA.m⁻²), 5 g.l⁻¹ of date syrup (49.51 mW.m⁻², 195.19 mA.m⁻²), 3 g.l⁻¹ of glucose (48.23 mW.m⁻², 94.16 mA.m⁻²) and 1 g.l⁻¹ of date syrup (47.36mW.m⁻², 104.12 mA.m⁻²).

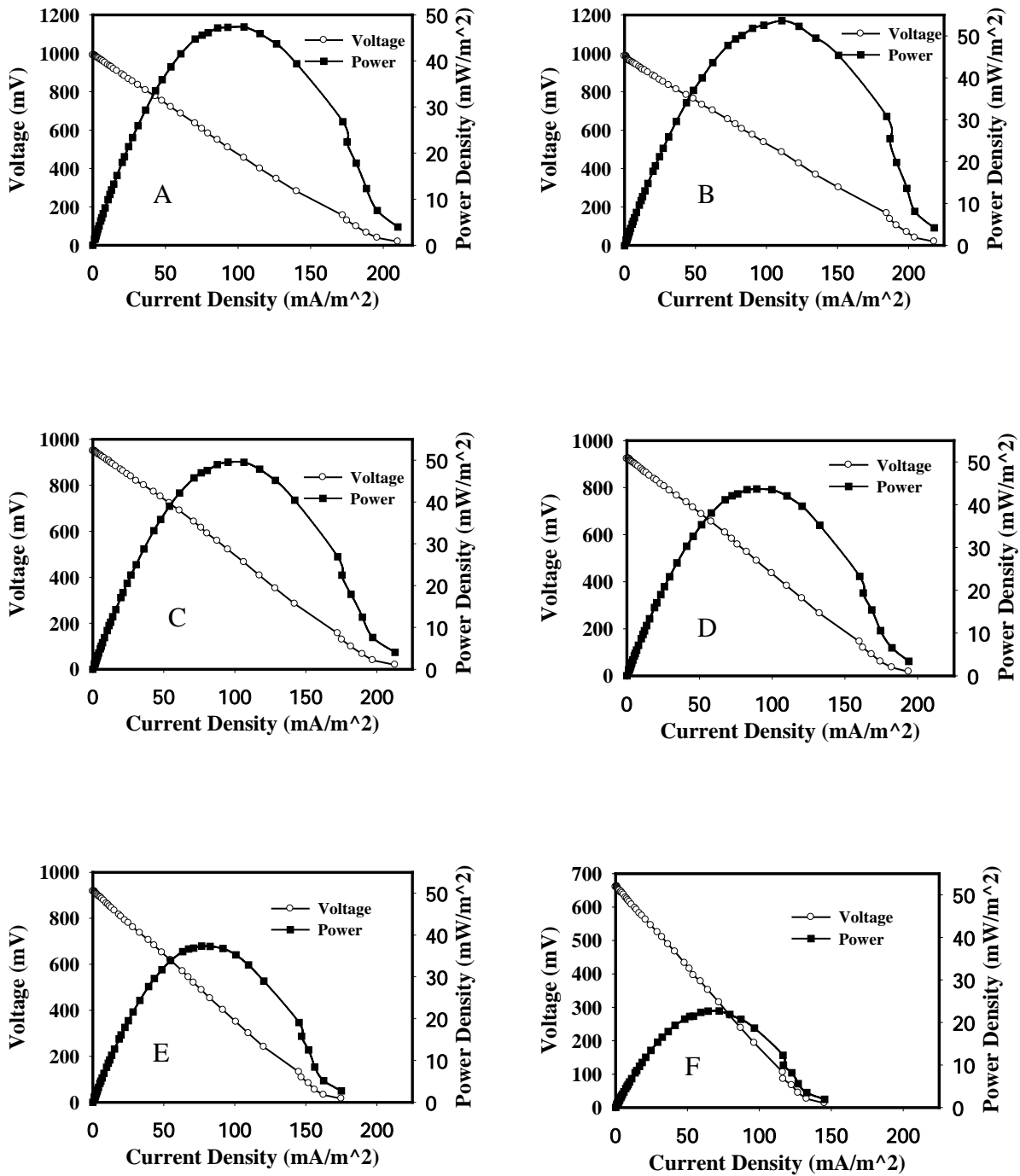


Fig. 3. Effect of different date syrup concentrations on polarization curves

1 g.l⁻¹, B) 2 g.l⁻¹, C) 5 g.l⁻¹, D) 7 g.l⁻¹, E) 10 g.l⁻¹, F) 20 g.l⁻¹

Fig. 4 compares the power and current output for the two types of substrates used in this study at their optimum concentration. The Figure indicates a superior electrical performance for the date syrup compared to the glucose.

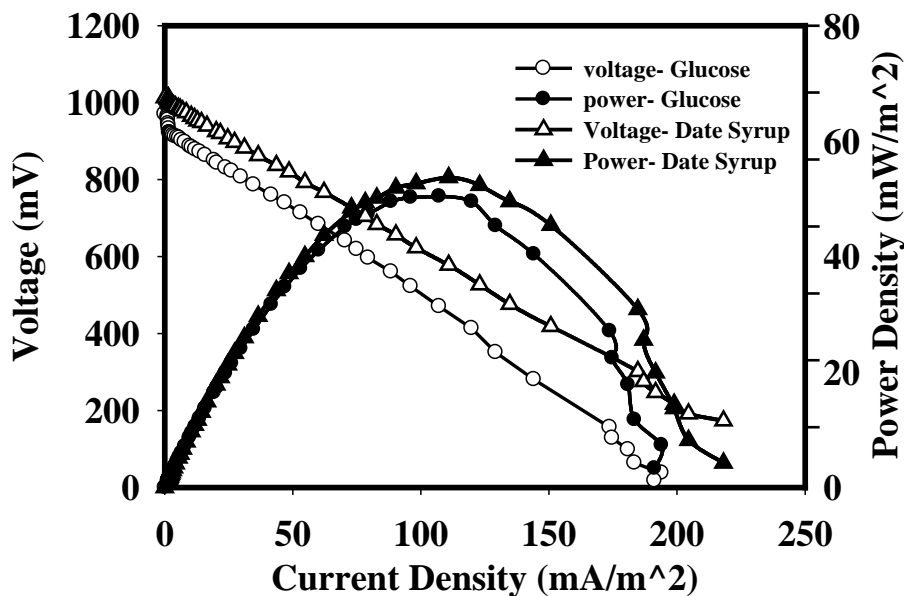


Fig. 4. Comparison of the MFC electrical performance working with glucose and date syrup as substrate at optimum concentration

4. Conclusions

In this study the effect of substrate type and concentration on the performance of microbial fuel cells was investigated. The glucose and date syrup were utilized as the carbon source for the production of electrical energy by means of *Saccharomyces cerevisiae* as the biocatalyst. Several concentrations of glucose and date syrup at the range of 1-20 g.l⁻¹ were experimented in a two-chambered fabricated MFC. The results revealed that the optimum concentration with the highest electrical performance were 3 g.l⁻¹ for date syrup and 5 g.l⁻¹ for glucose. Comparing the two types of substrates used in this study, date syrup has shown a superior electrical performance. The best results was achieved using the date syrup at optimum concentration of 3 g.l⁻¹ with the maximum power 53.7031 mW.m⁻² and current density 110.86 mA.m⁻². The results also indicated that the substrate inhibition effect may have a significant role in the performance of MFC at high concentration of glucose and date syrup.

References

- [1] Z. D. Liu and H. R. Li, Effects of bio-and abio-factors on electricity production in a mediatorless microbial fuel cell, *Biochemical Engineering Journal* 36, 2007, pp. 209-214.
- [2] M. S. Kim and Y. Lee, Optimization of culture conditions and electricity generation using *Geobacter sulfurreducens* in a dual-chambered microbial fuel-cell, *International Journal of Hydrogen Energy* 35, 2010, pp. 13028-13034.
- [3] A. Larrosa, L. J. Lozano, K. P. Katuri, I. Head, K. Scott, and C. Godinez, On the repeatability and reproducibility of experimental two-chambered microbial fuel cells, *Fuel* 88, 2009, pp. 1852-1857.
- [4] X. Tang, Z. Du, and H. Li, Anodic Electron Shuttle Mechanism Based on 1-Hydroxy-4-Aminoanthraquinone in Microbial Fuel Cells, *Electrochemistry Communications* 12, 2010, pp. 1140-1143.
- [5] K. Chae, M. Choi, F. Ajayi, W. Park, I. Chang, and I. Kim, Mass Transport through a Proton Exchange Membrane (Nafion) in Microbial Fuel Cells†, *Energy & Fuels* 22, 2007, pp. 169-176.
- [6] F. Li, Y. Sharma, Y. Lei, B. Li, and Q. Zhou, Microbial Fuel Cells: The Effects of Configurations, Electrolyte Solutions, and Electrode Materials on Power Generation, *Applied biochemistry and biotechnology* 160, 2010, pp. 168-181.
- [7] A. Larrosa-Guerrero, K. Scott, I. M. Head, F. Mateo, A. Ginesta, and C. Godinez, Effect of temperature on the performance of microbial fuel cells, *Fuel* 2010, pp.
- [8] Z. He, Y. Huang, A. K. Manohar, and F. Mansfeld, Effect of electrolyte pH on the rate of the anodic and cathodic reactions in an air-cathode microbial fuel cell, *Bioelectrochemistry* 74, 2008, pp. 78-82.
- [9] I. Ieropoulos, J. Winfield, and J. Greenman, Effects of flow-rate, inoculum and time on the internal resistance of microbial fuel cells, *Bioresource technology* 101, 2010, pp. 3520-3525.
- [10] K. Chae, M. Choi, J. Lee, K. Kim, and I. Kim, Effect of different substrates on the performance, bacterial diversity, and bacterial viability in microbial fuel cells, *Bioresource technology* 100, 2009, pp. 3518-3525.
- [11] A. Thygesen, F. W. Poulsen, B. Min, I. Angelidaki, and A. B. Thomsen, The effect of different substrates and humic acid on power generation in microbial fuel cell operation, *Bioresource technology* 100, 2009, pp. 1186-1191.
- [12] D. Pant, G. Van Bogaert, L. Diels, and K. Vanbroekhoven, A review of the substrates used in microbial fuel cells (MFCs) for sustainable energy production, *Bioresource technology* 101, 2010, pp. 1533-1543.
- [13] W. Habermann and E. Pommer, Biological fuel cells with sulphide storage capacity, *Applied microbiology and biotechnology* 35, 1991, pp. 128-133.
- [14] H. Liu, S. Cheng, and B. E. Logan, Production of electricity from acetate or butyrate using a single-chamber microbial fuel cell, *Environ. Sci. Technol* 39, 2005, pp. 658-662.
- [15] S. Chaudhuri and D. Lovley, Electricity generation by direct oxidation of glucose in mediatorless microbial fuel cells, *Nature Biotechnology* 21, 2003, pp. 1229-1232.
- [16] M. Behera and M. Ghangrekar, Performance of microbial fuel cell in response to change in sludge loading rate at different anodic feed pH, *Bioresource technology* 100, 2009, pp. 5114-5121.
- [17] L. Huang, R. J. Zeng, and I. Angelidaki, Electricity production from xylose using a mediator-less microbial fuel cell, *Bioresource technology* 99, 2008, pp. 4178-4184.
- [18] S. Venkata Mohan, G. Mohanakrishna, B. P. Reddy, R. Saravanan, and P. N. Sarma, Bioelectricity generation from chemical wastewater treatment in mediatorless (anode)

- microbial fuel cell (MFC) using selectively enriched hydrogen producing mixed culture under acidophilic microenvironment, *Biochemical Engineering Journal* 39, 2008, pp. 121-130.
- [19] X. Wang, Y. Feng, N. Ren, H. Wang, H. Lee, N. Li, and Q. Zhao, Accelerated start-up of two-chambered microbial fuel cells: Effect of anodic positive poised potential, *Electrochimica Acta* 54, 2009, pp. 1109-1114.
- [20] Y. Feng, X. Wang, B. Logan, and H. Lee, Brewery wastewater treatment using air-cathode microbial fuel cells, *Applied microbiology and biotechnology* 78, 2008, pp. 873-880.
- [21] B. Min, J. R. Kim, S. E. Oh, J. M. Regan, and B. E. Logan, Electricity generation from swine wastewater using microbial fuel cells, *Water Research* 39, 2005, pp. 4961-4968.
- [22] L. Huang and B. E. Logan, Electricity generation and treatment of paper recycling wastewater using a microbial fuel cell, *Applied microbiology and biotechnology* 80, 2008, pp. 349-355.
- [23] G. Chamberlin and G. Shute, *Colorimetric chemical analytical methods*, 1974

Bioelectricity power generation from organic substrate in a Microbial fuel cell using *Saccharomyces cerevisiae* as biocatalysts

T. Jafary¹, G.D. Najafpour^{1,*}, A.A. Ghoreyshi¹, F. Haghparast¹, M. Rahimnejad¹, H. Zare¹

¹Biotechnology Research Lab., Faculty of Chemical Engineering, Noshirvani University, Babol, Iran,

*Corresponding author Email: najafpour@nit.ac.ir

Abstract: In recent years, as a novel mode of converting organic matter into bioelectricity, Microbial fuel cells (MFCs) have gained significant attention. Among effective parameters in MFCs, substrate type and concentration play major role on MFC performance. In this study, a dual chamber MFC was used with a wide range of fructose concentrations: 10, 20, 30 and 40 g/l. The MFC was inoculated with *Saccharomyces cerevisiae* as biocatalyst. A 100 μ m of neutral red as mediator and also 100 μ m ferricyanide as oxidizer added to anode and cathode chambers, respectively. The MFC generated an open circuit voltage (OCV) of 690, 768, 548 and 507 mV with concentration of fructose from 10 to 40 g.l⁻¹, respectively. Maximum power density of 32.16, 23.7, 18.9 and 10.47 were obtained with substrate concentration of 10 to 40 g.l⁻¹, respectively. The maximum value of OCV and power density obtained with 10g.l⁻¹ of carbohydrate. To investigate resistance effect on MFC performance, for each substrate concentration data acquisition system was set at optimum value for the resistance which was resulted by the polarization curve. Then maximum power and optimum current density were recorded.

Keywords: Bioelectricity, External resistance, Fructose, Microbial fuel cell, *Saccharomyces cerevisiae*

1. Introduction

As fossil fuel sources are depleted, alternative energy sources are developed. Renewable energy is much eco-friendly such as biomass converted to fuel and energy in many alternative processes.

In the near future, the trends for new alternative renewable energies are gradually increasing.[1-4] Major efforts were devoted to develop alternative electricity generation methods.[5, 6] Among renewable alternatives, microbial fuel cell (MFC) created great interests for many researchers due to its possibility of directly harvesting electricity from organic wastes and renewable biomass.[7] MFC operates under very mild conditions and wide variable ranges of biodegradable materials are used as fuel.[8, 9] The bio base materials are oxidized by the microorganisms in the anode and the biocatalysts have the great potential to generate electrons. Biological systems possess number of advantages over the conventional chemical systems. Microbial fuel cell as the newest type of chemical fuel cells is a bioreactor that can generate electricity from what would be considered as organic wastes by means of microorganisms as biocatalysts. In this approach, bioelectricity generation and simultaneous waste treatment may take place in a cell; therefore the yield of newly developed system is much higher than any conventional processes. [10, 11]

A typical MFC consists of anodic and cathodic chambers partitioned by a proton exchange membrane (PEM). Microbes in the anodic chamber oxidize substrates and generate electrons and protons in the process. As an oxidative by-product, carbon dioxide is also produced. However, there is no net carbon emission because of the carbon dioxide originated from renewable biomass incorporated into photosynthetic process. Unlike in a direct combustion process, the electrons are absorbed by the anode and are transported to the cathode through an external circuit. After crossing a PEM or a salt bridge [12], the protons enter the cathodic chamber where they combine with oxygen to form water. Microbes in the anodic chamber generate electrons and protons in the dissimilative process of oxidizing organic substrates.[13, 14] Electric current generation is made possible by keeping microbes separated from oxygen

or any other end terminal acceptor other than the anode and this requires a separate anaerobic anodic chamber. In general, there are two types of microbial fuel cells: mediator and mediator-less microbial fuel cells.[15-18]

Among effective parameters on performance of microbial fuel cell, substrate type and concentrations had a significant effect on cell power.[19-22] The aim of this study was to investigate the effect of fructose, a monosaccharide that could be found in many fruit juices. Substrate concentrations were varied from 10 to 40 g.l⁻¹. Also, the influence of external resistance on production of bioelectricity in a dual chamber MFC was evaluated.

2. Methodology

Saccharomyces cerevisiae PTCC 5269 was supplied by Iranian Research Organization for Science and Technology (IROST), Tehran, Iran. The microorganisms were grown in an anaerobic jar. The prepared medium for seed culture consists of yeast extract, NH₄Cl, NaH₂PO₄, MgSO₄ and MnSO₄: 3, 0.2, 0.6, 0.2 and 0.05 g.l⁻¹, respectively. Fructose as carbon source was added to the medium with concentration in the range of 10-40 g.l⁻¹. The medium was sterilized, autoclaved at 121°C and 15psig for 20 min.

The medium pH was initially adjusted to 6.5 and the inoculums were introduced into the media at ambient temperature. The inoculated cultures were incubated at 30°C. The bacteria were fully grown for duration of 24 hours in 100 ml flask without any agitation. Substrate consumption was calculated based on determination of reduced sugars in the culture broth. All chemicals and reagents used for the experiments were analytical grades and supplied by Merck (Darmstadt, Germany). The pH meter, HANA 211(Romania) model glass-electrode was employed for pH measurements of the samples in aqueous phase. The initial pH of the working solutions was adjusted by addition of dilute HNO₃ or 0.1M NaOH solutions. DNS reagent was employed to detect and measure substrate consumption using colorimetric method and cell growth was also monitored by optical density using spectrophotometer (Unico, USA) at wave length of 620nm.

The fabricated cells in laboratory scale were made of Plexiglas material. The volume of each chamber (anode and cathode chambers) was 800 ml with working volume of 600 ml (75% of total volume). The sample port was provided for anode chamber, wire point inputs and inlet port. The selected electrodes in MFC were graphite felt in size of 50×35×2 mm. Proton exchange membrane (PEM; NAFION 112, Sigma–Aldrich) was used to separate two compartments. The Nafion area separated the chambers was 3.79 cm². Nafion as a proton exchange membrane was subjected to a course of pretreatment to take off any impurities. The membrane pretreatment started with boiling the film in 3% H₂O₂ for 1h, washed with deionized water, 0.5 M H₂SO₄, and then washed with deionized water. The anode and cathode compartments were filled by deionized water when the biological fuel cell was not in use to maintain and preserve the membrane for good conductivity. Natural Red and Ferricyanide were supplied by Merck (Germany). These chemicals with the concentrations of 100 μmol.l⁻¹ & 100 μmol.l⁻¹ were used as mediators in anode and cathode of MFC, respectively.

In the microbial fuel cell, *S. cerevisiae* was used as a biocatalyst for production of bioelectricity from carbohydrate source. This microorganism was grown under anaerobic condition in the biofuel cell. Fixed incubation time and enriched medium was used. The obtained data showed that *S. cerevisiae* had good ability to consume substrate under anaerobic

condition. The Fabricated cell for the experimental set up with auxiliary equipments is shown in Fig. 1.

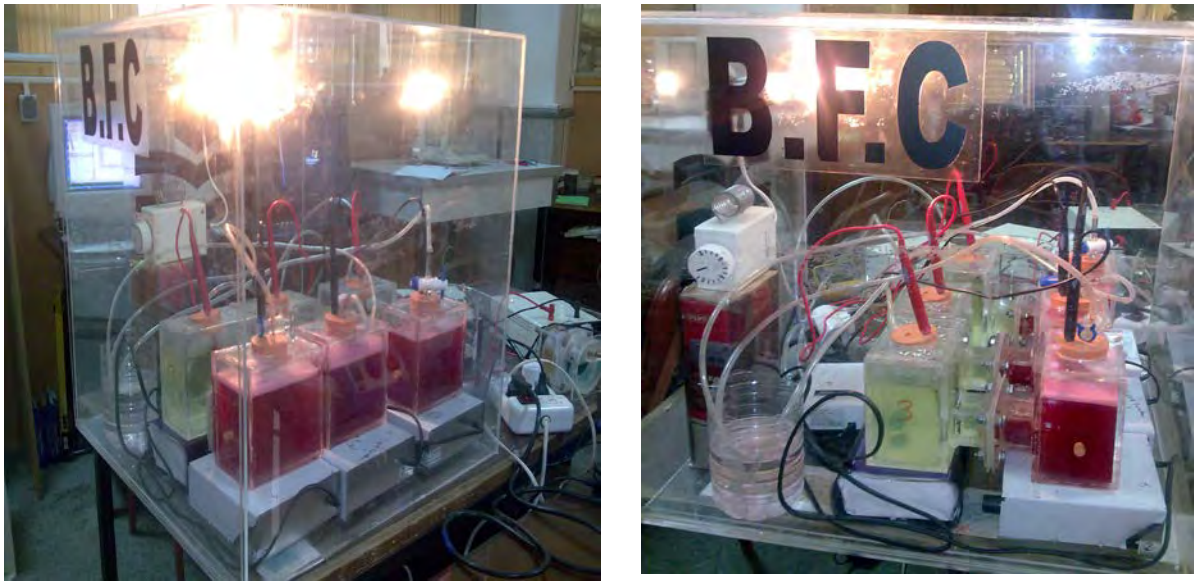


Fig. 1. The laboratory-scale MFCs with thermal controller in enclosed space

3. Result and Discussion

To start up the process, *S. cerevisiae* was inoculated into anode chamber. Fructose fed to microbial fuel cell with concentrations ranged from 10 to 40 g.l⁻¹. The output result in the form of open circuit voltage (OCV) was recorded by the data acquisition system. Biochemical activity of the microorganisms gradually increased electricity generation. At incubation time 64, 68, 59 and 57 hours after inoculation, the output OCV remained constant while the cell growth proceeded to stationary phase. The recorded voltages were 690, 768, 548 and 507 mV for 10, 20, 30 and 40 g.l⁻¹ of fructose, respectively. Due to stability of process operation after incubation time, the polarization curves were also recorded by data acquisition system in order to evaluate the performance of the MFCs. Fig. 2 shows the substrate concentration was increased (10 to 40 g.l⁻¹) the power and current density were decreased. With substrate concentration of 10 g.l⁻¹, maximum power and current density generated were 32.16 mW.m⁻² and 96.59 mA.m⁻², respectively.

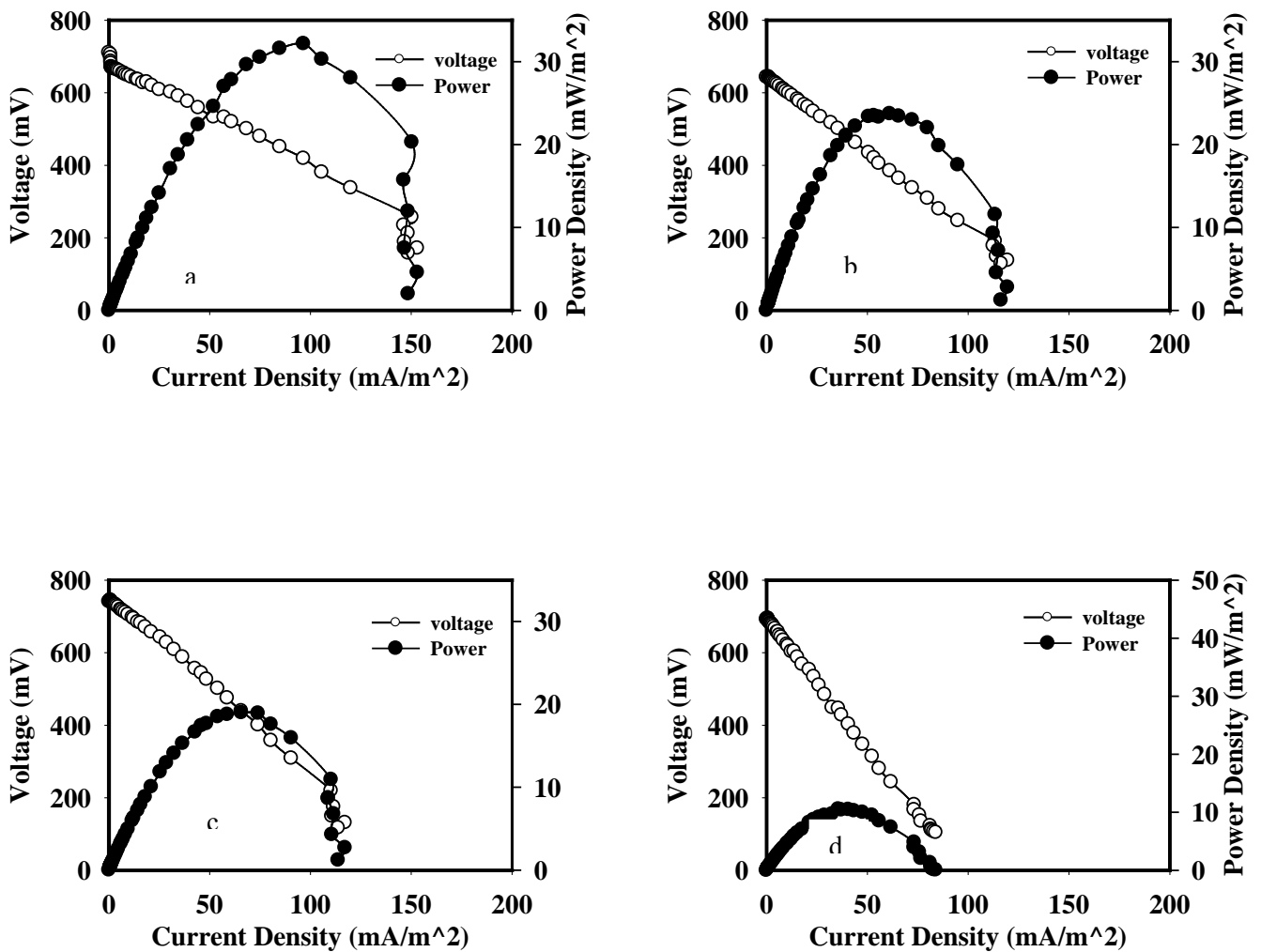


Fig. 2. Effect of different concentrations of fructose on polarization curves
a) 10 g.l⁻¹, b) 20 g.l⁻¹, c) 30 g.l⁻¹, d) 40 g.l⁻¹

As the electrical resistance applied to plot polarization curve varied in the range of 65535 to 0.1 k Ω , the pick point of the graph occurred at 3.88k Ω . Pick point demonstrated maximum power density and the optimum current density were proportional to applied resistance. The MFC performance is illustrated in Fig. 3. The cathode and anode of MFC were connected together through a circuit of 3.88k Ω as an external resistance. Due to presence of resistance, the power and voltage were considered as operational electricity (see Fig. 3).

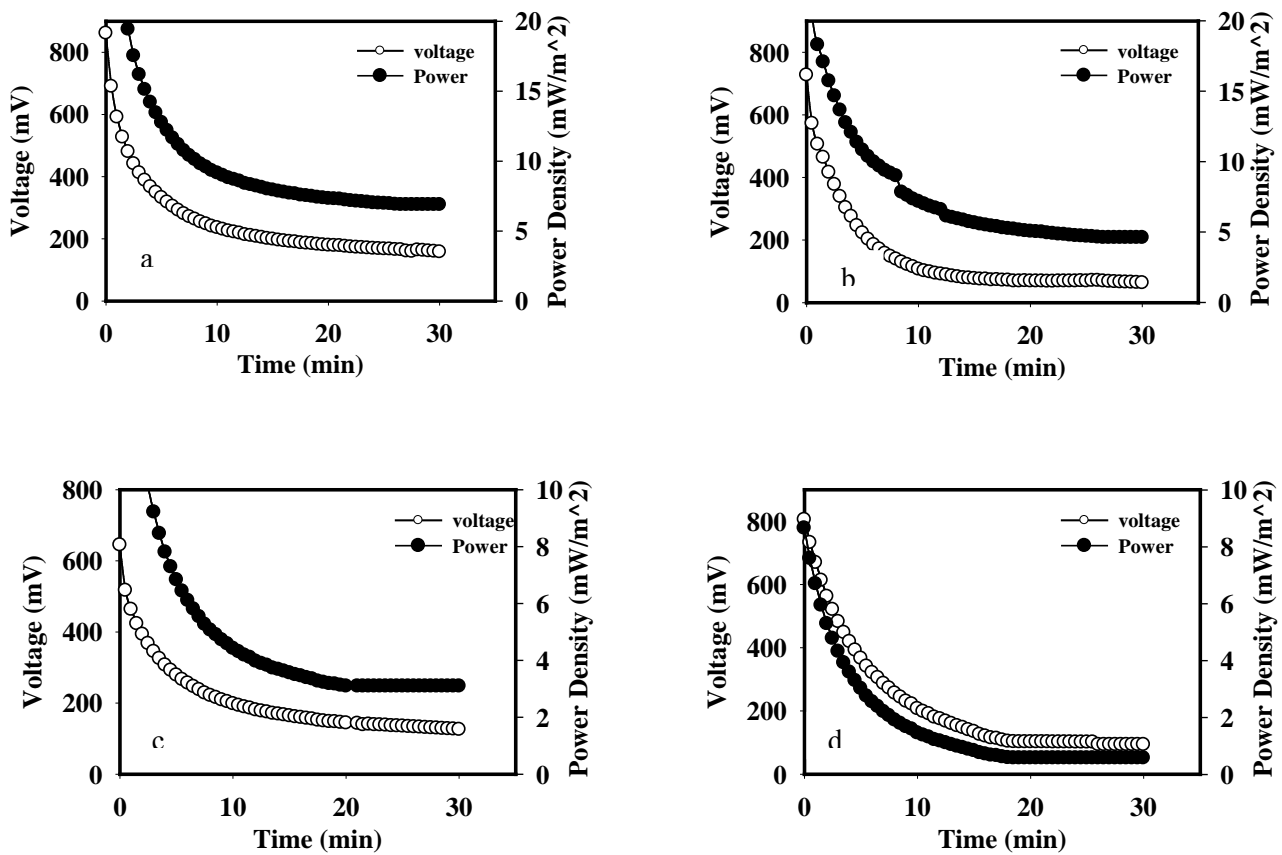


Fig. 3. Effect of external resistance on power density and voltage of MFC fed with
a) 10 g.l⁻¹, b) 20 g.l⁻¹, c) 30 g.l⁻¹ and d) 40 g.l⁻¹ of fructose solution

The performance of MFC with respect to time was monitored. The voltage and power density in experimental runs for the course 30 minutes were obtained. In addition, current density was also recorded but due to complexity of presented plots the data are not shown. However the recorded data were averaged and summarized in Table 1.

Table 1. Mean power and current density and mean voltage in presence of 3.88 kΩ as an external resistance

Fructose Concentration g.l ⁻¹	Mean Power Density mW/m ⁻²	Mean Current Density mA/m ⁻²	Mean Voltage mV
10	11.26	56.25	196.02
20	9.8	39.17	248.2
30	5.86	36.88	165.7
40	2.3	15.86	145.9

4. Conclusions

The effect of substrate concentrations was investigated in a dual microbial fuel cell. Fructose was chosen as the simple carbon source with concentrations ranged from 1 to 40 g.l⁻¹. *S. cerevisiae* as the biocatalyst successfully oxidized the soluble substrate. The biocatalysts in the media with concentration of 10 g.l⁻¹ of substrate demonstrated the maximum power and optimum current density of 32.16 mW/m⁻² and 96.59 mA/m⁻², respectively. The proportional resistance to the pick point of the polarization curve at 3.88 kΩ, was applied to the circuit as an external resistance in the operating system. The obtained averaged power and current density were 11.26 mW/m⁻² and 56.26 mA/m⁻², respectively. The presented data were allocated to fructose with total sugar concentration of 10 g.l⁻¹.

References

- [1] S. Meher Kotay and D. Das, Biohydrogen as a renewable energy resource--Prospects and potentials, *International Journal of Hydrogen Energy* 33, 2008, pp. 258-263.
- [2] M. Dresselhaus and I. Thomas, Alternative energy technologies, *Nature* 414, 2001, pp. 332-337.
- [3] R. Navarro, M. Sánchez-Sánchez, M. Alvarez-Galvan, F. Valle, and J. Fierro, Hydrogen production from renewable sources: biomass and photocatalytic opportunities, *Energy & Environmental Science* 2, 2009, pp. 35-54.
- [4] M. Parikka, Global biomass fuel resources, *Biomass and Bioenergy* 27, 2004, pp. 613 - 620.
- [5] A. Boudghene Stambouli and E. Traversa, Fuel cells, an alternative to standard sources of energy, *Renewable and Sustainable Energy Reviews* 6, 2002, pp. 295-304.
- [6] B. Logan, Peer Reviewed: Extracting Hydrogen and Electricity from Renewable Resources, *Environmental science & technology* 38, 2004, pp. 160-167.
- [7] D. Lovley, Microbial fuel cells: novel microbial physiologies and engineering approaches, *Current opinion in biotechnology* 17, 2006, pp. 327-332.
- [8] M. Grzebyk and G. Pozniak, Microbial fuel cells (MFCs) with interpolymer cation exchange membranes, *Separation and Purification Technology* 41, 2005, pp. 321-328.
- [9] F. Zhao, F. Harnisch, U. Schröder, F. Scholz, P. Bogdanoff, and I. Herrmann, Application of pyrolysed iron (II) phthalocyanine and CoTMPP based oxygen reduction catalysts as cathode materials in microbial fuel cells, *Electrochemistry Communications* 7, 2005, pp. 1405-1410.
- [10] S. Patil, V. Surakasi, S. Koul, S. Ijmulwar, A. Vivek, Y. Shouche, and B. Kapadnis, Electricity generation using chocolate industry wastewater and its treatment in activated sludge based microbial fuel cell and analysis of developed microbial community in the anode chamber, *Bioresource technology* 100, 2009, pp. 5132-5139.
- [11] H. Liu, R. Ramnarayanan, and B. Logan, Production of electricity during wastewater treatment using a single chamber microbial fuel cell, *Environ. Sci. Technol* 38, 2004, pp. 2281-2285.
- [12] B. Min, S. Cheng, and B. Logan, Electricity generation using membrane and salt bridge microbial fuel cells, *Water research* 39, 2005, pp. 1675-1686.
- [13] J. Jang, Construction and operation of a novel mediator-and membrane-less microbial fuel cell, *Process Biochemistry* 39, 2004, pp. 1007-1012.

- [14] B. Logan and J. Regan, Electricity-producing bacterial communities in microbial fuel cells, *TRENDS in Microbiology* 14, 2006, pp. 512-518.
- [15] H. Kim, H. Park, M. Hyun, I. Chang, M. Kim, and B. Kim, A mediator-less microbial fuel cell using a metal reducing bacterium, *Shewanella putrefaciens*, *Enzyme and Microbial technology* 30, 2002, pp. 145-152.
- [16] G. Gil, I. Chang, B. Kim, M. Kim, J. Jang, H. Park, and H. Kim, Operational parameters affecting the performance of a mediator-less microbial fuel cell, *Biosensors and Bioelectronics* 18, 2003, pp. 327-334.
- [17] D. Park and J. Zeikus, Electricity generation in microbial fuel cells using neutral red as an electronophore, *Applied and environmental microbiology* 66, 2000, pp. 1292.
- [18] M. Nielsen, D. Wu, P. Girguis, and C. Reimers, Influence of Substrate on Electron Transfer Mechanisms in Chambered Benthic Microbial Fuel Cells, *Environmental science & technology* 43, 2009, pp. 8671-8677.
- [19] D. Pant, G. Van Bogaert, L. Diels, and K. Vanbroekhoven, A review of the substrates used in microbial fuel cells (MFCs) for sustainable energy production, *Bioresource technology* 101, pp. 1533-1543.
- [20] J. Niessen, U. Schröder, and F. Scholz, Exploiting complex carbohydrates for microbial electricity generation—a bacterial fuel cell operating on starch, *Electrochemistry Communications* 6, 2004, pp. 955-958.
- [21] M. Reddy, S. Srikanth, S. Mohan, and P. Sarma, Phosphatase and dehydrogenase activities in anodic chamber of single chamber microbial fuel cell (MFC) at variable substrate loading conditions, *Bioelectrochemistry* 77, pp. 125-132.
- [22] Y. Zhang, B. Min, L. Huang, and I. Angelidaki, Electricity generation and microbial community response to substrate changes in microbial fuel cell, *Bioresource technology* 201.

Performance and economics of low cost clay cylinder microbial fuel cell for wastewater treatment

Siva Rama Satyam B¹, Manaswini Behera¹, Makarand M. Ghangrekar^{1,*}

¹ Department of Civil Engineering, Indian Institute of Technology, Kharagpur – 721302, India

*Corresponding Author. Tel.: +91-3222-283440; Fax: +91-3222-282254

E-mail: ghangrekar@civil.iitkgp.ernet.in

Abstract: Current wastewater treatment processes require large amount of power for various treatment units and most of the useful energy available in the wastewater remains unrecovered. With increase in demand for clean treatment technologies, Microbial Fuel Cell (MFC) technology is a viable option for treatment of wastewater, since simultaneous recovery of energy in the form of direct electricity with desired degree of treatment can be achieved in this process. Extensive research on MFCs is going on at laboratory scale but very few pilot scale studies have been reported. An attempt has been made to produce low cost scaled up MFCs fabricated using naturally available cheaper clay material as proton exchange membrane without involving any costly polymer membrane or noble metals for electrode fabrication. The results of the experimental study are promising and encouraging for further scaling up of MFCs.

Economic feasibility of MFCs for treating municipal wastewater having COD of 500 mg ·L⁻¹ has been studied. The cost analysis shows that clay material may be suitable option as a membrane in scaling up of MFCs. It needs further study on strength of clay material as membrane to handle higher wastewater flows in larger reactor volume. Although, these clay MFCs were operated for more than six months, the life of this material without deteriorating its functional utility also need attention.

Keywords: Earthen cylinder MFC, Proton exchange membrane, Power density

1. Introduction

The global energy demand is increasing with exponential growth of population. Unsustainable supply of fossil fuels and the environmental concerns like air pollution and global warming associated with the use of fossil fuels are acting as major impetus for research into alternative renewable energy technologies. The high energy requirement of conventional sewage treatment systems are demanding for the alternative treatment technology which will require less energy for its efficient operation and recover useful energy to make this operation sustainable. In past two decades, high rate anaerobic processes such as up-flow anaerobic sludge blanket (UASB) reactors are finding increasing application for the treatment of domestic as well as industrial wastewaters. Although, energy can be recovered in the form of methane gas during anaerobic treatment of the wastewater, but utilization of methane for electricity generation is not attractive while treating small quantity of low strength wastewater and usually it is flared [1]. Therefore, other alternatives for simultaneous wastewater treatment with clean energy production are much desired.

Microbial fuel cell (MFC) is a promising technology for simultaneous treatment of organic wastewater and bio energy recovery in the form of direct electricity, which has gained much interest in recent years. Conventionally, MFC is made up of an anode chamber and a cathode chamber separated by a proton exchange membrane (PEM). MFCs are devices that use bacteria as the catalysts to oxidize organic matter and generate current. Electrons produced by the bacteria from the substrates i.e., organic matter present in wastewater in this case, are transferred to the anode. The electrons are transported to the cathode through an external circuit and protons are transferred through the membrane internally, where they utilize either oxygen to form water or other chemical oxidants to form reduced product.

The PEM used in MFC plays a substantial role in the power generation [2]. Despite of the rapid development of separators in recent years, there are limitations such as proton transfer limitation and oxygen leakage, which increase the internal resistance and decrease the MFC performance, and thus limit the practical application of MFCs [3]. Various materials are used by the researchers for separating anode and cathode chambers, including cation exchange membrane, anion exchange membrane, ultrafiltration membranes [4], bipolar membrane [5], microfiltration membrane [6], J-Cloth [7] and salt bridge [8], etc. The advances in separator materials and configurations have opened up new promises to overcome these limitations, but challenges remain for the practical full scale application of MFC for wastewater treatment using this material because of its high production cost and fouling of membrane expected requiring replacement. Recently successful treatment of synthetic and rice mill wastewater has been reported in MFC fabricated using earthen pot acting as membrane and its performance has been compared with MFC fabricated using Nafion membrane [9,10]. In terms of organic matter removal and power production it is reported that the earthen pot membrane MFC demonstrated better performance than the Nafion membrane MFC. Better performance of earthen cylinder MFC has been reported without employing commercially available PEM than that of MFC using Nafion as PEM [11]. Utilization of such low cost separator will drastically reduce production cost of MFC and it will help in enhancing its application for small wastewater treatment system.

Extensive research on MFCs is going on at laboratory scale but very few pilot scale studies have been reported. To bring this novel technology from laboratory to pilot scale, an attempt has been made for volumetric comparison of the performance of low cost mediator-less MFCs fabricated using naturally available cheaper clay material as proton exchange membrane instead of costly membrane and without using any catalysts. Economic feasibility of MFCs for treating municipal wastewater having COD of $500 \text{ mg} \cdot \text{L}^{-1}$ has been studied.

2. Methodology

2.1. Experimental set-up

The study was carried out in two laboratory scale up-flow dual chamber MFCs (MFC-1, MFC-2) with outer cathode chamber and inner cylindrical anode chamber without employing commercially available PEM. The anode chamber in both the MFCs was made up of earthen cylinder and the wall (5 mm thick) of the earthen cylinder itself was used as the medium for proton exchange. The working volume of anode chamber of MFC-1 and MFC-2 was 0.6 L and 3.75 L, respectively. The cathode chamber volume was 4.5 L and 16 L in MFC-1 and MFC-2, respectively. Earthen cylinder, made from locally available soil (elements present: Na-1.15 %, Mg- 1.52 %, Al-20.50 %, Si-53.52 %, K-4.74 %, Ca-1.15 %, Ti-0.94 %, Fe-16.48 %), was used in this study. The MFCs were operated under continuous mode. The wastewater was supplied to the MFCs from the bottom of the anode chamber with the help of peristaltic pump. The effluent leaving the anode chamber at the top was brought to the cathode chamber to work as catholyte, where it was given further aerobic treatment with the help of aerators. Stainless steel mesh having total surface area of 360 cm^2 and 2250 cm^2 was used as anode electrodes and graphite plates, having total surface area of 250 cm^2 and 1562.5 cm^2 , was used as cathode electrodes in MFC-1 and MFC-2, respectively. The electrodes were connected externally with concealed copper wire through external resistance of 100Ω .

2.2. MFC Operation

Synthetic wastewater containing sucrose as a source of carbon having chemical oxygen demand (COD) of about $500 \text{ mg} \cdot \text{L}^{-1}$ was used in this study. The sucrose medium was prepared using the composition given by Jadhav and Ghangrekar [12]. During start up, MFCs

were inoculated with anaerobic sludge collected from septic tank bottom after giving heat pretreatment [13] and required amount of sludge was added to the reactors to maintain the sludge loading rate at $0.1 \text{ kg COD} \cdot \text{kg VSS}^{-1} \cdot \text{d}^{-1}$. The influent feed pH was in the range of 7.2 to 7.8 throughout the experiments. These MFCs were operated at room temperature varying from 26 to 34°C. Both the MFCs were operated under continuous mode at hydraulic retention time (HRT) of 13 h and organic loading rate (OLR) of $0.923 \text{ kg COD} \cdot \text{m}^{-3} \cdot \text{d}^{-1}$.

2.3. Analyses and calculations

The suspended solids (SS), volatile suspended solids (VSS), and COD were monitored according to APHA standard methods [14]. The elemental composition of the earthen cylinder material was determined by Energy Dispersive X-ray analysis (EDX) scanning electron microscope with oxford EDX detector (JEOL JSM5800, Japan). The voltage and current were measured using a digital multimeter with data acquisition unit (Agilent Technologies, Malaysia) and converted to power according to $P = I \cdot V$; where, P = power, I = current, and V = voltage (V). The Coulombic efficiency (CE) was estimated by integrating the measured current relative to the theoretical current on the basis of consumed COD [15]. Polarization studies were carried out at variable external resistances (10000-10 Ω) using 10 K Ω variable resistors. Internal resistance of the MFCs was measured from the slope of line from the plot of voltage versus current [16].

3. Results

3.1. Substrate degradation

The synthetic wastewater having COD of about $500 \text{ mg} \cdot \text{L}^{-1}$ was treated anaerobically first in the anode chamber of the MFCs and further aerobic treatment was given to the anode chamber effluent in the cathode chamber. To achieve stable performance in terms COD removal efficiency MFC-1 took about 15 days and MFC-2 took about 13 days. Average COD removal efficiencies in the anode chambers of MFC-1 and MFC-2 were $77.5 \pm 3.1\%$ and $86.9 \pm 2.65\%$, respectively. After aerobic treatment in the cathode chamber the total COD removal efficiencies of both MFC-1 and MFC-2 were $90.7 \pm 4.2\%$ and $93.12 \pm 2.6\%$, respectively. The larger volume MFC (MFC-2) demonstrated higher COD removal efficiency when both the MFCs were operated at similar HRT and OLR. The higher COD removal could be due to better retention of sludge in larger reactor as compared to smaller reactor improving solid retention time, which favors higher substrate degradation rates.

3.2. Power generation

Electricity generation in both the MFCs increased gradually with time and got stabilized. Maximum open circuit voltage (OCV) of 0.698 V and maximum short circuit current (SC) of 6.04 mA were observed in MFC-1. Maximum OCV of 0.776 V and maximum SC of 27.6 mA were obtained in MFC-2. The average electrical output from these MFCs is presented in the Table 1. Sustainable power density (normalized to the anode surface area) of $12.84 \text{ mW} \cdot \text{m}^{-2}$ and volumetric power (normalized to the working volume of anode chamber) of $770 \text{ mW} \cdot \text{m}^{-3}$ (2.15 mA, 0.215 V) were generated at 100 Ω external resistance in MFC-1. MFC-2 generated sustainable power density and volumetric power of $12.11 \text{ mW} \cdot \text{m}^{-2}$ and $727 \text{ mW} \cdot \text{m}^{-3}$, respectively. Sustainable volumetric current density with respect to working volume of anode chamber achieved in MFC-1 and MFC-2 were $3.6 \text{ A} \cdot \text{m}^{-3}$ and $1.4 \text{ A} \cdot \text{m}^{-3}$, respectively. Maximum Coulombic efficiency of 5.43 % and 4.49 % was achieved in MFC-1 and MFC-2, respectively.

Table 1. Power generation in the MFCs at OLR of 0.923 kg COD · m⁻³ · d⁻¹

MFC	OCV (V)	SC (mA)	Voltage across 100 Ω (V)	Current density with 100 Ω (A · m ⁻³)	Power density with 100 Ω (mW · m ⁻²)	Power/vol .with 100 Ω (mW · m ⁻³)	Max. Power/ vol. at optimum resistance (W · m ⁻³)	Internal resistance (Ω)
MFC-1	0.692	4.9	0.215	3.6	12.84	770.4	0.96	212.0
MFC-2	0.767	21.9	0.522	1.4	12.11	726.9	1.00	44.3

Although, the larger volume MFC (MFC-2) demonstrated slightly lower CE (4.49 %) as compared to MFC-1 (CE of 5.43 %), the volumetric power produced in both these MFCs was similar. This was due to 143 % higher working voltage demonstrated by MFC-2. This higher working voltage observed in MFC-2 could be due to higher working volume and hence having higher surface area of electrodes improving capacitance of the system. Also, the higher cathode surface area might have favored better cathodic reaction by reducing cathodic overpotential and improving voltage produced by this MFC as compared to MFC-1 with lower cathode surface area. Since oxygen is terminal electron acceptor in cathode, reduction of oxygen on cathode surface can occur in two different mechanisms at 25°C as:



Cathode potentials in MFC-1 and MFC-2 were 210 mV and 330 mV without employing any noble catalysts. The typical measured cathode potentials using oxygen as terminal electron acceptor is around 200 mV [15]. The higher cathode potential observed demonstrates the better performance of graphite plate cathode while using earthen material as membrane.

3.3. Polarization and internal resistance

Polarization studies were carried out for the MFCs by varying external resistance from 10000 Ω to 10 Ω. Maximum power densities observed during polarization were 15.97 mW · m⁻² at external resistance of 234 Ω in MFC-1 and 16.74 mW · m⁻² at external resistance of 45.5 Ω in MFC-2 (Fig. 1). Internal resistance of the MFCs measured from the slope of line from the voltage versus current plot of MFC-1 and MFC-2 were 212 Ω and 44.3 Ω, respectively. In spite of 6.25 times larger surface area of anode provided in MFC-2, it demonstrated slightly higher power density than the MFC-1 provided with lower anode surface area. Also, the larger MFC demonstrated very low internal resistance as compared to smaller MFC, indicating better substrate diffusion and less internal losses in larger MFC. This is particularly encouraging for scaling up of MFC and provides a scope for further increase in anode volume and surface area to obtain similar power density. This experience has demonstrated that, if properly designed, similar energy recovery efficiency can be obtained from the larger MFCs. This will facilitate reducing number of MFCs, to treat same wastewater volume or produce desired power, thus reducing its production cost and also operating complications and cost.

3.4. Cost Analysis for MFC

Preliminary cost analysis for MFCs treating municipal wastewater having COD of 500 mg · L⁻¹ with anode chamber volume of 20 liters and hydraulic retention time of 10 hours was performed. For 1 m³ of wastewater treatment per day number of MFCs required are 21 and each will be treating wastewater flow rate of 48 L · d⁻¹. With assumed COD removal efficiency of 75 %, cell voltage of 0.5 V and CE of 30 %, the power obtained from each cell is 0.3 W.

Reversal of voltage in stack of cells is not considered and maintenance cost of the cells and pumping costs are not included in the cost comparison. For treating wastewater flow of $1000 \text{ m}^3 \cdot \text{d}^{-1}$, total power achieved from MFC plant is 7.9 KW. Maximum power available in this wastewater is calculated based on $1 \text{ g COD} = 14.7 \text{ kJ}$ [17]. Fig. 2 presents the power likely to be harvested from the MFCs treating $1000 \text{ m}^3 \cdot \text{d}^{-1}$ of wastewater flow rate at different Coulombic efficiencies. There is lot of scope for MFC to improve because from the theoretical calculations of power production at different flow rates with assumed voltage of 0.5 V , maximum power achieved from MFCs is 23.6 kW at CE of 90% and at flow rate of $1000 \text{ m}^3 \cdot \text{d}^{-1}$. Maximum power available in wastewater at similar conditions is 63.8 kW .

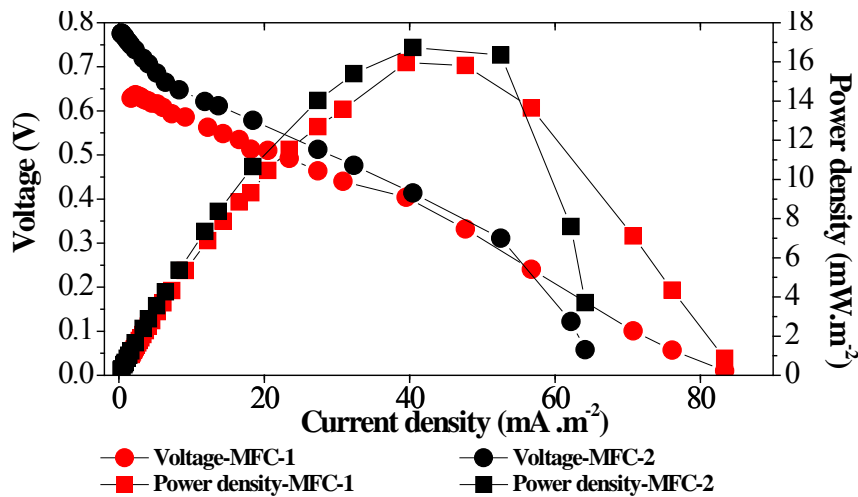


Fig. 1. Polarization curves for MFC-1 and MFC-2

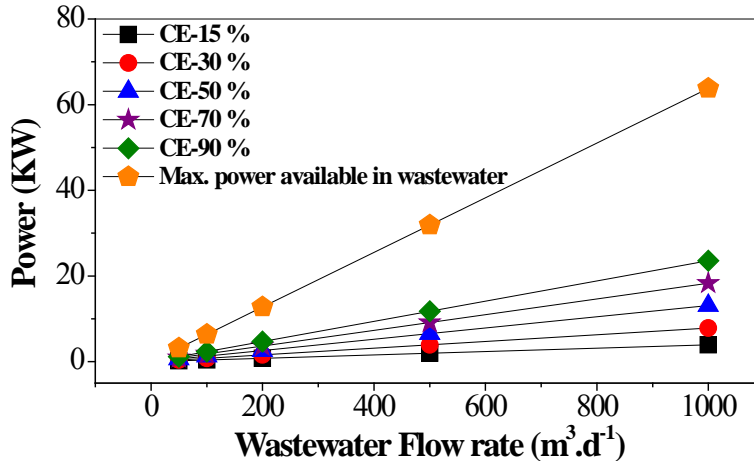


Figure 2 : Power achieved from the MFC treatment plant at different CE and different wastewater flowrates with assumed voltage obtained from each cell of 0.5 V and COD removal efficiency of 75% .

The materials considered for cell construction are Stainless Steel (SS) mesh as electrode for both anode and cathode, Sintex^R pipe for anode and cathode chamber in case of nafion membrane where 12 slits of $8 \text{ cm} \times 10 \text{ cm}$ were considered on the circumference of anode chamber wall for nafion membrane insertion (6 in bottom half and 6 in top half of anode chamber). In the second case, hollow cylindrical earthen pot was considered for fabrication of anode and the pot material acting as a membrane separating anode and cathode and Sintex^R pipe was considered for fabrication of cathode chamber. Cost of each of these materials considered in this study is according to the prevailing Indian market. The approximate costing

of the MFCs for treatment of different wastewater flows is presented in the Table 2. MFC with earthen material as membrane is a sustainable option for its application in wastewater treatment because of low cost (79 % cost reduction compared to Nafion as membrane) and comparable power generation and treatment efficiency in terms of COD removal than Nafion as membrane. In addition to this no chemical mediators are considered in this study to enhance the power production.

Table 2. Total capital cost comparison of MFC plant at different flow rates of waste water

Flow of wastewater (m ³ · d ⁻¹)	Cost of MFC cells with Nafion membrane (Rupees)	Cost of MFC cells with earthen pot as membrane (Rupees)	% of cost reduction with earthen material than Nafion
1000	159,106,828	32,750,000	79
500	79,553,414	16,375,000	79
200	31,821,366	6,550,000	79
100	15,910,683	3,275,000	79
50	7,955,341	1,637,500	79

4. Discussions

The overall COD removal efficiency of both the MFCs were more than 90%, which demonstrates the feasibility of this configuration of MFC as an effective wastewater treatment technology and ensures better reliable effluent quality. It was observed that the power generation in the MFC did not change significantly when the volume of the reactor was increased from 0.6 L to 3.75 L. This result demonstrates that there is further scope in increasing the reactor size.

Jana et al. [11] have reported sustainable power density of 48.30 m W · m⁻² in an MFC employing earthen cylinder of 0.6 L capacity as anode chamber. The power generated in MFC-1 was lower than that obtained by Jana et al. [11]. MFC-1 was in operation over 6 months prior to present study. The reduction in power generation might be due to fouling of earthen cylinder used as separator and decrease in the porosity of the earthen material, which probably has reduced the proton transfer and also due to the reuse of old graphite plate's electrodes. Recently we observed that by polishing the surfaces of graphite plates increased the power generation.

The internal resistance and overpotential losses of MFC-2 are less than MFC-1 which motivates further scaling up of microbial fuel cells with earthen cylinder as PEM. The study was carried out with synthetic wastewater. It needs further study on strength of clay material as membrane for higher wastewater flows and higher reactor volumes. The life of this material without deteriorating its functional utility also needs attention.

Rozendal et al. [18] have compared the anticipated costs of MFCs with the capital costs of the two most widely used conventional wastewater treatment systems, i.e., activated sludge treatment and anaerobic digestion. This comparison shows that, based on the materials currently used in the laboratory, the capital costs of a full scale bioelectrochemical systems would be orders of magnitude higher than those of conventional wastewater treatment systems. The capital cost might be reduced significantly by improving the design and employing innovative materials, but because of the inherently complex design of bioelectrochemical systems, it is expected that the capital cost will always remain several times that of conventional wastewater treatment systems. However, for smaller wastewater flow such as from individual house or from the small group of housing, the cost of MFC may

become comparable with the other treatment methods and the advantage of direct electricity generation for powering certain onsite appliances can be gained. Also, this process can be best utilized for treatment of wastewater in remote area and generating the power in the form of direct electricity. Thus, the advantage of making electricity available can be utilized along with wastewater treatment in the remote area which is not connected with the electric grid.

The major drawback in MFC as compared to other processes is smaller volume required for anode chamber. Whatsoever the volume of anode, it will deliver maximum voltage of about 0.7 V and hence, smaller anode volume is desirable for integrating voltage by putting several MFCs in series. Whereas the single large anode of volume equal to that of summation of anode volumes in series will produce only about 0.7 V. Hence, while scaling up a trade-off need to be maintained while finalizing anode volume between the voltage and current recovered. If larger volume MFCs is able to demonstrate similar CE as smaller MFCs, higher current can be recovered from the MFC to maintain similar volumetric power densities. Therefore while scaling the geometrical arrangement and relative positions of the electrodes should be decided in such a way to obtain maximum Coulombic efficiency. Such large size MFCs will then be able to compete with the established alternative wastewater treatment processes in terms of capital investments.

5. Conclusions

Clay material was found to be a cheaper alternative to more commonly used expensive Nafion membrane in MFCs. It needs further study on strength of clay material as membrane for higher wastewater flows and higher reactor volumes. Although, these clay MFCs were operated for more than six months, the life of this material without deteriorating its functional utility also need attention. It remains to be demonstrated whether the results from this liter scale MFC can be extrapolated to more realistic scales for industrial applications. Full scale implementation of bioelectrochemical system is not straightforward as it includes certain microbiological, technological and economic challenges, which need to be resolved that have not previously been encountered in any other wastewater treatment systems.

Acknowledgement

The Grant received from the Ministry of Environment and Forest, Government of India (F. No. 19-35/2005-RE) is duly acknowledged.

References

- [1] M.M. Ghangrekar, V.B. Shinde, Wastewater treatment in microbial fuel cell and electricity generation: a sustainable approach. Proceedings of 12th international sustainable development research conference, 2006, Hong Kong, pp. 1-9.
- [2] Z. Du, H. Li, T. Gu, A state of the art review on microbial fuel cells: A promising technology for wastewater treatment and bioenergy, *Biotechnology Advances*, 25, 2007, pp. 464-482.
- [3] W.W. Li, G.P. Sheng, X.W. Liu, H.Q. Yu, Recent advances in the separators for microbial fuel cells, *Bioresource Technology*, 102, 2011, pp. 244–252.
- [4] J.R. Kim, S. Cheng, S.E. Oh, B.E. Logan, Power generation using different cation, anion, and ultrafiltration membranes in microbial fuel cells, *Environmental Science and Technology*, 41, 2007, pp. 1004-1009.

- [5] A. Terheijne, H.V.M. Hamelers, V.D. Wildie, R.A. Rozendal, C.J.N. Buisman, A bipolar membrane combined with ferric iron reduction as an efficient cathode system in microbial fuel cells, *Environmental Science and Technology*, 40, 2006, pp. 5200-5206.
- [6] J. Sun, Y. Hu, Z. Bi, Y. Cao, Simultaneous decolorization of azo dye and bioelectricity generation using a microfiltration membrane air-cathode single-chamber microbial fuel cell, *Bioresource Technology*, 100, 2009, pp. 3185–3192.
- [7] Y. Fan, H. Hu, H. Liu, Enhanced Coulombic efficiency and power density of air-cathode microbial fuel cells with an improved cell configuration, *Journal of Power Sources*, 171, 2007, pp. 348–354.
- [8] B. Min, S. Cheng, B.E. Logan, Electricity generation using membrane and salt bridge microbial fuel cells, *Water Research* 39, 2005, pp.1675-1686.
- [9] M. Behera, P. S. Jana, M.M. Ghangrekar, Performance evaluation of low cost microbial fuel cell fabricated using earthen pot with biotic and abiotic cathode, *Bioresource Technology*, 101, 2010, pp.1183-1189.
- [10] M. Behera, P. S. Jana, T. T., More, M.M. Ghangrekar, Rice mill wastewater treatment in microbial fuel cells fabricated using proton exchange membrane and earthen pot at different pH, *Bioelectrochemistry*, 79, 2010, pp. 228-233.
- [11] P. S. Jana, M. Behera, M.M. Ghangrekar, Performance comparison of up-flow microbial fuel cells fabricated using proton exchange membrane and earthen cylinder, *International Journal of Hydrogen Energy*, 35, 2010, pp. 5681-5686.
- [12] G.S. Jadhav, M.M. Ghangrekar, Improving performance of MFC by design alteration and adding cathodic electrolytes, *Applied Biochemistry and Biotechnology*, 2008, 151, pp. 319-332.
- [13] M.M. Ghangrekar, V.B. Shinde, Performance of membrane-less microbial fuel cell treating wastewater and effect of electrode distance and area on electricity production, *Bioresource Technology*, 98, 2007, pp. 2879-2885.
- [14] APHA, AWWA, WPCF, Standard methods for examination of water and wastewater, Washington, D.C., 20th Ed., 1998.
- [15] B.E. Logan, B. Hamelers, R. Rozendal, U. Schroder, J. Keller, S. Freguia, P. Aelterman, W. Verstraete, K. Rabaey, Microbial fuel cells: methodology and technology, *Environmental Science and Technology*, 40, 2006, pp. 5181-5192.
- [16] C. Picioreanu, I.M. Head, K.P. Katuri, M.C.M. van Loosdrecht, K. Scott, A computational model for biofilm-based microbial fuel cells, *Water Research* 41, 2007, pp. 2921-2940.
- [17] I. Shizas, D.M. Bagley, Experimental determination of energy content of unknown organics in municipal wastewater streams, *Journal of Energy Engineering*, 130, 2004, pp. 45-53.
- [18] R.A. Rozendal, H.V.M. Hamelers, K. Rabaey, J. Keller, C.J.N. Buisman, Towards practical implementation of bioelectrochemical wastewater treatment, *Trends in Biotechnology*, 26, 2008, pp. 450-459.

Development of laccase and manganese peroxidase biocathodes for microbial fuel cell applications

Sahar Bakhshian¹, Hamid-Reza Kariminia^{1,*}

¹ Department of Chemical and Petroleum Engineering, Sharif University of Technology, Tehran, Iran

* Corresponding author. Tel: +98 21 66166426, Fax: +98 21 66166426, E-mail: kariminia@sharif.ir

Abstract: In this study, we investigated how microbial fuel cell (MFC) performance can be affected by laccase and manganese peroxidase (MnP) enzymes as catalysts in the cathode compartment. Commercial laccase was immobilized by crosslinking on chitosan using glutaraldehyde. Immobilized enzyme was settled on graphite electrode previously covered with polymerized methylene blue. Application of this enzymatic electrode was investigated in the cathode chamber of a MFC. Output power density of the MFC in the mentioned situation was 100% higher than that for the graphite electrode. The MnP was first, produced from a white rot fungus isolate and was immobilized on the graphite electrode via adsorption. This modified electrode with MnP was utilized as cathode. The fuel cell with MnP modified graphite electrode and H₂O₂ as oxidizer yielded the maximum power density of 46 mW/m² at the current density of 109 mA/m². This augmentation of MFC performance was due to a higher cathode electrode potential with H₂O₂ rather than oxygen. The most important function of MnP was to catalyze the reduction of H₂O₂ and hence diminished activation overpotential loss of the cathode.

Keywords: Biocathode, Laccase, Manganese peroxidase, Microbial fuel cell

1. Introduction

Microbial fuel cells are devices that generate electricity by oxidation of organic substrates using bacterial metabolism. This technology is considered as a non-polluting and a new source of renewable energy [1,2,3].

Oxygen is a preferable oxidant in the cathode compartment of MFC because of its availability and its environmental friendly reduction product *i.e.* water [4]. Platinum has been applied as main catalyst to improve oxygen reduction rate in the cathode chamber; but it imposes high cost on MFC construction [5].

Application of biocatalysts as an inexpensive alternative to platinum is a potential solution [4]. Application of these components under moderate (ambient) temperatures and neutral pH are the main advantages of them over conventional catalysts [6]. Laccase, bilirubin oxidase and peroxidase like manganese peroxidase (MnP) has been used as biocatalysts in cathode of a MFC [6,7].

Laccase (E.C. 1.10.3.2, *p*-benzenediol: oxygen oxidoreductase) is a multi-copper oxidase enzyme in plants, fungi and some bacteria which can catalyze the oxidation of phenolic and other aromatic compounds resulting in four-electron reduction of oxygen to water [8]. The active site of laccase contains four copper atoms as redox centers, classified in three types, T₁, T₂ and T₃. The T₁ site is reduced by oxidation of substrate or involving in polarized electrode. Four electrons are transferred from T₁ site to T₂ and T₃ sites where, O₂ is reduced to H₂O [9,4]. Palmore et al. have studied the application of fungal laccase in the cathode compartment of a dihydrogen/dioxygen biofuel cell. Reduction of dioxygen to water with laccase was mediated by redox mediator, 2,2'-azinobis (3-ethylbenzothiazoline-6-sulfonate). They concluded that a biocatalyst with specific activity of 10³ U/mg has a higher catalysis rate than a platinum as catalyst in the cathode compartment [4].

Manganese peroxidase (MnP) (EC 1.11.1.13) is one of the major ligninolytic enzymes that can be produced by white rot fungi. This enzyme is a heme containing glycoprotein that uses hydrogen peroxide as oxidant and reduce it to water [10,11].

In this study, methylene blue was electropolymerized on graphite electrode as an electrical active polymer that can enhance electron transfer. Commercial laccase was immobilized by crosslinking on chitosan with glutaraldehyde. Immobilized laccase was settled on a graphite electrode covered with polymethylene blue and this enzymatic electrode was applied in a dual chamber MFC as cathode electrode. In another attempt, MnP produced from a white rot fungus isolate was immobilized on graphite electrode via adsorption. Effect of this biocathode electrode was also investigated on the MFC performance.

2. Methodology

2.1. Microbial fuel cell assembly

The MFC setup consisted of two 250 ml chambers joined through a short tube. Nafion 117 was utilized as membrane with 1.5 cm diameter separating two compartments. Pretreatment of the membrane was conducted by soaking it in a 0.1 M H₂SO₄ solution, H₂O₂ solution and deionized water, each for 60 min at 60°C. Anode and cathode electrodes were 6cm×2cm and 4cm×2cm graphite bars, respectively. These two electrodes were connected with a copper wire. The anode chamber was inoculated with anaerobic sludge and both chambers were mixed gently by a magnetic stirrer.

Nutrient medium (pH 7) utilized in the anode chamber consisted of molasses (1 g/l), K₂HPO₄, urea and trace elements (0.4 mg/l FeCl₃, 3 mg/l MgSO₄, 0.11 mg/l CuSO₄.5H₂O, 0.7 mg/l NaCl, 0.015 mg/l ZnCl₂, 4 mg/l Na₂S₂O₅, 0.254 mg/l MnSO₄.H₂O, 2.06 mg/l FeSO₄.7H₂O). All experiments were performed at the ambient temperature (28±1°C).

2.2. Microorganism and enzyme

Commercial laccase was prepared from AB Enzymes GmbH, Germany. A lignolytic fungus isolated from rotted wood in Northern Iran was employed for the production of MnP. This isolate had indicated the capability to produce MnP as its main lignolytic enzyme. As much as 50 ml of the culture broth (30 g/l glucose, 10 g/l peptone, 5 g/l yeast extract and 0.1 mM Mn²⁺, pH 4) was prepared in 250 ml Erlenmeyer flasks and autoclaved (121⁰ C, 15 min). One mycelia piece of the isolated fungus was placed in the center of an autoclaved 3.9% potato dextrose agar plate and incubated at 32⁰ C. After 7 days of cultivation, a mycelial plug (diameter 10 mm) of this culture was used as the inoculum. The cultivation was conducted in a rotary shaker with the rotation speed of 160 rpm at 32⁰ C. After 14 days, when a maximum activity for the extracellular MnP was observed, the enzyme was collected from the culture broth by centrifugation (5,000 rpm for 30 m in). The supernatant then was utilized for immobilization on the graphite electrode.

2.3. Preparation of enzymatic biocathodes

Electropolymerization of methylene blue was performed by cyclic voltammetry using a potentiostat – galvanostat EG&G PAR 273A, Princeton Applied Research, US from -0.5 to 1.2 V for 18 scans at a scan rate of 50 mV/s [13]. Electrolyte solution contained 0.01 M borate buffer (pH 9.1), 0.1 M NaNO₃ and 0.4 mM methylene blue. In another study, the optimal monomer concentration was found to be 0.4 mM. As basic electrolyte solution, 0.1 M NaNO₃ was used. Nitrate ions have catalytic role on electropolymerization of methylene blue. Graphite electrode (12 cm²) was polished with emery paper and rinsed with distilled water

prior to use. The reference and counter electrodes were saturated calomel electrodes (SCE, 0.241 V vs. SHE) and platinum sheet (2 cm²), respectively.

Crosslinking method was employed for laccase immobilization. The enzyme was immobilized on chitosan using glutaraldehyde [12]. A 5 g/l chitosan solution was prepared using a 2% acetic acid solution to dissolve chitosan. By addition of 2 M NaOH to this solution, a white flocculent deposit was formed and separated from the wet chitosan carrier. The flocculent was washed with distilled water several times and then 20 ml of a 5% glutaraldehyde solution was added. In order to associate the glutaraldehyde to the enzyme, the solution was mixed for 8 h and then left overnight. After that, the deposit was washed with water and added to 50 ml of a 20 g/l laccase solution. Then, 5 ml of acetate buffer (pH 4.4) was added to the solution, agitated for 16 h at room temperature and incubated at 4°C, overnight. The resulting settlement was immobilized laccase on chitosan. Then, 1 ml of the immobilized laccase on chitosan was pipetted onto the electropolymerized (polymethylene blue) graphite electrode and left to dry in a vacuum desiccator for 1 hour. Glutaraldehyde molecule includes two aldehyde group (-CHO) in its structure in which one of these groups react with amine group (-NH₂) of chitosan and crosslinking takes place. The free aldehyde group of glutaraldehyde binds to an amine group of laccase, covalently. Therefore, glutaraldehyde plays the crosslinking agent role in the linkage of laccase to chitosan.

MnP was immobilized to the graphite electrode by adsorption. As much as 1 ml of the produced crude MnP was pipetted onto the graphite electrode and left to dry in a vacuum desiccator for 1 hour.

2.4. Laccase and MnP activity assay

Laccase activity measurement was performed spectrophotometrically at 25° C, using 2,2-azino-bis-(3-ethylbenzothiazoline-6-sulfonic acid) or ABTS as substrate. The mixture of reaction was contained 3 ml sodium acetate buffer (1 mM, pH 4.5), 0.1 ml ABTS (0.5 mM) and 0.1 ml enzyme solution. The reaction started by addition of ABTS solution (0.1 ml). The rate of ABTS⁺ formation was measured spectrophotometrically at 420 nm. One unit of the enzyme activity (U) determined as the amount of the enzyme necessary to produce 1 μmol of oxidized ABTS per minute [14].

MnP was assayed by the formation of Mn³⁺ in 50mM sodium malonate buffer (pH 4.5), using 0.1 Mm H₂O₂ as substrate. The rate of complex formation between manganic ions Mn³⁺ and malonate was measured spectrophotometrically at 270 nm. One unit of MnP activity defined as the amount of the enzyme necessary to produce 1 μmol of Mn³⁺ per minute at 25° C [15].

3. Results and Discussion

3.1. Electropolymerization of methylene blue on graphite

Methylene blue was polymerized on the surface of a graphite electrode. According to cyclic voltammogram of polymethylene blue on the graphite (Fig. 1), the peaks appeared at high anodic potential (almost 1 V) are related to the irreversible oxidation of the monomer. Other peaks are formed due to polymerization of formed cation radicals of methylene blue. Therefore, after oxidation of methylene blue and formation of radicals, chemical reaction related to the polymerization of these radicals had been taken place. Methylene blue which is an electroactive polymer was utilized as a mediator due to its high conductivity. Polymethylene blue could increase electron transfer from the electrode to active sites of the laccase. Therefore, electron access will be improved after polymerization of methylene blue

on the electrode surface. As a result, mediator utilization will influence oxygen reduction to water, catalyzed by the laccase in the cathode compartment.

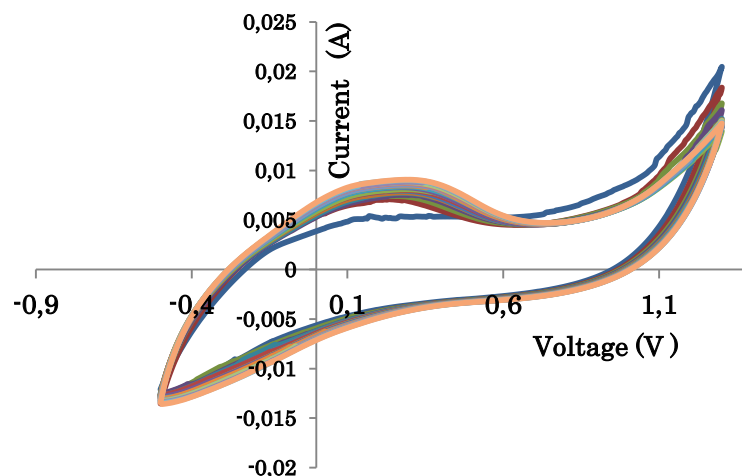


Fig 1. Cyclic voltammogram of methylene blue on graphite electrode (Scan rate 50 mV/s).

3.2. MFC performance in the presence of laccase

The polarization curve that was obtained by changing the external load at the maximum output voltage of the MFC, indicates the cell voltage drop and power dependence on current. In general, power density increases to a maximum value against current density and then sharply decreases. Polarization and power curve of the cathode electrodes were plotted at the maximum voltage of the MFC when each of graphite, polymerized graphite or enzymatic electrode was used.

The polarization curves of graphite, polymerized graphite and laccase immobilized graphite are shown in Fig. 2. Maximum current density of the MFC for the polymerized graphite as cathode was 20% higher than that for the graphite electrode. This increase in the current density is due to electron transfer improvement because of improved conductivity of the polymerized graphite electrode.

The power curves of graphite, polymerized graphite and laccase immobilized graphite are indicated in Fig. 3. The maximum power density for the enzymatic electrode was 45.2 mW/m² at the current density of 175 mA/m², which was two folds of that for the graphite electrode (maximum power density of 22.3 mW/m² at current density of 106.9 mA/m²). The maximum power density for the polymerized graphite electrode was 31 mW/m² at the current density of 140.6 mA/m². The power density improved 40% in comparison to the graphite electrode. The maximum power density for graphite, polymerized and enzymatic graphite occurred at the external load of 1.2, 98 and 92 k Ω , respectively. According to Ohm's law, at maximum power density, external load is equal to the internal load of MFC. Therefore, modification of graphite electrode through electropolymerization and enzyme immobilization causes a reduction in the internal resistance of the MFC. This phenomenon occurs due to the improvement of electron transfer when polymerized methylene blue or laccase is used on the graphite electrode and the internal resistance of the system decreases, accordingly.

Fig. 3 also indicates that the slope of polarization curve for the enzymatic electrode is milder than that for the graphite electrode at lower current densities. This observation suggests that the activation overpotential of the enzymatic electrode is less than the graphite electrode.

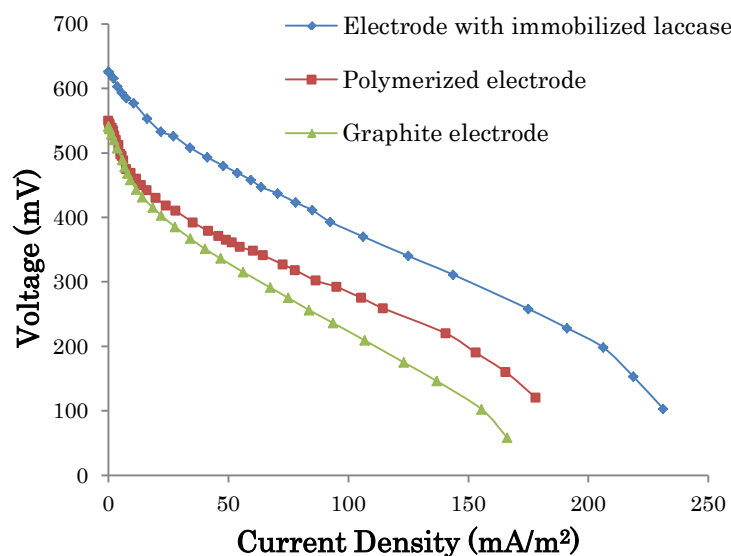


Fig. 2. Polarization curve of MFC with three different electrodes.

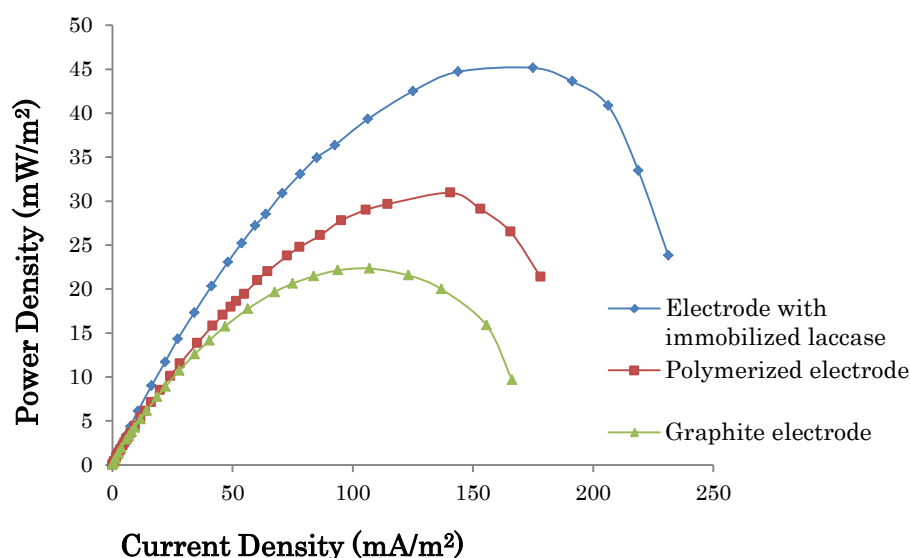


Fig. 3. Power density curve of MFC with three different.

3.3. MFC performance in the presence of MnP

The time course of open circuit voltage variation of the MFC after addition of H_2O_2 is shown in Fig. 4. After H_2O_2 addition, the voltage rapidly increased to a maximum value and then gradually decreased to a constant value. The voltage increase is related to a higher cathodic potential of H_2O_2 compared to oxygen potential. The MFC performance during this stable condition is shown in the polarization and power curves (Fig. 5 and Fig. 6). Maximum output power of 46 mW/m^2 was obtained at current density of 108.8 mA/m^2 . This power density is 106% higher than that for a non-enzymatic cathode. The slope of polarization curve for MnP with immobilized MnP cathode at low current densities is 54% less than that for the non-enzymatic cathode. Therefore, MnP presence in the cathode reduces cathodic and overall activation overpotential which is attributed to the catalytic role of MnP in the cathode.

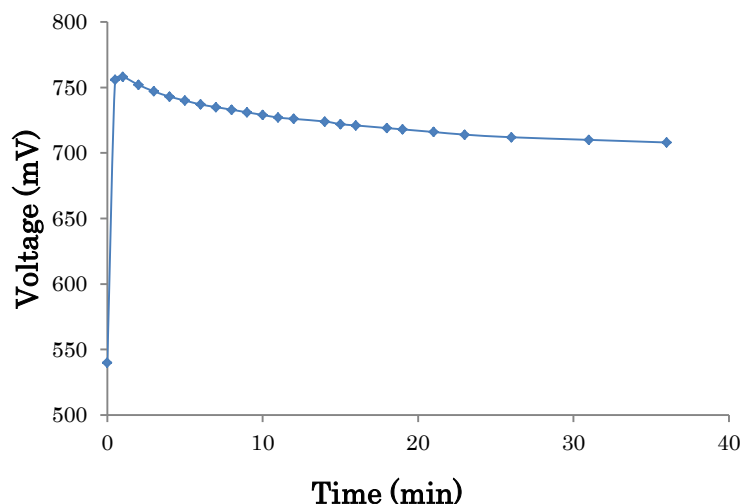


Fig. 4. Open circuit voltage-time curve of MFC after H_2O_2 addition to the cathode in the presence of MnP.

MnP can catalyze hydrogen peroxide reduction to water. Reduction of H_2O_2 causes the oxidation of heme group of the enzyme. The oxidized heme group needs to be reduced to keep its activity which can be fulfilled electrochemically or by an electron donor molecule. Here, Mn^{2+} acts as electron donor. Electrons generated through Mn^{2+} oxidation will be transferred to the active sites of the enzyme and will be utilized to reduce H_2O_2 to water. The produced Mn^{3+} ions extract electrons presented on the cathode surface. The cathodic reaction is catalyzed by MnP enzyme through repetition of the mentioned reactions, cyclically.

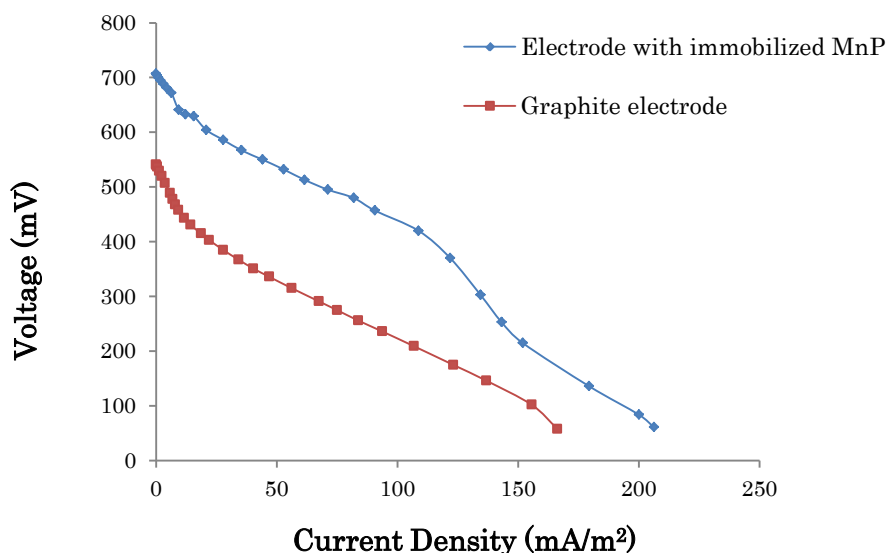


Fig. 5. Polarization curve of MFC with two different electrodes.

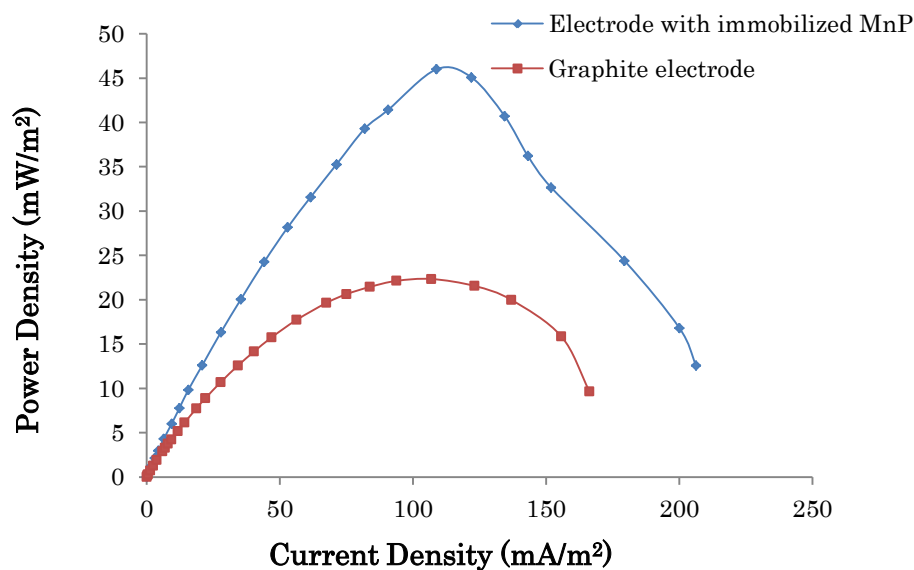


Fig. 6. Power density curve of MFC with three different electrodes.

4. Conclusion

Commercial laccase and MnP produced from a white rot fungus isolate were immobilized on graphite electrode and used as new renewable catalysts in the cathode compartment of a dual chamber MFC. Application of these electrodes in the cathode, enhanced the MFC performance. Output voltage and current density increased as two times as output voltage of the MFC with non-enzymatic cathode. Activation overpotential of MFC decreased due to the catalytic effect of laccase and MnP on reduction of oxygen and H₂O₂, respectively. Laccase and MnP can be proposed as innovative catalysts to be applied in MFCs in order to achieve higher performance via improvement of reaction kinetic in the cathode and therefore, reduction of its related overpotential.

References

- [1] B.E. Logan, B. Hamelers, R. Rozendal, U. Schröder, J. Keller, S. Freguia, P. Aelterman, W. Verstraete and K. Rabaey, *Microbial fuel cells: methodology and technology*, Environmental Science and Technology, 2006, pp. 307-314.
- [2] Z.-D. Liu, H.-R. Li, Effects of bio- and abio-factors on electricity production in a mediatorless microbial fuel cell, *Biochemical Engineering Journal*, 2007, pp. 209-214.
- [3] R.D. Lovely, *Microbial fuel cells: novel microbial physiologies and engineering approaches*, *Current Opinion in Biotechnology*, 2006, pp. 327-332.
- [4] G. Tayhas, R. Palmore, H.H. Kim, Electro-enzymatic reduction of dioxygen to water in the cathode compartment of a biofuel cell, *Journal of Electroanalytical Chemistry*, 1999, pp. 110-117.
- [5] O. Lefebvre, W.K. Ooi, Z. Tang, Md. Abdullah-Al-Mamun, D.H.C. Chua, H.Y. Ng, Optimization of a Pt-free cathode suitable for practical applications of microbial fuel cells, *Bioresource Technology*, 2009, pp. 4907-4910.
- [6] M. Smolander, H. Boer, M. Valkiainen, R. Roozemana, M. Bergelin, J. E. Eriksson, X. C. Zhang, A. Koivula, L. Viikari, Development of a printable laccase-based biocathode for fuel cell applications, *Enzyme and Microbial Technology*, 2008, pp. 93-102.

- [7] R.A. Bullen, T.C. Arnot, J.B. Lakeman, F.C. Walsh, Biofuel cells and their development, *Biosensors and Bioelectronics*, 2006, pp. 2015-2045.
- [8] N. Duran, M. Rosa, A.D. Annibale, L. Gianfreda, Application of laccases and tyrosinases (phenoloxidases) immobilized on different supports: a review, *Enzyme and Microbial Technology*, 2002, pp. 907-931.
- [9] C. Vaz-Dominguez, S. Campuzano, O. Rudiger, M. Pita, M. Gorbacheva, S. Shleev, V. M. Fernandez, A.L.D. Lacey, Laccase electrode for direct electrocatalytic reduction of O₂ to H₂O with high-operational stability and resistance to chloride inhibition, *Biosensors and Bioelectronics*, 2008, pp. 531-537.
- [10] H.-R. Karimniaae-Hamedani, A. Sakurai, M. Sakakibara, Decolorization of synthetic dyes by a new manganese peroxidase-producing white rot fungus. *Dyes and Pigments*, 2007, pp. 157-162.
- [11] M. Hofrichter, Review: lignin conversion by manganese peroxidase (MnP), *Enzyme and Microbial Technology*, 2003, pp. 454-466.
- [12] J. Zhang, Z. Xu, H. Chen, Y. Zong, Removal of 2,4-dichlorophenol by chitosan-immobilized laccase from *Coriolus versicolor*, *Biochemical Engineering Journal*, 2009, pp. 54-59.
- [13] A.A. Karyakin, E.E. Karyakina, H.-L. Schmidt, Electropolymerized azines: a new group of electroactive polymers, *Electroanalysis*, 1999, pp. 149-155.
- [14] X.Q. Yang, X.X. Zhao, C.Y. Liu, Y. Zheng, S.J. Qian, Decolorization of azo, triphenylmethane and anthraquinone dyes by a newly isolated *Trametes* sp. SQ01 and its laccase, *Process Biochemistry*, 2009, pp. 1185-1189.
- [15] H. Wariishi, K. Valli, M.H. Gold, Manganese (II) oxidation by manganese peroxidase from the basidiomycete *Phanerochaete chrysosporium*, *Journal of Biological Chemistry*, 1992, pp. 23688-23695.

Numerical Studies of PEM Fuel Cell with Serpentine Flow-Field for Sustainable Energy Use

Sang-Hoon Jang¹, GiSoo Shin¹, Hana Hwang¹, Kap-Seung Choi¹, Hyung-Man Kim^{1,*}

¹ Department of Mechanical Engineering & High Safety Vehicle Core Technology Research Center, INJE University, 607 Eobang-dong, Gimhae-si, Gyongsangnam-do 621-749, Republic of Korea

* Corresponding author. Tel: +82 55 320 3666, Fax: +82 55 324 1723, E-mail: mechkhm@inje.ac.kr

Abstract: This paper proposes the numerical analyses on performance for PEMFC in the aspects of water management and distribution of current density were performed to compare serpentine channel flow field of 5 passes 4 turns serpentine and 25cm² reaction surface between with and without sub-channel at rib. Through the supplement of sub-channel flow field, the improvement of water removal characteristic inside channel was confirmed from the numerical results because the flow direction of under-rib convection is changed into the sub-channel. Reacting gases supplied from entrance disperse into sub-channel flow field and electrochemical reaction occurs uniformly over the reaction surface. Therefore, it was also known that total current density distributions become uniform because retention time of reacting gases traveling to sub-channel flow field is longer than main channel. At the averaged current density of 0.6 A/cm², the results show that output power for the serpentine flow-field with sub-channel is 8.475 W which is decreased by about 0.35 % compared with 8.505 W for the conventional-advanced serpentine flow-field, whereas the pressure drops on the anode and cathode side for the serpentine flow-field with sub-channel are 0.282 kPa and 1.321 kPa which are decreased by about 22.95 % and 17.12 % compared with 0.366 kPa and 1.594 kPa for the conventional-advanced serpentine flow-field, respectively.

Keywords: PEM Fuel Cell, Current density, Water management, Under-rib convection, Sub-channel

1. Introduction

Proton exchange membrane fuel cell (PEMFC) has been considered one of the most promising alternative clean power generators because of its low to zero emission, its low temperature operation, high power density, and high efficiency [1]. Currently, many researchers have studied the bipolar plate considered performance and water management in the flow channel. Kanazaki [2] and Nam [3] have found that under-rib convection flow between adjacent channels. The under-rib convection is believed to increase the reactant concentration in the under-rib regions, facilitate liquid water removal from those regions, and enable a more uniform concentration distribution, thus explaining an experimental result of good cell performance.

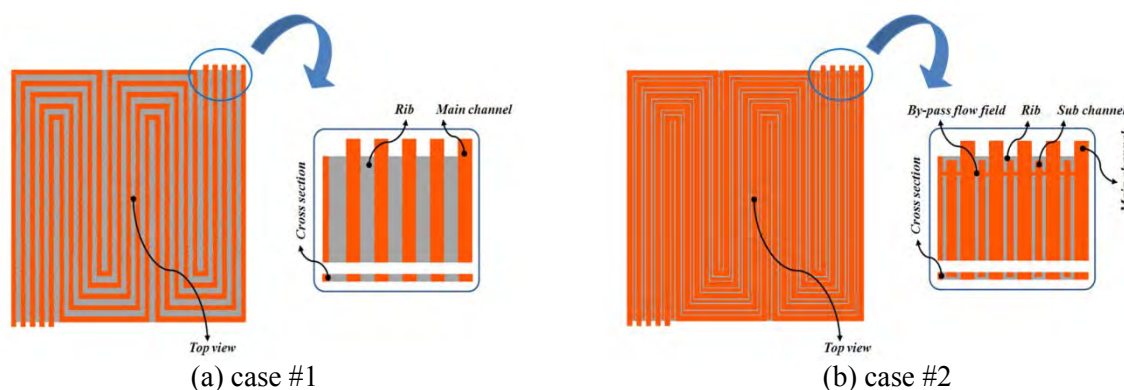


Fig. 1. Two 25cm² serpentine flow-field patterns; (a) case #1 (without sub-channel); (b) case #2 (with sub-channel).

This paper proposes the numerical analyses on performance for PEMFC in the aspects of water management and distribution of current density were performed to compare serpentine channel flow fields of 5-passes and 4-turns serpentine and 25cm² reaction surface between with and without sub-channel at rib. Two serpentine flow-field patterns are shown in Fig. 1.

2. Numerical model

In this study, CFD programs based on STAR-CD and ES-PEMFC were used to solve the fully coupled governing equations. The model assumes a steady state, ideal gas properties, and homogeneous two phase flows. Assuming that liquid film is formed on the electrode surface during liquid water condensation, the Henry's law of the solubility of gases in the liquid water is used to calculate the diffusion flux, electro-osmotic drag force, and water back diffusion [4, 5]. To improve the computational accuracy, grid cells were established by equalizing the node connectivity in each component and by using the hexahedron mesh. The number of computational cells used in the model varied with complexity of the model. For the case #1, the total cell number was 3.078 million cells, case #2 had 3.336 million computational cells. The present numerical model was validated by grid tests and numerical simulation results on 10cm² serpentine with single channel flow-field PEMFC [4].

3. Results and discussion

The parametric studies were conducted on 25 cm² serpentine channels that have the case #1 and case #2 configurations, all under the same operating conditions and inlet flow velocity as listed in Table 1 and Table 2. The performance-related parameters include membrane water content (λ), net water flux per proton (α), pressure drop, current density. They are investigated to generate the optimum serpentine flow-field that enhances the PEMFC performance. The net water flux per proton expresses the water transport between anode and cathode. If the net water flux per proton is greater than 0, the electro-osmotic drag is higher than the back diffusion, and water is transported from the anode to the cathode. On the other hand, the net water flux per proton is less than 0 mainly in the outlet area under the ribs, and water is transported from the cathode to the anode by the back diffusion. Back diffusion occurred due to the concentration of water on the anode is higher than on the cathode.

Table 1. Inlet conditions at Anode and Cathode.

Anode	Inlet conditions	Cathode	Inlet conditions
Gas	Hydrogen	Gas	Air
Stoichiometry	1.5	Stoichiometry	2.0
Inlet temperature (°C)	75	Inlet temperature (°C)	75
Inlet relative humidity (%)	100	Inlet relative humidity (%)	100
Mass fraction of hydrogen	0.078	Mass fraction of hydrogen	0.169
Mass fraction of water	0.561	Mass fraction of water	0.274

Table 2. Operating conditions at $I_{ave} = 0.6A/cm^2$.

Operating conditions	
%H ₂ in reformat	75
Exit pressure (kPa)	101
H ₂ exchange current density (A/cm ²)	2000
O ₂ exchange current density (A/cm ²)	200
Open circuit voltage (V)	0.96
Cell temperature (°C)	75

Fig. 2 ~ Fig. 4 show the comparison of the membrane water contents (λ), net water flux per proton (α) and current density distributions at averaged current density of 0.6 A/cm^2 .

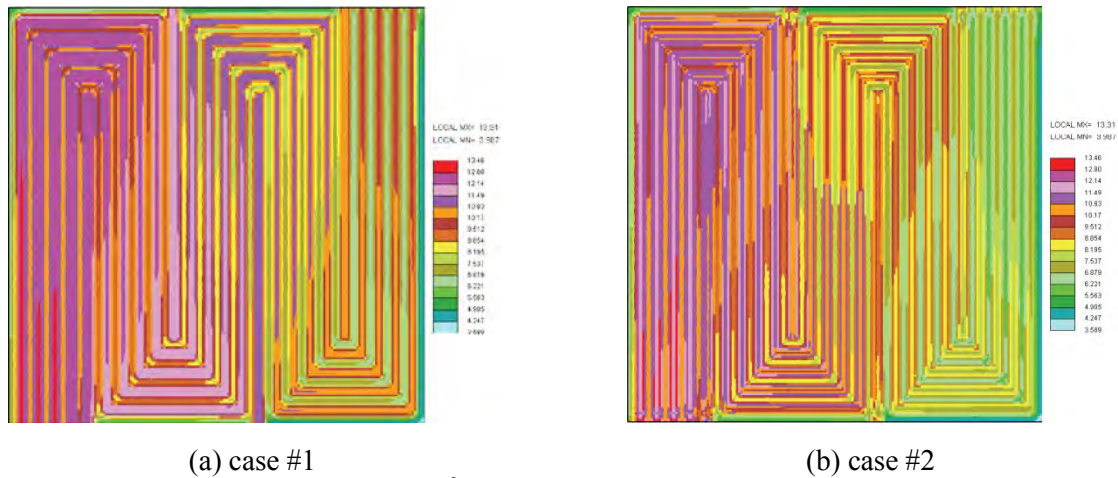


Fig. 2. Water content (λ) at $I_{ave}=0.6 \text{ A/cm}^2$; (a) case #1; (b) case #2.

Fig. 2 shows the comparison of the membrane water contents between the case #1 and case #2 at the averaged current density of 0.6 A/cm^2 . The membrane water content under the rib area is higher than that under the adjacent channel area because a lot of water produced at the cathode under the rib region can be absorbed into the membrane as shown in case #1. On the other hand, the membrane water content of the case #2 has smaller variation between the channel and rib than that of the case #1 because under-rib convection flow from channel to the adjacent rib and then flow from the inlet channel to the adjacent outlet channel, and liquid water gathers and discharges into sub-channel.

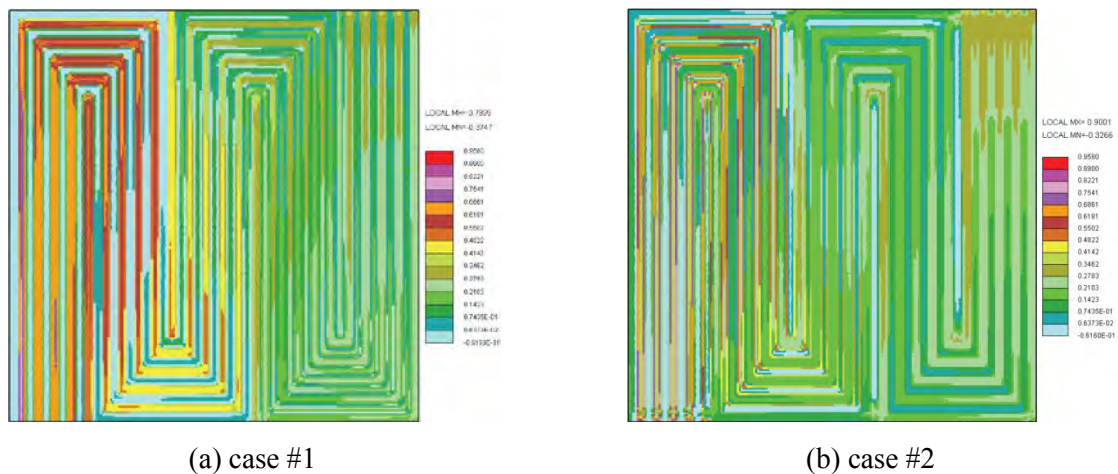


Fig. 3. Net water flux per proton (α) at $I_{ave}=0.6 \text{ A/cm}^2$; (a) case #1; (b) case #2.

Fig. 3 shows the comparison of the net water flux per proton between the case #1 and case #2 at the averaged current density of 0.6 A/cm^2 . The net water flux per proton is greater than 0 at the ribs and that is less than 0 at the channels as shown in case #1. The net water flux per proton is always greater than at the ribs because the hydrogen ions are transported from cathode to the anode with a lot of water. Case #2 shows that the net water flux per proton at the ribs is lower due to sub-channel than the net water flux per proton at the channels i.e. a lot of water is transported from cathode to the anode.

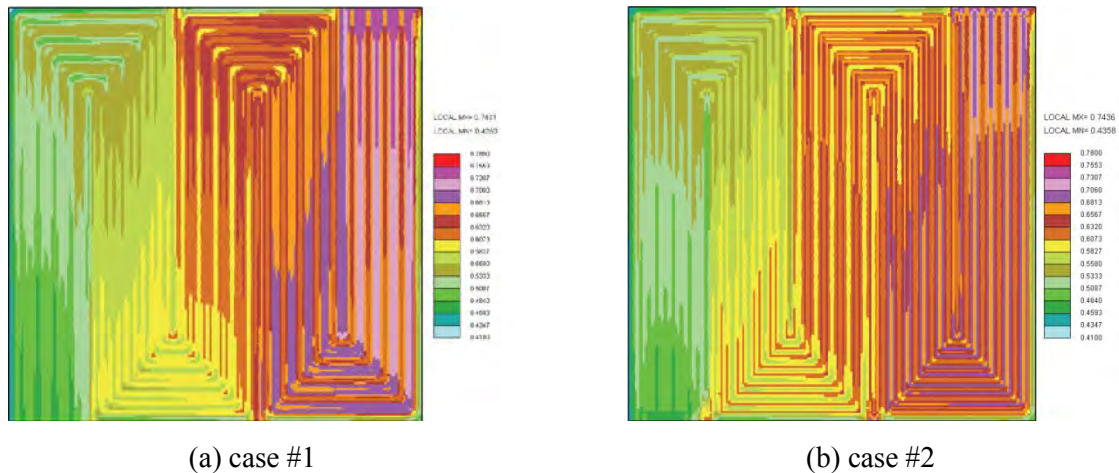


Fig. 4. Current density distributions at $I_{ave}=0.6 A/cm^2$; (a) case #1, case #2.

Fig. 4 presents the comparison of the current density distributions between the case #1 and case #2 at the averaged current density of $0.6 A/cm^2$. The overall distributions show that the local current density is decreasing from the inlet toward the outlet due to the consumption of the reacting gases. Through the supplement of sub channel flow field, it is shown from the results that water removal characteristic inside channel improves because the flow direction of under-rib convection is changed into the sub channel. Therefore, case #2 shows that total current density distributions become uniform because retention time of reacting gases traveling to sub channel flow field is longer than to main channel.

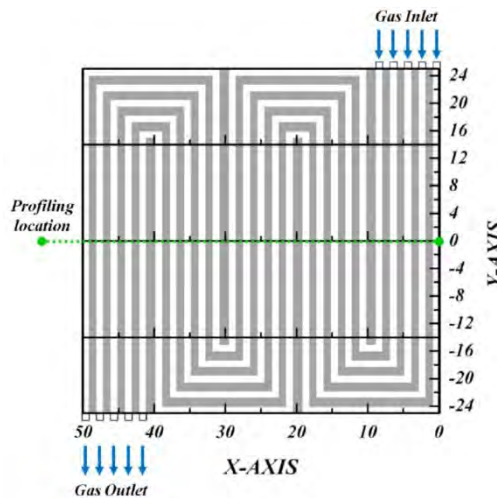


Fig. 5. Index and location of the serpentine flow-field.

Fig. 6 shows the comparison of the total pressures between the case #1 and case #2 at the averaged current density of $0.6 A/cm^2$ and the same location as shown in Fig. 5. The pressure drops on the anode and cathode side for case #2 are 0.282 kPa and 1.321 kPa which are decreased by about 22.95 % and 17.12 % compared with 0.366 kPa and 1.594 kPa for case #1, respectively. The enhanced under-rib convection in both anode and cathode of case #2 decreases the pressure drop, which also contributes to the performance by reducing the power consumption of air blower.

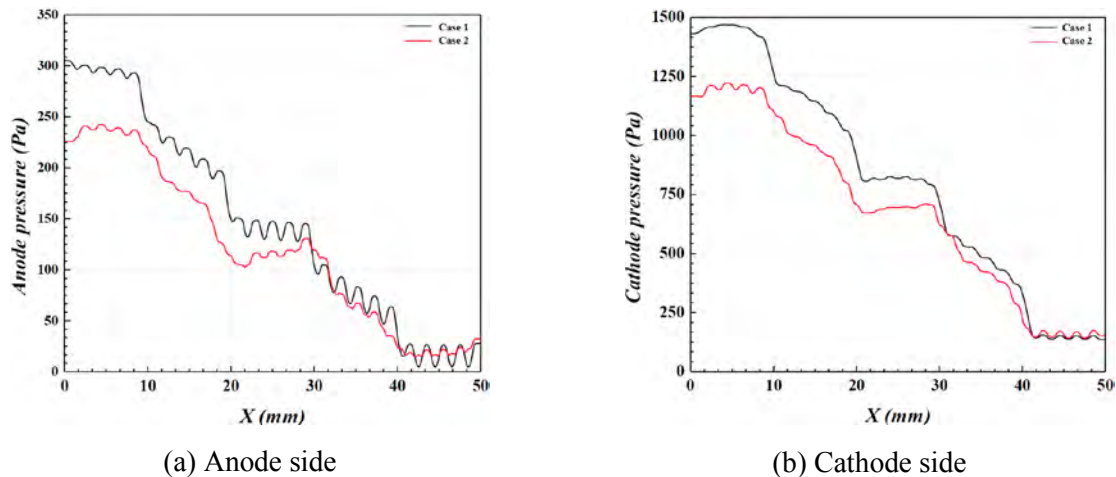


Fig. 6. The comparison of the total pressures between the case #1 and case #2 at $I_{ave}=0.6 A/cm^2$; (a) Anode side; (b) Cathode side.

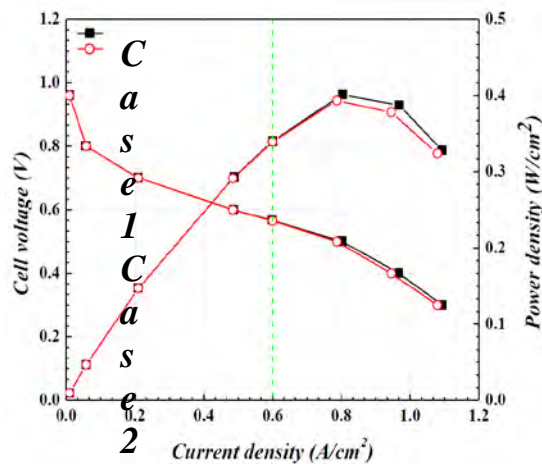


Fig. 7. The comparison of the polarization and power density curves between the case #1 and case #2.

To verify the maximization of power density among the performance-related parameters, the comparison of the polarization and power density curves between the case #1 and case #2 is given in Fig. 7. For the current density lower than $0.6 A/cm^2$, the cell voltage and power density is independent of serpentine flow-field with and without sub-channel. For the current density greater than $0.6 A/cm^2$, the cell voltages and power densities of case #1 and case #2 differ, the differences increase with the decreasing current density.

4. Conclusions

This study presents numerical analysis-based design of the serpentine flow field patterns to stimulate under-rib convection by adding sub-channel for improving the PEMFC performance. In the case of the case #2, under-rib convection flow from channel to the adjacent rib and then flow from the inlet channel to the adjacent outlet channel, and liquid water gathers and discharges into the sub-channel. Through the present numerical analysis-based design, the serpentine flow field with sub-channel enhances the performances of pressure drop, discharge of liquid water, and uniformities of current density.

Acknowledgements

This research was supported by Basic Science Research Program through the National Research Foundation of Korea (NRF) funded by the Ministry of Education, Science and Technology (No. 2009-0080496).

References

- [1] F. Barbir, PEM Fuel Cells: Theory and Practice, Elsevier Academic Press, 2005.
- [2] T. Kanezaki, X. Li and J.J. Baschuk, Cross-leakage flow between adjacent flow channels in PEM fuel cells, *J. Power Sources* 162, 2006, pp. 415 – 425.
- [3] J.H. Nam, K.J. Lee, S.Sohn, C.H. Kim, Multi-pass serpentine flow-fields to enhance under-rib convection in polymer electrolyte membrane fuel cells: Design and geometrical characterization, *J. Power Sources* 188, 2009, pp. 14 – 23.
- [4] D.H. Jeon, S. Greenway, S. Shimpalee and J.W. Van Zee, The Effect of Serpentine Flow Field Designs on PEM Fuel Cell Performance, *Int. J. Hydrogen Energy* 33, 2008, pp. 1052 – 1066
- [5] CD-adapco, ES-PEMFC Methodology and Tutorial Manual, CD-adapco Group, 2008, <http://www.adapco.com>.

Comparison of three anode channel configurations and their effects on DMFC performance

S.SH.Khoshmanesh^{1,*}, S.Bordbar²

¹ Islamic Azad University, Khormoj branch, khormoj, Boushehr, Iran

² Petroiran company, Tehran, Iran

* Corresponding author. Tel: +987726240716, Fax: +987726240286, E-mail: sharif.khoshmanesh@gmail.com

Abstract: Here the 3D two phase homogenous CFD modeling for the anode channel and 1D two phase mathematical modeling for the porous media were considered. The challenging issue is to define the interface boundary conditions such as gradient of CO₂ and methanol mass fraction between the diffuser layer and the anode channel. To overcome this difficulty, CFD modeling in the anode channel and mathematical modeling in the porous media were coupled. This combination models gives an accurate model to evaluate the cell performance and also to predict accumulation of CO₂ in the channel and its negative effects on the cell performance. Output results of the combination's model are in very good agreement with the experimental data. The distribution of CO₂ in the anode channel shows that the accumulation of CO₂ in the MSFF is less than SSFF and PFF configuration so the negative effect of CO₂ decrease in the MSFF case relative to two other cases. Accumulation of CO₂ is more in the channel rib relative to other places of channel. This is true for all three channel configurations. The cell voltage-Current density graph shows that the MSFF performance is better than two other cases. Comparing MSFF configuration with the SSFF shows that the performance of MSFF is a little more than SSFF.

Keywords: Direct methanol fuel cell, Anode flow configurations, CFD modeling, Mathematical modeling

Nomenclature

C_0 Average concentration of methanol at the channel/ADL interface..... molm^{-3}
 C_I Concentration of methanol at the ADL/ACL interface..... molm^{-3}
 C_{II} Concentration of methanol at the ACL/membrane interface..... molm^{-3}
 C Molar Concentration kmolm^{-3}
 D Diffusion coefficient m^2s^{-1}
 X Mass fraction
 F Faraday's constant, 96,487..... Cequiv
 I_{Cell} Cell current density..... Am^{-2}
 I_{Leak} Leakage current density Am^{-2}
 $I_{0,\text{ref}}^{\text{MeOH}}$ Exchange current density of methanol Am^{-2}
 $I_{0,\text{ref}}^{\text{O}_2}$ Exchange current density of oxygen Am^{-2}
 $N_{\text{Cross Over}}^{\text{MeOH}}$ Methanol crossover $\text{molm}^{-2}\text{s}^{-1}$
 P Pressure Pa
 T Temperature..... K
 U_{MeOH} Thermodynamic equilibrium potential of methanol oxidation..... Volt
 U_{O_2} Thermodynamic equilibrium potential of oxygen oxidation..... Volt
 V_{cell} Cell voltage..... Volt
 U_{O_2} Thermodynamic equilibrium potential of oxygen oxidation..... Volt

M Molecular weight km/kg

Greek

α_A Anodic transfer coefficient
 α_C Cathodic transfer coefficient
 δ_{AC} Anode Catalyst layer thickness..... m
 δ_{AD} Anode diffuser layer thickness..... m
 δ_M Membrane thickness..... m
 α Void fraction
 μ Dynamic viscosity..... $\text{kgm}^{-1}\text{s}^{-1}$
 ρ Density..... kgm^{-3}
 η_A Anode over potential..... Volt
 η_C Cathode over potential..... Volt
 ξ^{MeOH} Electro-osmotic drag coefficient of methanol
 κ Ionic conductivity of the membrane Scm^{-1}
 x' Quality

Subscripts

ADL Anode Diffuser Layer
 ACL Anode Catalyst Layer
 M Membrane

Superscripts

MeOH Methanol
 O₂ Oxygen
 CO₂ Carbon dioxide
 K Species

1. Introduction

Direct methanol fuel cells (DMFCs) are currently being investigated as an alternative power source to batteries for portable applications such as cell phones, laptop computers and video recorders. DMFCs with advantages of high energy density, rapid startup and response, low operation temperature, zero emission and refueling instantly, stand out as a most promising candidate to the applications of present and next generation of portable electronic devices [1, 2]. Regarding the DMFCs studies have been focused on two categories, materials of the cell and the anode electrochemical reaction. Water, methanol and gas management are the three main issues that some attempts have been investigated to optimize these effects on the cell performance. A good understanding of this complex, interacting phenomena to optimum the design parameters of system leads to numerous experimental and comprehensive mathematical modeling of cells.

Kulikovsky et al. [3] developed a vapor-feed two-dimensional DMFC model. Their model based on the mass conservation equations for concentrations of species and conservation equations of proton and electron currents, which govern the distributions of electrical potentials of the membrane and carbon phases. In his study, he neglected the methanol cross over the membrane.

Wang and Wang [4] presented a 2-D, two-phase model of liquid – feed DMFC. They extended their previous two-phase PEMFC model [5] to include two phase flow and transport phenomena in a liquid feed DMFC. 1-D drift flow model was used to describe the methanol flow in the anode channel.

Here a comprehensive 3-D, homogenous two phase model for the anode channel and 1D two phase mathematical modeling for the porous region were considered. This combination model results in the easily managing and optimizing of effective parameters on DMFC.

A typical DMFC consists essentially of a membrane-electrode assembly (MEA) sandwiched between two bipolar plates which have a channel for distribution the fuel, an aqueous methanol solution in the anode and oxygen from air in the cathode, Figure (1). In an operation DMFC, methanol solution diffuses through one of the porous diffusion layer and is oxidized at the anode to produce carbon dioxide, protons and electrons. At the cathode, Oxygen diffuses through another porous diffusion layer and is reduced with the proton passing through the proton exchange membrane as well as electrons flowing through load from the anode to produce water, equations (1), (2).

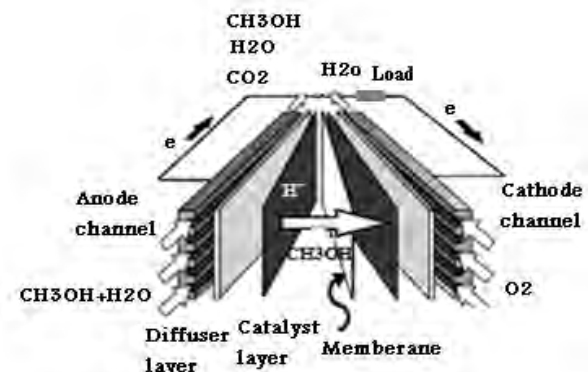


Fig. 1

2. Model description

Here 3-D homogenous, two phases, multi component flow for the anode channel and 1D two phase mathematical modeling for the porous regions were considered. For the anode channel

three type of flow patterns, parallel flow field (PFF), single-serpentine flow field (SSFF) and multiple serpentine flow field (MSFF) were considered, fig2.

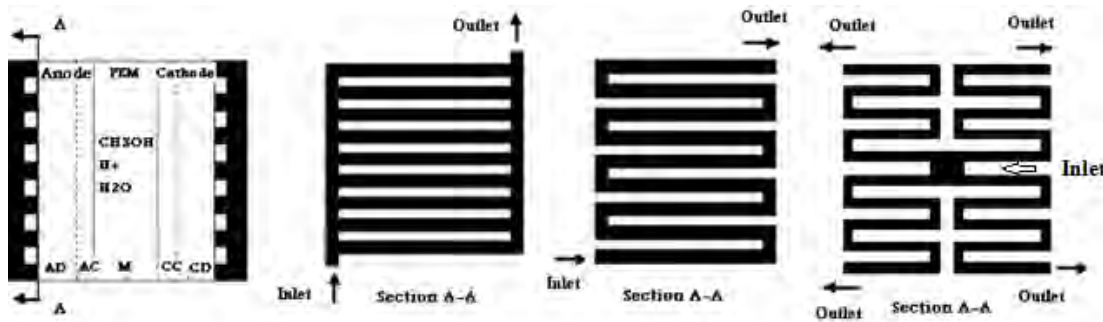


Fig. 2. Schematic view of DMFC with different anode configurations

The combination of CFD modeling and mathematical modeling has been shown in fig3.

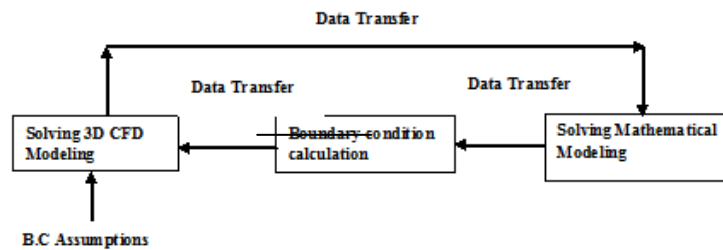


Fig. 3. Coupling CFD modeling and mathematical modeling

2.1. CFD modeling

In this study, two phase homogenous model have been used to describe the fluid flow in the anode channel. The study of Triplett [6], Fukano and Kariyasaki [7], showed that the homogeneous model is valid for two-phase bubbly flow because the tube diameter is smaller than 5.6 mm. In this model it is assumed that the thermodynamics equilibrium are available between the phases and two phases are well mixed and therefore travel with the same velocities so the mixture is treated as a pseudo-fluid that obeys the usual equations of single-phase flow.

$$\nabla \cdot (\rho^{mix} \vec{U}) = 0 \quad (3)$$

$$\nabla \cdot (\rho^{mix} \vec{U} \vec{U}) = -\nabla P + \nabla \cdot \vec{T} + \rho^{mix} g \quad (4)$$

$$T_{i,j} = \mu^{mix} \left(\frac{\partial u_i}{\partial x_j} + \frac{\partial u_j}{\partial x_i} - \frac{2}{3} \delta_{i,j} \frac{\partial u_n}{\partial x_n} \right) \quad (5)$$

$$\nabla \cdot (\rho^{mix} \vec{U} C^k) = \nabla \cdot (\rho^{mix} D^k \nabla C^k) \quad (6)$$

$$\rho^{mix} = \alpha \rho_l + (1 - \alpha) \rho_g \quad (8)$$

α is void fraction and related to quality x' by,

$$\alpha = \frac{1}{1 + \left(\frac{1-x'}{x'} \frac{\rho_g}{\rho_l} \right)} \quad (9)$$

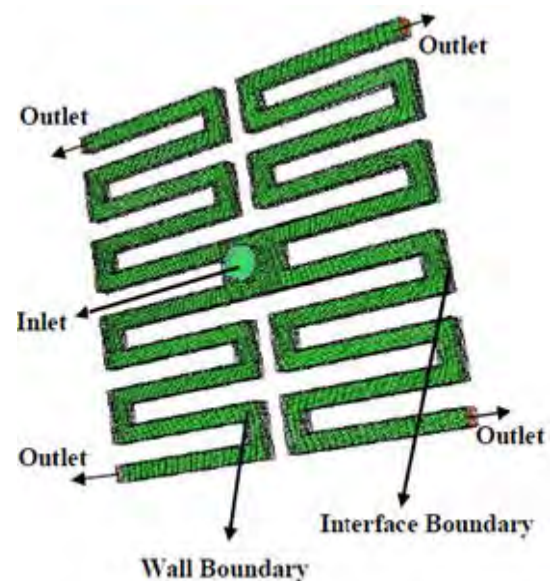


Fig. 4. MSFF configuration , boundary conditions and Meshing Scheme

$$x' = \frac{\rho_g(X_g^{CO_2} + X_g^{H_2O} + X_g^{MeOH})}{\rho_l(X_l^{H_2O} + X_l^{MeOH} + X_l^{CO_2})} \quad (10)$$

The Isbin equations have been used to calculate the mixture viscosity [8].

$$\frac{1}{\mu^{mix}} = x' \frac{1}{\mu_l} + (1 - x') \frac{1}{\mu_g} \quad (11)$$

2.2. Boundary Conditions

Fig 4 shows the view of MSFF with the different boundary conditions. In the inlet, mass flow rate of dilute methanol is defined. In the outlet, fully developed condition for the SSFF, MSFF and pressure outlet for the PFF is applied. In the boundary between the anode channel and diffuser layer the mass fraction of MeOH and CO₂ are defined.

2.2.1. Channel/ Anode diffuser layer interface boundary conditions

Consumed methanol in the anode catalyst layer and methanol cross over the membrane are equal to methanol transfer due to convection and diffusion in Channel/ Anode diffuser layer,

$$\rho^{mix} \vec{U} \cdot \vec{n} X^{MeOH} + \rho^{mix} D^{MeOH} \frac{\partial X^{MeOH}}{\partial x} = M^{MeOH} \frac{I_{cell}}{6F} + M^{MeOH} N_{Cross\ Over}^{MeOH} \quad (12)$$

The consumptions of the methanol, water and methanol crossover are equal to the total mass flow rate that goes out of the interface, so

$$\rho^{mix} \vec{U} \cdot \vec{n} = M^{MeOH} \frac{I_{cell}}{6F} + M^{MeOH} N_{Cross\ Over}^{MeOH} + M^{H_2O} \frac{I_{cell}}{2F} \quad (13)$$

If we replace the $\rho^{mix} \vec{U} \cdot \vec{n}$ from equation (16) into the equation (15) it gives the diffusion flux from the channel into the diffuser layer.

$$\rho^{mix} D^{MeOH} \frac{\partial X^{MeOH}}{\partial x} = M^{MeOH} \frac{I_{cell}}{6F} (1 - X^{MeOH}) + M^{MeOH} N_{Cross\ Over}^{MeOH} (1 - X^{MeOH}) + M^{H_2O} \frac{I_{cell}}{2F} X^{MeOH} \quad (14)$$

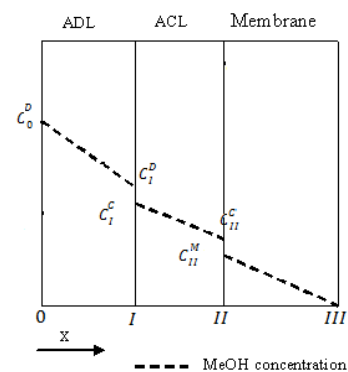
For the carbon dioxide the diffusion flux, which comes into the channel via the diffuser layer is equal to the CO₂ production in anode catalyst layer ,diffusion via convection neglected, so,

$$\rho^{mix} D^{CO_2} \frac{\partial X^{CO_2}}{\partial x} = M^{CO_2} \frac{I_{cell}}{6F} \quad (15)$$

2.3. Mathematical modeling

The porous media regions are divided to the diffuser, catalyst and membrane layer, Fig4. Mathematical modeling has been studied in the detail by Brenda[9]. Here only the results have been shown,

$$C_{AC}^{MeOH} = \frac{I_{Cell}}{12F\delta_{AC}D_{AC}^{MeOH}} X^2 + C_1X + C_2 \quad (16)$$



$$C_1 = \frac{C_{II}^C - C_I^C}{\delta_{AC}} - \frac{I_{Cell}(2\delta_{AD} + \delta_{AC})}{12F\delta_{AC}D_{AC}^{MeOH}} \quad (17)$$

$$C_2 = C_I^C - \frac{(C_{II}^C - C_I^C)\delta_{AD}}{\delta_{AC}} + \frac{I_{cell}\delta_{AD}(\delta_{AD} + \delta_{AC})}{12F\delta_{AC}D_{AC}^{MeOH}} \quad (18)$$

$$C_I^C = \frac{\delta_{AC}D_M^{MeOH}K_{II}\left(D_{AD}^{MeOH}C_0^D - \frac{I_{cell}\delta_{AD}}{12F}\right) + \delta_M D_{AC}^{MeOH}\left(D_{AD}^{MeOH}C_0^D - (1 + 6 \xi_{MeOH})\frac{I_{cell}\delta_{AD}}{6F}\right)}{D_{AD}^{MeOH}K_I(\delta_{AC}D_M^{MeOH}K_{II} + \delta_M D_{AC}^{MeOH}) + \delta_{AD}D_{AC}^{MeOH}D_M^{MeOH}K_{II}} \quad (19)$$

$$C_{II}^C = \frac{\delta_M(D_{AC}^{MeOH}D_{AD}^{MeOH}C_0^D - \delta_{AC}D_{AD}^{MeOH}K_I(1 + 12 \xi_{MeOH})\frac{I_{cell}}{12F} - \delta_{AD}D_{AC}^{MeOH}(1 + 6 \xi_{MeOH})\frac{I_{cell}}{6F})}{D_{AD}^{MeOH}K_I(\delta_{AC}D_M^{MeOH}K_{II} + \delta_M D_{AC}^{MeOH}) + \delta_{AD}D_{AC}^{MeOH}D_M^{MeOH}K_{II}} \quad (20)$$

The operation conditions, geometry and physicochemical properties have been come in table 1 and 2.

Table 1. Operation and Geometry values

Parameters	Symbols	Values
Operation Temperature	T	60°c
Operation Pressure	P	1At
Rib Height	H	0.001 (m)
Rib Width	W	0.0013 (m)
Diffuser layer thickness	δ_{AD}	0.0015 (m)
Catalyst layer thickness	δ_{AC}	0.00023(m)
Membrane layer thickness	δ_M	0.0018 (m)

Table 2. Physicochemical properties

Parameters	Symbols	Values	Ref
Binary diffusion coefficient	$D_{MeOH-Water}$	1.74×10^{-6}	[11]
Binary diffusion coefficient	$D_{CO2-Water}$	3.19×10^{-6}	[11]
MeOH diffusion coefficient,diffuser layer	D_{AD}^{MeOH}	8.7×10^{-3}	[9]
MeOH diffusion coefficient,catalyst layer	D_{AC}^{MeOH}	$2.8 \times 10^{-9} e^{2436(\frac{1}{353} - \frac{1}{T})}$	[12]
Methanol diffusion coefficient,memberane	D_M^{MeOH}	$4.9 \times 10^{-9} e^{2436(\frac{1}{353} - \frac{1}{T})}$	[12]
Thermodynamic potential of oxygen (Volt)	U^{O2}	1.24	[4]
Thermodynamic potential of methanol (Volt)	U^{MeOH}	0.03	[4]
Ref, exchange current density of anode (A/m2)	$I_{0,ref}^{MeOH}$	$94.25 e^{\frac{35570}{R}(\frac{1}{353} - \frac{1}{T})}$	[4]
Ref, exchange current density of cathode (A/m2)	$I_{0,ref}^{O2}$	$42.22 e^{\frac{73200}{R}(\frac{1}{353} - \frac{1}{T})}$	[15]
Anodic transfer coefficient	α_A	0.52	[4]
Cathodic transfer coefficient	α_C	1.55	[4]
Ionic conductivity of the membrane(S/Cm2)	κ	0.036	[11]
Electro-osmotic drag coefficient	ξ^{MeOH}	$2.5X^{MeOH}$	[14]
Partition coefficient	K_I	0.8	[13]
Partition coefficient	K_{II}	0.8	[13]

3. Performance Evaluation

To obtain the polarization curve the cell voltage of DMFC can be written as,

$$V_{cell} = U^{O_2} - U^{MeOH} - \eta_A - \eta_C - \frac{\delta_{MEM} I_{Cell}}{\kappa} \quad (21)$$

The over potentials term η_A and η_C can be determined from the Tafel equations,

$$I_{Cell} = I_{0,ref}^{MeOH} \frac{C_{AC}^{MeOH}}{C_{MeOH,ref}} e^{\alpha_A \eta_{AF}/RT} = I_{0,ref}^{O_2} \frac{C_{O_2}}{C_{O_2,ref}} e^{\alpha_C \eta_{CF}/RT} - I_{leak} \quad (22)$$

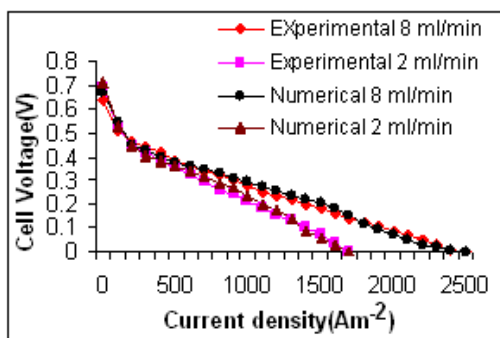
I_{leak} is the leakage current density due to the oxidation of the methanol crossover.

$$\frac{I_{leak}}{6F} = N_{Crossover}^{MeOH} = (-D_M^{MeOH} \frac{dC_M^{MeOH}}{dx} + \xi^{MeOH} \frac{I_{cell}}{F}) \quad (23)$$

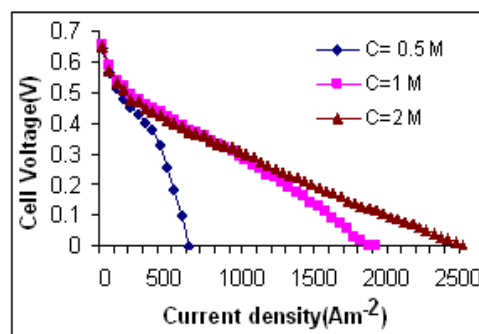
4. Results

4.1. Effect of mass flow rate and inlet feed concentration on the cell performance

The model has been validated by comparison of the results from SSFF configuration with its experimental data from Q. Liao and X. Zhu [10]. The cell performance have been calculated for the methanol inlet feed concentration of $M=1$, temperature of 60°C and two different inlet mass flow rate. As it can be seen the model results are in the good agreement with the experimental data. In the right figure the variation of cell voltage with the current density at different inlet feed concentrations have been shown and it is obvious that the cell performance will improve while the inlet feed concentration increase. The performance improvement from 1M to 2M is more than from 0.5M to 1M. This can be attributed to increasing methanol concentration, which satisfies the additional requirement of the electrochemical reaction in the anode due to higher current densities.



(6.a)



(6.b)

Fig. 6. Numerical and experimental cell data performance for two different inlet mass flow rate (6.a) and Cell performance at different inlet feed concentration (6.b)

4.2. Effect of flow configuration on CO₂ and methanol concentration

Distribution of CO₂ molar concentration in the anode channel for different configurations at the inlet feed concentration and current density 2M, 1500A/m² respectively, have been shown in fig7. CO₂ molar concentration increase incrementally from inlet to outlet and reach the maximum value 0.03 , 0.025 and .02 for PFF, SFF and MSFF respectively. Fig8 shows the distribution of methanol molar concentration. Here the methanol concentration decreases incrementally from inlet to outlet and reaches the minimum value of 0.5, 0.71 and 0.81 for PFF, SFF and MSFF respectively in the outlet of the channel. The distribution of the CO₂ in

the MSFF is more smoothly relative to two other cases and the coalescence of gas bubbles in the corner of the ribs are less than other cases.

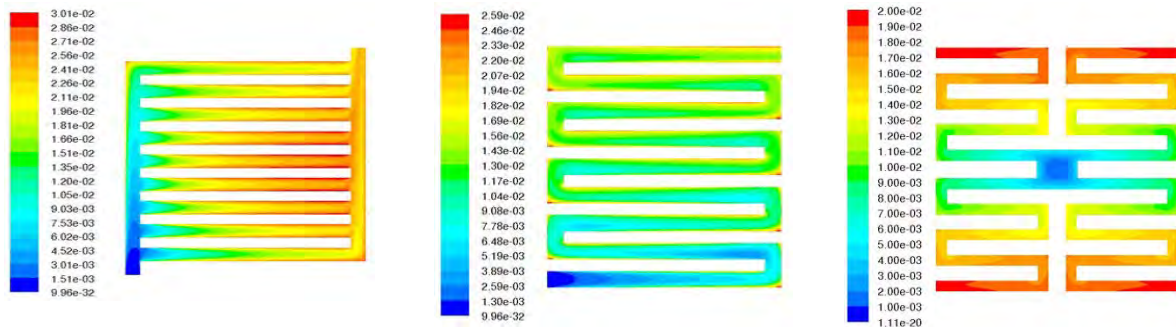


Fig. 7. Distribution of CO₂ molar concentration for PFF, SFF and MSFF flow configuration

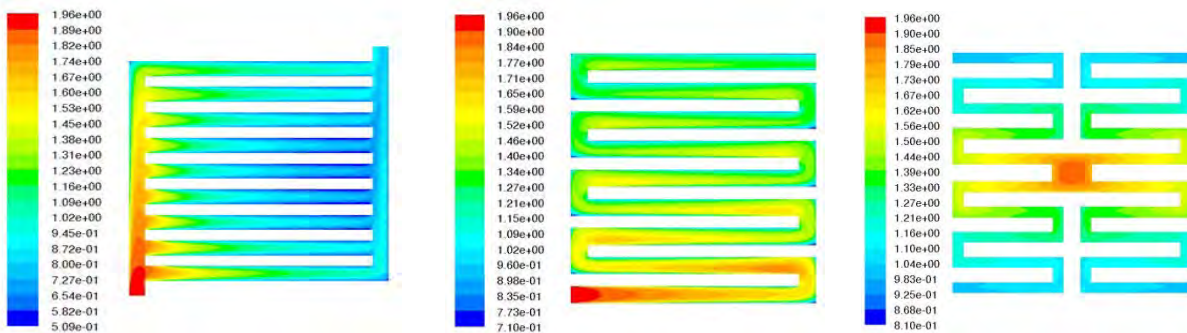


Fig. 8. Distribution of MeOH molar concentration for PFF, SFF and MSFF flow configuration

4.3. Effect of flow configuration and temperature on the cell performance

The performance of the cell is depended on the mass fraction of methanol in the catalyst layer that is depended on the average methanol mass fraction in the anode channel. By calculation the cell performance using mentioned combination method, it can be seen that the MSFF configuration has better performance relative two other cases fig9a. In the right picture9.b the effects of temperature on cell performance have been shown. As it can be seen with increasing the temperature the cell performance will increase, especially at high current density.

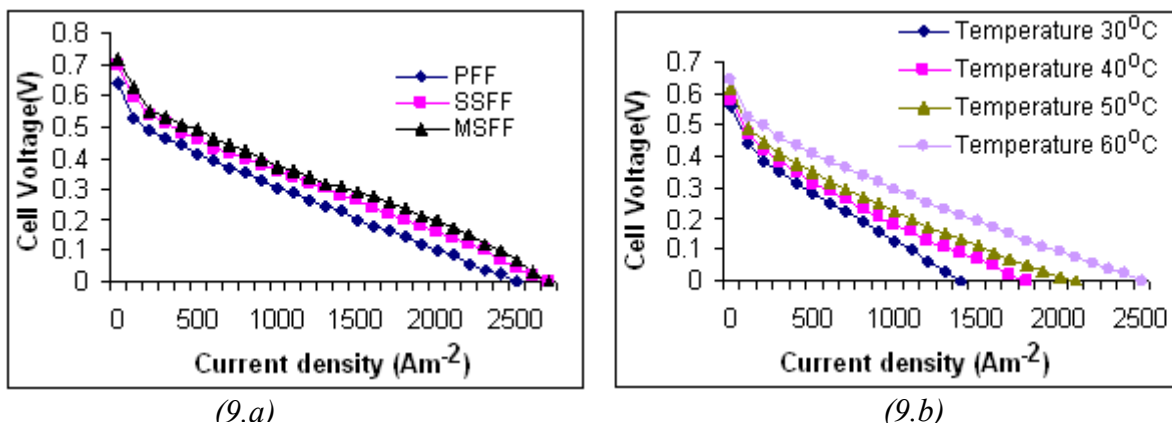


Fig. 9. Comparison of anode configuration on cell voltage (9.a) and effects of temperature on cell performance (9.b)

5. Conclusions

DMFCs have the following advantages; easy fuel delivery and storage, no need for cooling or humidification, simpler system design and may even achieve higher overall energy efficiency than PEMFCs with further developments. This new modeling design is the way to find the exact cell performance with different geometry. From the results, MSFF flow configuration can give a better performance relative to two other cases so this kind of cell geometry can solve the problems regarding lower overall energy efficiency of DMFCs relative to PEMFCs.

References

- [1] C.K. Dyer, Fuel Cells for Portable Applications, *J. Power Sources* 106 (2002) 31–34.
- [2] K. Cowey, K.J. Green, G.O. Mepsted and R. Reeve, Portable and military fuel cells, *Curr. Opin. Solid State Mater. Sci.* 8 (2004) 367–371.
- [3] A. Kulikovskiy, J. Divisek and A.A. Kornyshev, Two-dimensional simulation of direct methanol fuel cells, a new type of current collector, *J. Electrochem. Soc.* 147 (2000) 953.
- [4] Z.H. Wang and C.Y. Wang, Mathematical modeling of liquid-feed direct methanol fuel cells, *J. Electrochem. Soc.* 150 (4) (2003) 508–519.
- [5] Z.H. Wang, C.Y. Wang and K.S. Chen, Two-phase flow and transport in the air cathode of proton exchange membrane fuel cells, *J. Power Sources* 94 (2001) 40–50.
- [6] K.A. Triplett, S.M. Ghiaasiaan, S.I. Abdel-Khalik, A. LeMouel and B.N. Mc-Cord, Gas-liquid two-phase flow in microchannels, Part II, *Int. J. Multiphase Flow* 25 (1999) 395.
- [7] T. Fukano and A. Kariyasaki, Characteristics of gas-liquid two-phase flow in a capillary tube, *Nucl. Engng. Des* 141 (1993) 59.
- [8] H.S. Isbin, R.H. Moen, R.O. Wickey, D.R. Mosher and H.C. Larson, Two-phase Steam Water Pressure Drops, Nuclear Science and Engineering, Conference, Chicago, 1958
- [9] G.L. Brenda, A.S. Vijay, J.W. Weidner and R. E. White, Mathematical Model of a Direct Methanol Fuel Cell *Journal of Fuel Cell Science and Technology* Nov, 2004, Vol. 1 /Pp 43-48
- [10] L. Qiang, Z. Xun, Z. Xueyan and D. Yudong, Visualization study on the dynamics of CO₂ bubbles in anode channels and performance of a DMFC, *Journal of Power Sources* 171 (2007) 644–651
- [11] A. A. Kulikovskiy, J. Divisek, and A. A. Kornyshev, Two-Dimensional Simulation of Direct Methanol Fuel Cell A New (Embedded) Type of Current Collector, *Journal of the Electrochemical Society*, 147 (3) 953-959 (2000)
- [12] K. Scott, W. Taama and J. Cruickshank, Performance and Modeling of a Direct Methanol Solid Polymer Electrolyte Fuel Cell, *J. Power Sources* 65(1-2), 1997, pp. 159-171.
- [13] S.F. Baxter, V.S. Battaglia and R.E. White, Methanol Fuel Cell Model: Anode, *Journal of the Electrochem Society*, 1999, 146(2), pp. 437-447.
- [14] X. M. Ren, T. E. Springer, T.A. Zawodzinski and S. Gottesfeld, Methanol Transport through Nafion Membranes, *J. Electrochem Society*, 2000. 147(2), pp. 466-474.
- [15] A. Parthasarathy, S. Srinivasan, A.J. Appleby and C. R. Martin, Temperature Dependence of the Electrode Kinetics of Oxygen Reduction at the Platinum/Nafion Interface, a Microelectrode Investigation, *J. Electrochem Society*, 1992, 139(9), pp. 2530-2537.

Investigation of electrical, structural and thermal stability properties of cubic $(\text{Bi}_2\text{O}_3)_{1-x-y}(\text{Dy}_2\text{O}_3)_x(\text{Ho}_2\text{O}_3)_y$ ternary system

Refik Kayali^{1,*}, Murivet Kasikci¹, Semra Durmus², Mehmet Ari²

¹Department of Physics, Science-Literature Faculty, Nigde University, Nigde, Turkey

²Department of Physics, Science-Literature Faculty, Erciyes University, Kayseri, Turkey

* Corresponding author. Tel: +90 388 225 4069, Fax: +90 388 225 0180, E-mail: refikkayali@nigde.edu.tr

Abstract: In the scope of this work, $(\text{Bi}_2\text{O}_3)_{1-x-y}(\text{Dy}_2\text{O}_3)_x(\text{Ho}_2\text{O}_3)_y$ ternary system ($x=1,3,5,7,9,11$ mol % and $y=11,9,7,5,3,1$ mol %, dopant concentrations) sample materials were developed using solid state reaction method sintering each of them at 650, 700, 750, 800 °C for 48 hours. Structural, electrical and thermal properties of these samples which are candidate of electrolyte for solid oxide fuel cells (SOFCs) have been evaluated by means of XRD, four-probe method, and TGA / DTA. XRD measurements showed that except the samples annealed at 650 °C, all the other samples have stabilized δ - Bi_2O_3 phase. It was seen that duration of sintering time and temperature was rather effective on the formation of the stabilized sample materials and their other properties, such as electrical and structural properties. It was seen that the electrical conductivities of all the examples developed sintering at 700, 750 and 800 °C for 48 hours increases with the increasing temperature having numerical values varying in the range of $7,65 \times 10^{-2} \Omega \cdot \text{cm}^{-1}$ - $6,11 \times 10^{-1} \Omega \cdot \text{cm}^{-1}$. Activation energy of the sample A6 was calculated and it was found 0.97 eV. On the other hand, the main purpose of this study is to find an electrolyte which does not have any degradation in its properties with time; this maybe caused either interaction between the different electrochemical cell materials or by instability of the ionic conductor under operation conditions. During the heating/cooling process, the four-point probe conductivity measurements have been performed. The hysteresis curve was obtained for this sample due to time interval difference of heating/cooling processes. It was observed that there is no gradation in the structure of the sample.

Keywords: Electrolyte, Solid state reaction, Fuel cell, Electrical conductivity, XRD, Four- probe point method

1. Introduction

Recently, it has been known that bismuth oxide based and doped with the other two ceramic oxides are ternary materials with the properties showing promise of utility in SOFC's [1-7]. In addition, the need to develop oxide ion conductive materials with high conductivity and desired structure stability at low temperature directs most of the research toward solid oxide electrolyte materials. Among these electrolyte materials, Bi_2O_3 - based solid oxide electrolyte materials with δ -phase fcc fluorite type crystal structure are of interest for use in solid oxide fuel cell (SOFC) due to their high oxide ion conductivity [8,9]. The fluorite type phase of pure Bi_2O_3 , known as the most highly conductive oxide-ion conductor, has a conductivity of about 1 Scm^{-1} at 750 °C. But, δ -phase Bi_2O_3 is stable only between 730 °C and 825 °C and cannot be quenched to room temperature [10]. However, the δ -phase can be obtained at room temperature by doping with some transition metal (Nb, Ta, V and W) and rare earth (Sm-Lu). It is also possible to use combination of oxides, so called double doping, to obtain the δ fluorite type phase. Fluorite type δ -phase materials displays very high oxide ion conductivity which is attributed to the highly polarisable Bi^{3+} cations and highly disordered structure of sublattice [11-15]. Structural and conductive properties of a solid material during the various temperature ranges determine its suitability as an electrolyte in the practical use. If an electrolyte material has a high conductive behavior over a long period of time at reasonably low temperature, it is possible to use at operation of a SOFC. Many researchers were reported that the fluorite type δ -phase Bi_2O_3 cannot be stabilized [11-13]. Some these kinds of materials had completely transformed into mixture phases after annealing for long time period. In addition, the conductivity decay can also occur for the fluorite type materials without changing its structure. The rate of conductivity decay is dependent on annealing temperature, long ordering oxide-ion sublattice and amount of doped cations.

2. Experimental

2.1. Sample preparation

We have tried to stabilize the fluorite type δ -phase in the ternary system $(\text{Bi}_2\text{O}_3)_{1-x-y}(\text{Dy}_2\text{O}_3)_x(\text{Ho}_2\text{O}_3)_y$. As a result, we could obtain a stabilized δ -phase in limited compositional range of x and y .

The desired proportions of the samples were accurately weighed and thoroughly mixed. The mixture was heated in an alumina crucible at 750 °C for 10 h and quenched to room temperature by air stream. Next, the samples were examined by XRD using $\text{CuK}\alpha$ radiation. Then, the prepared pellets were annealed at 650, 700, 750 and 800 °C for 48 h followed by air quenching. The same heat treatment was repeated several times in order to get its equilibrium state, after the conductivity measurements were performed in air. Finally, thermal behavior of the samples was taken the differential thermal analysis (DTA) measurements in order to find out whether any phase transition exists or not, after each measurement.

2.2. XRD measurements

Powder XRD measurements is carried out by using Bruker AXS D8 Advance type diffractometer with an interval $2\Theta = 10^\circ\text{--}90^\circ$, scanning $0,002^\circ/\text{min}$, and $\text{Cu-K}\alpha$ radiation for the determination of the crystal structure of the samples at room temperature. These measurements were repeated for the powders of the samples obtained after every sintering process. Then, Diffrac Plus Eva packet program was used to analyze the unit lattice cell parameters (a , b , c , α , β , γ), Miller indexes, and the distance between the layers, d . On the other hand, Win-Index Professional Powder Indexing packet program was used for the indexing of the diffraction peaks in the powder patterns of the samples.

2.3. Electrical measurements

Conductivity of the samples was measured using four-point probe method. The pellets of the samples with 13 mm diameter and 2 mm thick were obtained by using a conventional press and then the pellets were being air-quenched after sintering. All of the measurements in this work were carried out by means of Data Acquisition Control System associated with a PC, interface card IEEE-488.2, multimeter with scanning card (Keithley 2700, 7700-2), programmable power supply (Keithley 2400), and computer program written for this purpose. These measurements were repeated for several times because of the electrical conductivity measurements performed during the first heating process are not enough to represent the complete electrical behavior of the samples.

2.4. TG/DTA measurements

The thermal behavior of the annealed materials was investigated by DTA/TG by means of DIAMOND TG/DTA-PERKIN ALMER Marck system. The samples whose masses are about 20-50 mg were heated at $200^\circ\text{C min}^{-1}$ in an alumina crucible and cooled quickly to room temperature under a stream of air.

3. Results and discussion

3.1. XRD measurement results

Figure 1 shows the comparisons of the XRD spectra of the samples annealed at 650 °C for 48 hours. As seen from this figure, all the samples do not have completely monoclinic- α phase, but some of them have also δ -phase. As a result, the samples prepared at this temperature have a mixed phase and the formation of the δ -phase also exhibits at this stage.

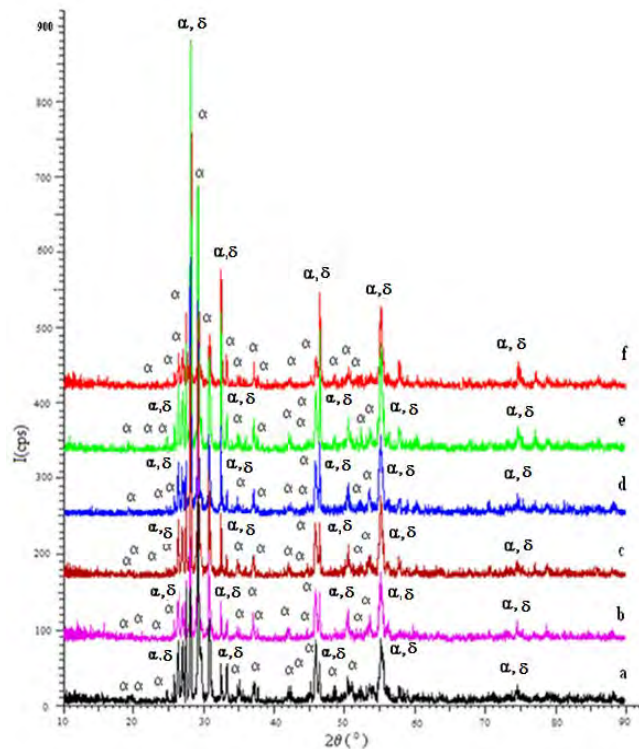


Fig.1. Comparisons of the XRD spectra of the samples annealed at 650 °C and for 48 hours and having $\alpha+\delta$ - Bi_2O_3 phase (a) A1, (b) A2, (c) A3, (d) A4, (e) A5 and (f) A6

Figure 2 shows the comparisons of the XRD spectra of the samples annealed at 750 °C for 48 hours. From this figure, it is observed that all the samples except A1 have only δ -phase. Two peaks at the right and left side of the most intensive peak of the sample A1 are seen and they are belonging to the α -phase. No significant modification of the intensity of the XRD pattern can be detected, which means that the δ -phase of the samples has not been decomposed into the other low conductivity phases by changing amount of the doped materials.

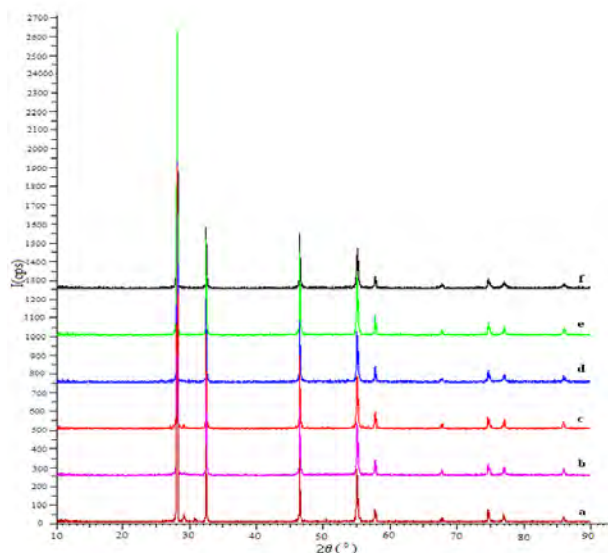


Fig. 2. Comparisons of the XRD spectra of the samples annealed at 750 °C and for 48 hours and having fcc δ - Bi_2O_3 phase (a) A1, (b) A2, (c) A3, (d) A4, (e) A5 ve (f) A6

Also, there is no transformation of the quenched δ -phase is evidenced on the XRD patterns. The fluorite type δ -phase is obtained at the end of the process. The first generated δ -phase has

been kept stable during the electrical measurement annealed at 700, 750, 800 °C for all the samples.

Summary of the observed phases from XRD measurements of the $(\text{Bi}_2\text{O}_3)_{1-x-y}(\text{Ho}_2\text{O}_3)_x(\text{Dy}_2\text{O}_3)_y$ ternary-systems with different dopant ratios and developed at different temperatures mentioned above is given in Table 1. As seen from this table, all the samples except the samples annealed at 650 °C have stable fcc δ -phase.

Table 1. Observed phases for $(\text{Bi}_2\text{O}_3)_{1-x-y}(\text{Ho}_2\text{O}_3)_x(\text{Dy}_2\text{O}_3)_y$ ternary-systems with different dopant ratios and developed at different temperatures

Synthesing temperature (°C)	Synthesing time (hour)	$(\text{Ho}_2\text{O}_3)_x(\text{Dy}_2\text{O}_3)_y(\text{Bi}_2\text{O}_3)_{1-x-y}$ ($x,y = \text{mol } \%$)					
		x=1 y=11	x=3 y=9	x=5 y=7	x=7 y=5	x=9 y=3	x=11 y=1
650	48	$\alpha + \delta$	$\alpha + \delta$	$\alpha + \delta$	$\alpha + \delta$	$\alpha + \delta$	$\alpha + \delta$
700	48	δ	δ	δ	δ	δ	Δ
750	48	δ	δ	δ	δ	δ	Δ
800	48	δ	δ	δ	δ	δ	Δ

3.2. Electrical conductivity measurements

The conductivity measurements were performed on the samples $(\text{Bi}_2\text{O}_3)_{1-x-y}(\text{Dy}_2\text{O}_3)_x(\text{Ho}_2\text{O}_3)_y$ ternary system ($x=1,3,5,7,9,11$ mol % and $y=11,9,7,5,3,1$ mol %). Conductivity measurements were only carried out up to 850 °C in order to ensure that melting does not occur. In this report, we have presented only the electrical measurements of the samples developed at 750 °C, since it has the best conductivity. The conductivity of this sample is $0.6 (\Omega \cdot \text{cm})^{-1}$ placing it among the most highly conductive materials known.

Figure 3 shows the graphics of the conductivity of the samples versus to $1000/T$ K. As seen from this figure, all the curves are similar with each other. It is the expected result since all of them have stable fcc δ -phase. These results were supported by the XRD patterns of the samples which have been given in Fig.3 too.

The Ho_2O_3 rich samples show higher electrical conductivity than the Dy_2O_3 rich materials. The conductivity results show that an intermediate fast changing conductivity region separated by linear evolution zone. The sharp rise of the conductivity is indication of an order-disorder transition.

Increase in the conductivity of the materials with increasing amount of Ho_2O_3 is attributed to the increase in the proportion of highly polarisable cations and in the number of oxide ion vacancies. It can be noticed that the conductivity slightly increases with increasing the Ho_2O_3 proportion, reaching highest values $0.6 (\Omega \cdot \text{cm})^{-1}$ for $x=11$ an $y=1$ %mol (A6). This can simply be explained that can be attributed to the increase in the concentration of vacancies by the Ho cations located on the host sub-lattice, which are available for oxide ion migration. The distribution of vacancies affects the long range migration of oxide ions and therefore the conductivity increases. Since dopant cations and oxide ion vacancies have negative and positive charges, attractions between them are likely to be mainly responsible for the high activation energy. As a result, it can be said that an electrical conductivity rise has been observed for all samples when the proportion of the Ho^{3+} cation is increased.

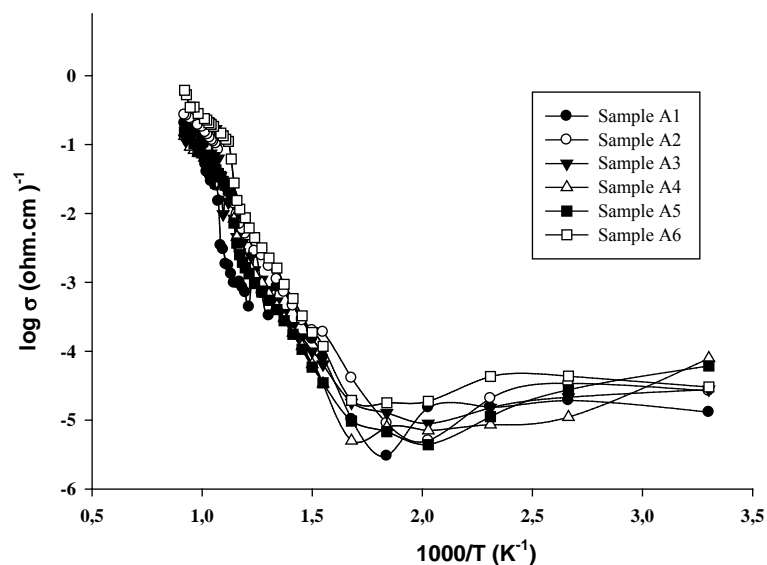


Fig. 3. Oxygen conductivity, as a function of temperature, for the samples A1, A2, A3, A4, A5, A6 obtained at 750 °C for 48 hours

Figure 4 shows the graphic of the conductivity of the sample A6 versus to 1000/T K at different annealing temperatures. As seen from this figure, two distinct regions observed on the curves corresponding to an order-disorder δ -phase transition which exhibits similar activation energy at these two regions. The characteristics of the conductivity curves are similar for all the samples. The conductivity values slightly increase with decreasing the annealing temperature especially at high temperature region.

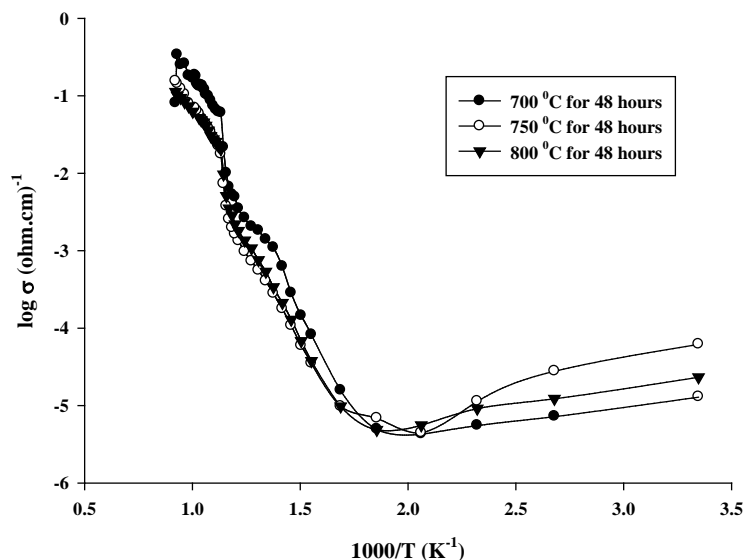


Fig. 4. Oxygen conductivity, as a function of temperature, for the sample A6

Activation energies of the samples can be obtained from the Arrhenius equation. As mentioned previously two distinct regions are observed for all samples corresponding to an order-disorder δ -phase transition which exhibits similar activation energy at these two regions. Activation energy calculated for sample A6 corresponding to the high temperature region is found 0.97 eV. And also, the conductivity results are in good agreement with these

already revealed by XRD and DTA/TG measurements. The samples which exhibit the lowest activation energy is associated the structure characterized by the fluorite type fcc lattice is likely responsible for opening of migration pathways for the oxide ions, and consequently to a decreasing of the activation energy.

The main purpose of this study is to find an electrolyte which does not have any degradation in its properties with time; this maybe caused either interaction between different electrochemical cell materials or by instability of the ionic conductor under operation conditions. So this sample has been firstly heated from room temperature to 650, 700, 750 and 800 °C in 48 hours and cooled from this temperature to room temperature in the same time. After this process, the four-point probe conductivity measurements have been performed.

Figure 5 shows the hysteresis curve obtained for the sample A6. This sample has been firstly heated from room temperature to 800 °C in 2 hours and cooled from this temperature to room temperature within the 4 hour s. During this process, the four-point probe conductivity measurements have been performed. The hysteresis curve was occurred for this sample due to time interval difference of heating/cooling processes. From this figure, the slopes of these curves nearly are the same. It means that there is no gradation in the physical and chemical properties of this sample after applying the operation condition.

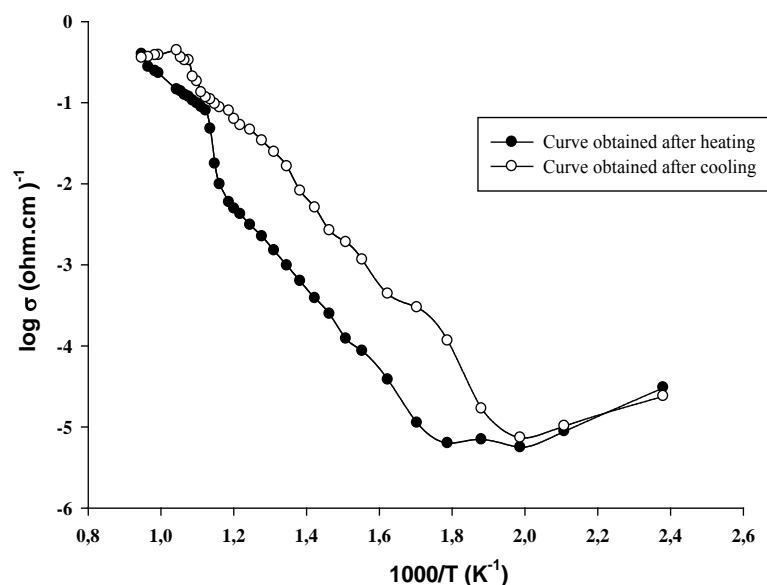


Fig. 5. Conductivity hysteresis curve obtained for the sample A6 obtained approximately 5 hours being heated from room temperature to 800 °C and cooled to room temperature

TG/DTA measurements of the samples have been carried out after the conductivity measurements of the samples using the same pellets. In figure 6, TG/DTA graphics of the sample A6 annealed at 750 °C and for 48 hours are given. From this figure, a wide range of exothermic peak is seen in a temperature range between 325-415 °C for A6 sample in DTA curve. Similar variation is seen between the same temperature ranges in TGA curve whose slope is changing during heating treatment. In this case, this peak results from the order/disorder transformation in the structure of the sample rather than the phase transformation. During the cooling process, there are no exothermic peak and slope changes because of long cooling time interval. This transformation is seen in the conductivity graphics of the same sample and its hysteresis curve (Fig. 5) too.

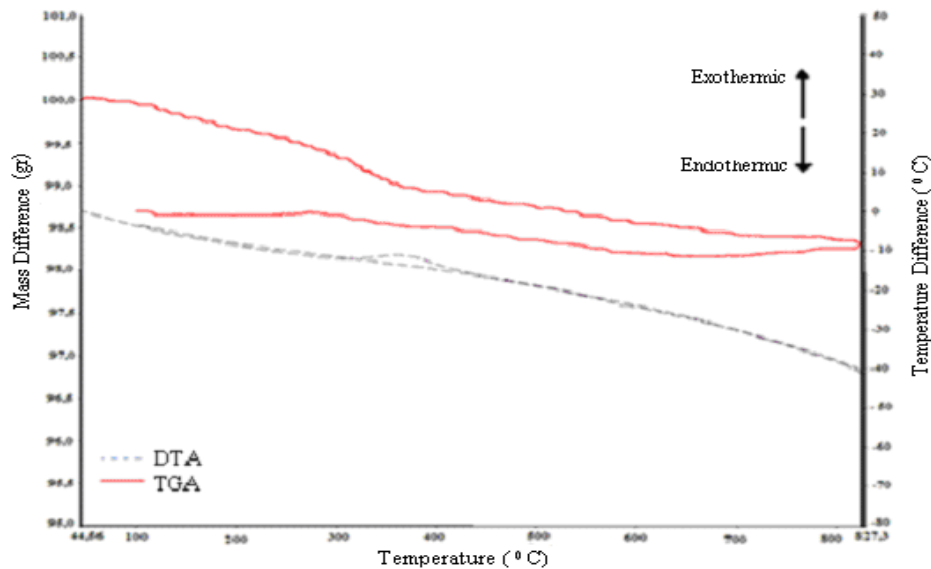


Fig. 6. TG/DTA graphics of sample A6 developed at 750 °C and for 48 hours

4. Conclusion

In this work, data obtained from XRD, DTA, TGA and four probe point method measurements for $(\text{Bi}_2\text{O}_3)_{1-x-y}(\text{Ho}_2\text{O}_3)_x(\text{Dy}_2\text{O}_3)_y$ ($x=1, 3, 5, 7, 9, 11$ mol%, $y=11, 9, 7, 5, 3, 1$ mol %) ternary system samples synthesized at different temperatures by solid state reaction method has been investigated in detail and some important results have been obtained for the chosen sample A6 as following:

- According to the obtained XRD results, all the samples synthesized at 700 °C, 750 °C and 800 °C for 48 hours have dominantly homogeneous face centered cubic $\delta\text{-Bi}_2\text{O}_3$ phase. The samples annealed at 650 °C have mixed phases composed from monoclinic $\alpha\text{-Bi}_2\text{O}_3$ phase and fcc $\delta\text{-Bi}_2\text{O}_3$ phase.
- According to conductivity measurements, all the samples, having stable $\delta\text{-Bi}_2\text{O}_3$ phase and synthesized at 700 °C, 750 °C, and 800 °C for 48 hours, have a good oxygen ion conductivity property.
- It has been observed that the electrical conductivity of all the samples increases while the percentage of the Ho_2O_3 doping materials increases.
- The best electrical conductivity has been observed for the sample A6 synthesized at 750 °C for 48 hours and having doping ratios % 11 mol for Ho_2O_3 and % 1 mol for Dy_2O_3 and maximum conductivity value has been measured as $6.11 \times 10^{-1} (\Omega \cdot \text{cm})^{-1}$.
- Stable δ -phase of $(\text{Bi}_2\text{O}_3)_{1-x-y}(\text{Ho}_2\text{O}_3)_x(\text{Dy}_2\text{O}_3)_y$ ternary system has been observed firstly in this study in operation conditions of an SOFC.

Comment

We are planning to perform resistance tests for this material for long time periods under the operation conditions to show that this material can be used as an electrolyte in SOFCs.

References

- [1] D. Music, S. Konstantinidis and J. M. Schneider, Equilibrium structure of $\delta\text{-Bi}_2\text{O}_3$ from first principle, *J. Phys.: Condens. Matter*, 21, 2009, 175403-175480.

- [2] C. -Y. Hsieh, K.-Z. Fung, Crystal structure and electrical conductivity of cubic fluorite-based $(\text{YO}_{1.5})_x(\text{WO}_3)_{0.15}(\text{BiO}_{1.5})_{0.85-x}$ ($0 \leq x \leq 0.4$) solid solutions, *J. Solid State Electrochem*, 13, 2009, 951-957.
- [3] P.K. Cheekatamarla, M. F. Caine, and J. Cai, Internal reforming of hydrocarbon fuels in tubular solid oxide fuel cells, *International Journal of Hydrogen Energy*, 33, 2008, 1853-1858.
- [4] S.R Xiao-Feng Ye, Z.R Wang, L. Wang, X.F Xiong, T.L. Sun Wen, Use of a catalyst layer for anode-supported SOFCs running on ethanol fuel, *Journal of Power Sources*, 177, 2008, 419-425.
- [5] M. Wang, and K. Woo, Impact of Sr_2MnO_4 preparation process on its electrical resistivity, *Energy Conversion and Management*, 49, 2008, 2409–2412.
- [6] S.H. Jung, E.D. Wachsman and N. Jiang, Structural Stability and Conductivity of Cubic $(\text{WO}_3)_x-(\text{Dy}_2\text{O}_3)_y-(\text{Bi}_2\text{O}_3)_{1-x-y}$, *International Journal of Ionics*, Volume 8, Numbers 3-4, 2002, 210-214.
- [7] M. Benkaddour, M.C. Steil, M. Drache, and P. Conflant, The Influence of Particle Size on Sintering and Conductivity of $\text{Bi}_{0.85}\text{Pr}_{0.105}\text{V}_{0.045}\text{O}_{1.545}$ Ceramics, *Journal of Solid State Chemistry*, 155, 2000, 273-279 .
- [8] N.M. Sammes, G.A. Tompsett, H. Nafe and F. Aldinger, Bismuth based oxide electrolytes structure and ionic conductivity, *Journal of European Ceramic Society*, 19, 1999, 1801-1826.
- [9] N. Jiang, E.D. Wachsman and S.H. Jung, A higher conductivity Bi_2O_3 -based electrolyte, *Solid State ionics*, 150, 3-4, 2002, 347-353.
- [10] H.A. Harwing, On the Structure of Bismuthsesquioxide: The α , β , γ , and δ -phase, *Z. Anorg. Allg. Chem.*, 444, 1978, 151-166.
- [11] A. Watanabe, Is it possible to stabilize $\delta\text{-Bi}_2\text{O}_3$ by an oxide additive?, *Solid State Ionics*, 40-41, 1990, 889-892 .
- [12] N. Jiang, R.M. Buchanan, F.E.G. Henn. A.F. Marshall, D.A. Stevenson, E.E. Wachsman, Aging phenomenon of stabilized bismuth oxides, *Mater. Res. Bull.*, 29, 1994, 247-254.
- [13] E.D. Wachsman, S. Boyapati, M.J. Kaufman, N. Jiang, Modeling of Ordered Structures of Phase-Stabilized Cubic Bismuth Oxides, *J. Am. Ceram. Soc.*, 83, 2000, 1964-1968.
- [14] E.D. Wachsman, G.R. Ball, N. Jiang and D.A. Stevenson, Structural and defect studies in solid oxide electrolytes, *Solid State Ionics*, 52, 1992, 213-218.
- [15] S. Boyabati, E.D. Wachsman and B.C. Chakoumakos, Neutron diffraction study of occupancy and positional oxygen ions in phase-stabilized cubic bismuth oxides, *Solid state Ionics*, 138, 2001, 293-304.

Alkaline Fuel Cell (AFC) engineering design, modeling and simulation for UPS provide in laboratory application

L. Ariyanfar^{1,*}, H. Ghadamian², R. Roshandel³

^{1,2}. Department of Energy Engineering, Science and Research Campus, Islamic Azad University, Tehran, IRAN

³. Energy Engineering Department, Sharif University of Technology, Tehran, IRAN

* Corresponding author. Tel: +98 21 44240042, Fax: +98 21 44232205, E-mail: Leyliariyan@gmail.com

Abstract: In the presented research, a feasibility study to cover a mobile electrolyte alkaline fuel cell behaviors and characteristics (which the electrolyte has system cooling role) for UPS (Uninterruptable Power Supply) application is provided to use in an energy laboratory. Electrochemical modeling and computations for irreversibilities led to optimization of cell voltage, current & power densities and the results are found to be 0.566V, 574.3 mA/cm², 325.2 mW/cm² respectively. By using mentioned quantities, ideal thermodynamic efficiency, real thermodynamic efficiency and electrical efficiency concluded 80%, 38% and 34% respectively. Preliminary electrochemical studies in this research are combined with engineering designs in complementary stage of research. At the next stage, considerations on heat and mass transfer and contributed models lead to approve a double pipe heat exchanger as energy sink. Then the cost model is also determined and the optimization codes are developed to propose best operation point of system with minimizing total cost and determining the heat exchanger dimensions, flow rates and temperatures. Furthermore, parametric analysis for variation of temperature, electrolyte cooling rate and cost of planned AFC has been studied for energy efficiency and performance improvement.

Keywords: Alkaline Fuel Cell (AFC), Irreversibilities, Heat Transfer, Cost Model, Parametric Analysis.

1. Introduction

Fuel cell is an electrochemical system that converts energy of the chemical reaction to useful electrical energy and is made of anode, cathode and electrolyte. Fuel cells classified according to practical temperature, type of electrolyte and constitutive materials; and alkaline fuel cells or AFCs are one of low temperature systems with an alkaline solution as the electrolyte. Alkaline fuel cell is the oldest type of fuel cells, which had described in 1902 and have used in spatial applications [1]. AFC produce electricity through oxidation - reduction reactions between oxygen and hydrogen. In the fuel cell reaction water is generated, and two electrons are released. The electrons flow through an external circuit, and have returned to the cathode to reduce oxygen in an electrochemical reaction and thus hydroxide ions are produced. Electricity and heat are made as byproducts of this product [2]. This system usually has peripheral equipment. Wide studies have done about alkaline fuel cells; but what had not enough attention is specialty study with practical and all purpose approach. Although the central system produce the power, but peripheral equipment also use and effect on whole system performance and the total cost. In this research has been trying to design system and accessories in the optimal mode of increasing efficiency and reducing costs are assessed.

2. System configuration

An energy laboratory is designed, which part of its power provide from fuel cell systems with ancillary performance and specific aims. Several different objects in correlation with together are contemplated in this laboratory that each has its survey. The typical plan of laboratory is shown in Fig.1. As seen a 100W AFC has chosen for UPS provider of this laboratory. In these cells the electrolyte is alkaline solution and how to use of is an issue. It can be in mobile electrolyte, static electrolyte and dissolved fuel alkaline fuel cells modes [1]. What are discussed in this research are electrochemistry calculations, engineering design and heat transfer of an alkaline fuel cell system with system optimization aim.

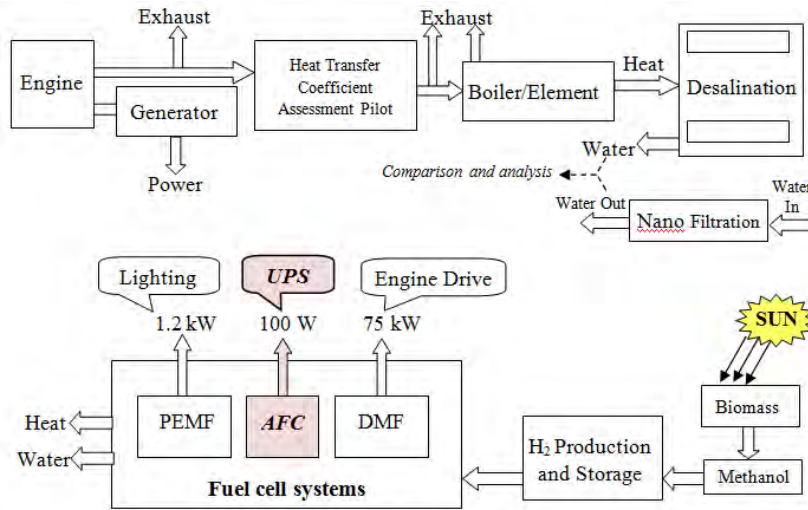


Fig. 1. Designed Energy Laboratory

Fig. 1. Designed Energy Laboratory

The basic structure design for mobile electrolyte AFC system [3] is shown in Fig.2.

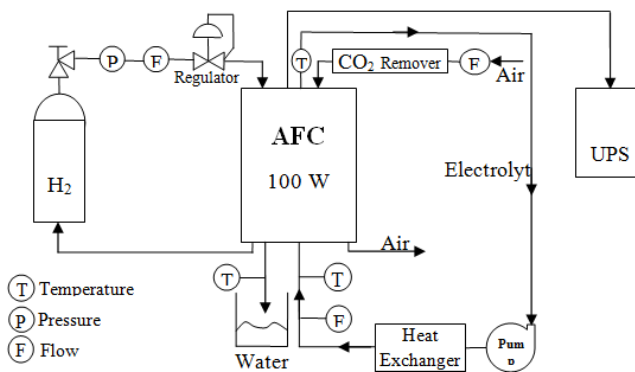


Fig. 2. Alkaline fuel cells with mobile electrolyte system and peripheral equipments

Procedures in this type of systems is so that the electrolyte flow between the anode and cathode plates in addition ion transfer and electric current; with its circulation led the excess heat of system to the outside and before re-entry into the system shall pass within a heat exchanger for cooling. Electrolyte needs pumping system us to held circulating [1].

2.1. Electrochemistry

According to voltage losses [4] in a fuel cell system, optimum current is achieved so that losses would be minimum, and thus optimal power and voltage are obtained [5,6]. Types of efficiencies that are considered in this system are ideal and actual thermodynamic efficiency and electrical efficiency that can be helpful to evaluation of system.

2.2. Engineering design

Hydrogen and air consumption, and water, electricity and heat production flow rates are calculated. A fuel cell stack consists of many separate cells. Design of stack and cells arrangement (after obtain the whole required surface) can has different modes. According to the desired power, energy demand and circumstances can decide regarding choice of optimized mode.

2.3. Heat Transfer

In mobile electrolyte systems, the cooling process is done by electrolyte. So according to the rate of heat production in electrochemical reactions and selected materials [7,8], electrolyte flow rate can set somehow that eject the waste heat from system and kept system performance in ideal temperature [9,10]. Overall fuel cell system heat transfer can be done through conduction, convection and radiation. Since the alkaline fuel cell systems have low operation temperature, radiant heat transfer can be waived [11].

3. System Modeling

To begin calculations, considering series of assumptions and initial conditions are necessary [12]. The system is considered to produce 100 watt in atmospheric pressure. It is assumed that produced water is in liquid form. Electrochemistry relations have scrutinized with optimization voltage and current using GAMS software. The optimum solution determined efficiency values and input and output flow rates. According to the steps of stack and cells arrangement [13], algorithm of Fig.3 can be used in modicum number studies.

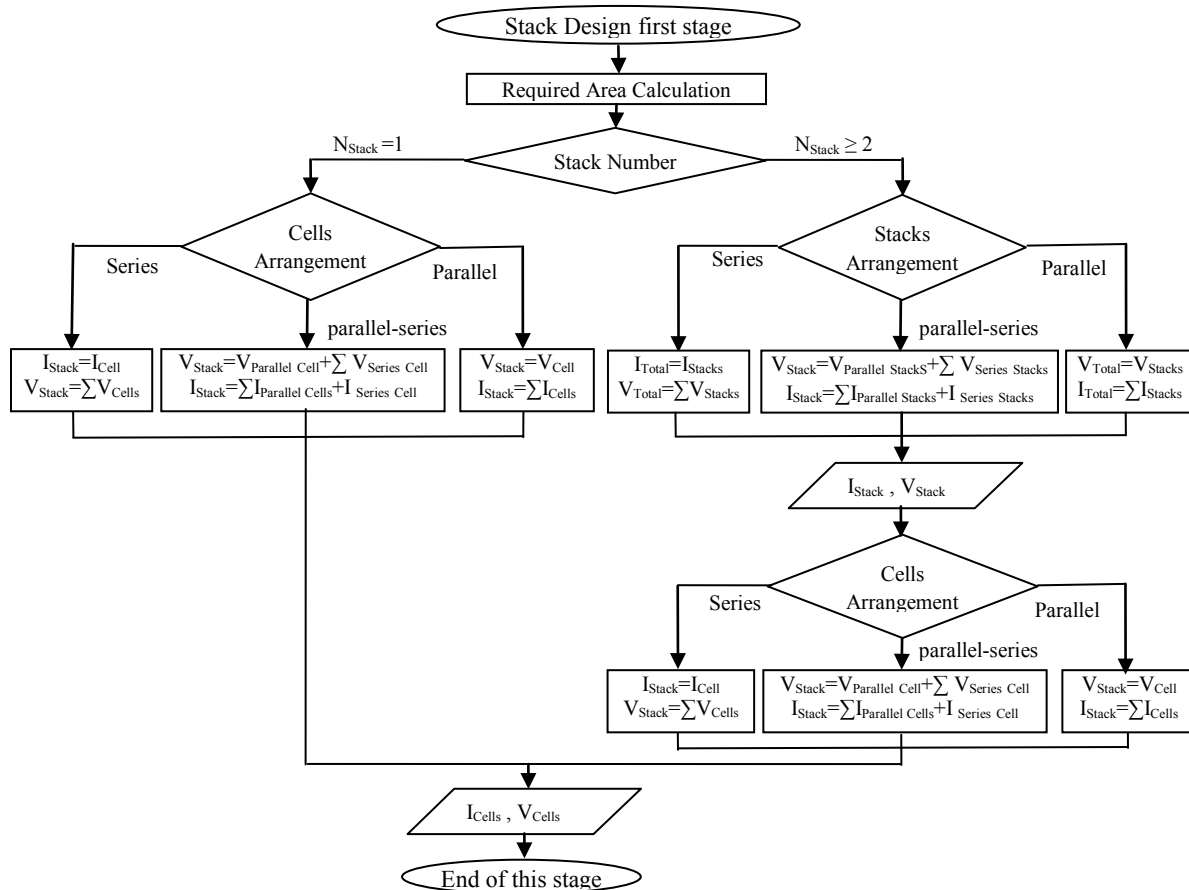


Fig. 3. Stack design algorithm

To evaluate heat transfer of system, anode, cathode and the whole of system are considered as three distinct control volumes, and heat and mass transfer relationships are extracted [14,15]. As noted, according to system description, a heat exchanger is required. For this purpose a double pipe heat exchanger is designed which electrolyte as the warm fluid have streaming in the inner tube and water consider as cooling fluid within the external tube [16]. In order to having a circulating electrolyte stream a proportional pump should be applied.

3.1. Cost model

A mobile alkaline electrolyte fuel cell system requires peripheral equipment such as hydrogen storage tank, circulating pump to provide the electrolyte driving force, heat exchanger and series of additional process such as hydrogen production. So in addition to the fuel cell cost, there are other equipments that should be considered. Thus, if consider the computing for 1000 hours annual performance, five years of application, and 15% inflation rate, with determining costs equation and set values also using the equations of heat transfer section and the heat exchanger design, it could be possible to optimize the overall system performance. For this purpose, GAMS code was developed, using heat transfer, heat exchanger design and the cost model equations the aim to minimize required cost to obtain the optimal heat exchanger area, rate of input and output flows and temperatures in the heat exchanger.

If design and calculation steps collect in an algorithm and associate them with each other, algorithm of Fig.4 will be obtained:

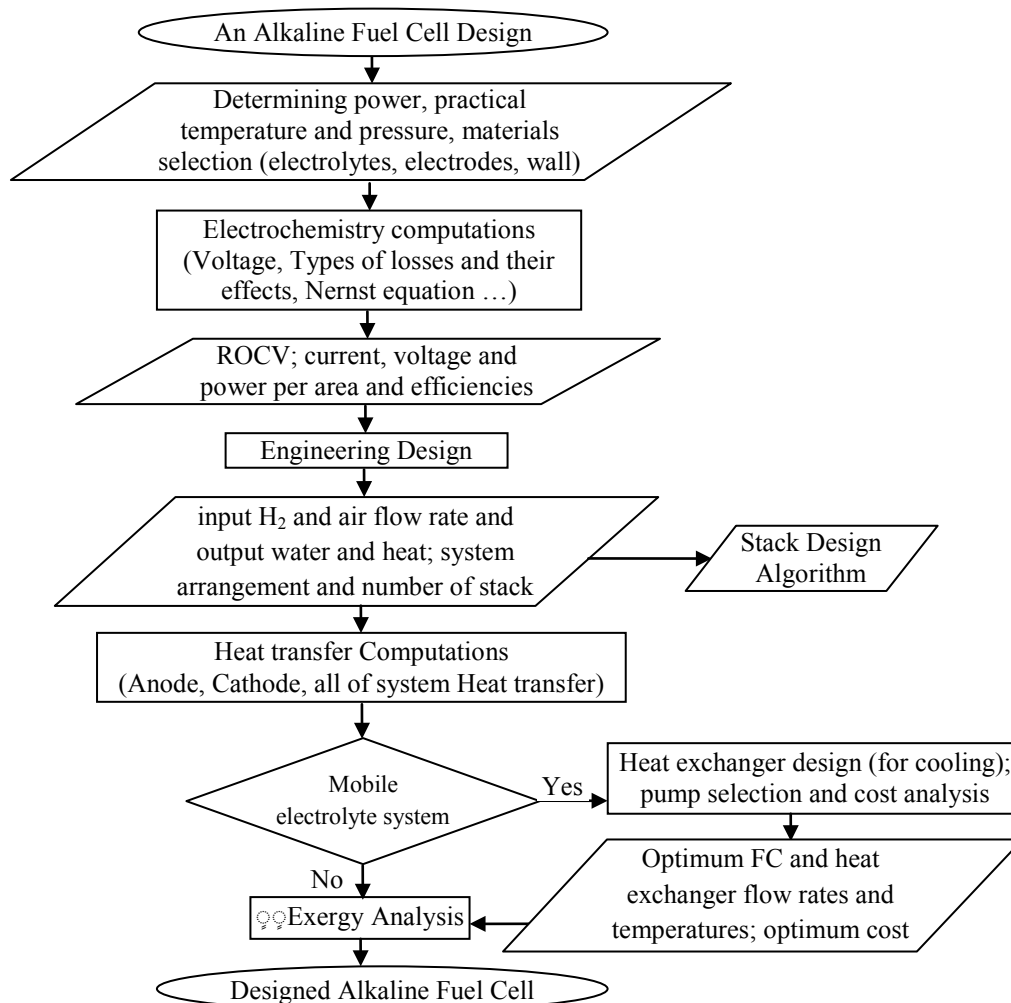


Fig. 4. Main steps of system design algorithm

4. Results

The results of electrochemical section and codes are presented in Table 1 and Fig.5 :

Table 1. Optimum electrochemical results

Voltage (V)	Current Density (mA/cm ²)	Power (mW/cm ²)
0.566	574.316	325.19

Required area for desired power is 308cm². Relation between voltage and current density [17, 18] is affected by irreversibilities and when cell current [19] increases, voltage of cell drops [20] because of activation, ohmic and mass transfer losses.

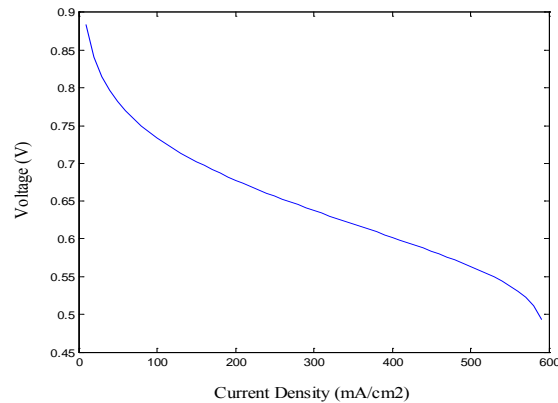


Fig.5. Voltage-Current graph

Designed system performance is presented in Table 2.

Table 2. Amount of efficiencies

Ideal thermodynamic efficiency	Actual thermodynamic efficiency	Electrical efficiency
80%	38%	34%

In engineering design step inlet and outlet flow rates are calculated as Table 3.

Table 3. Electrochemical flow rates

Hydrogen	Oxygen	Inlet air	Outlet air	Produced water
1.85×10^{-6}	1.48×10^{-5}	1.26×10^{-4}	1.12×10^{-4}	1.65×10^{-10} (kg/s)

Also it is concluded that for 100W power, overall 263W energy is generated. So it is seen that power to overall energy ratio is exactly 38%; and this is equal with calculated actual thermodynamic efficiency. Estimated cost for designed system in five years of operation is 2560 \$. Obtained temperature, required area and flow rates in optimal mode are as Table 4:

Table 4. Optimum temperature, required area and flow rates

Electrolyte inlet to heat exchanger and outlet of cell temperature	40 (°C)
Mass flow rate of electrolyte	1.6×10^{-4} (Kg/s)
Electrolyte outlet of heat exchanger and inlet to cell temperature	73 (°C)
Cold fluid mass flow rate (Water)	2.827×10^{-4} (Kg/s)
Cold fluid outlet temperature (Water)	25 (°C)
Area of heat exchanger	0.07 (m ²)
Pressure drop	5.2×10^{-4} (Pa)
Total Heat rate	121.7 (W)

The performance of cell is under influence of different factors, such as temperature. In order to peruse the effect of temperature on cell and all of system (cell and peripheral equipment), the graphs of difference efficiencies toward temperature are depicted in Fig.6. It is found that

because of reducing sensitivity of total system toward temperature with existing cooling section, its gradient is less than ideal performance of cell.

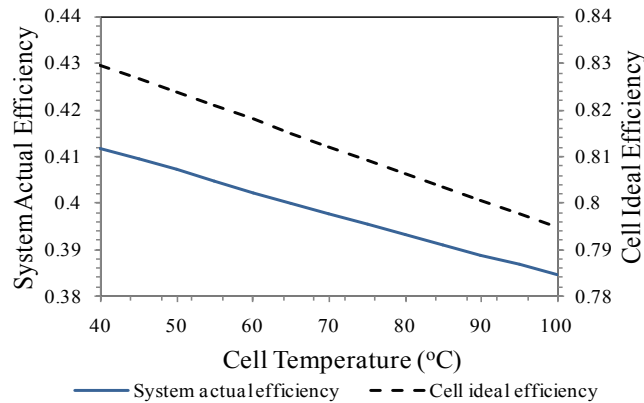


Fig. 6. Difference efficiency toward performance temperature

Nether graph is depicted to survey the effect of parameters variations toward electrolyte outlet temperature from AFC. As seen in Fig.7, with increasing temperature, flow rate of electrolyte and its pressure drop that depend on circulating flow rate, moreover the actual efficiency of system, are decreased. However, required heat exchanger area increases; because it should cool the warmer electrolyte. The minimum value of system total cost, which is obtained from system optimization GAMS codes, has been shown in this graph.

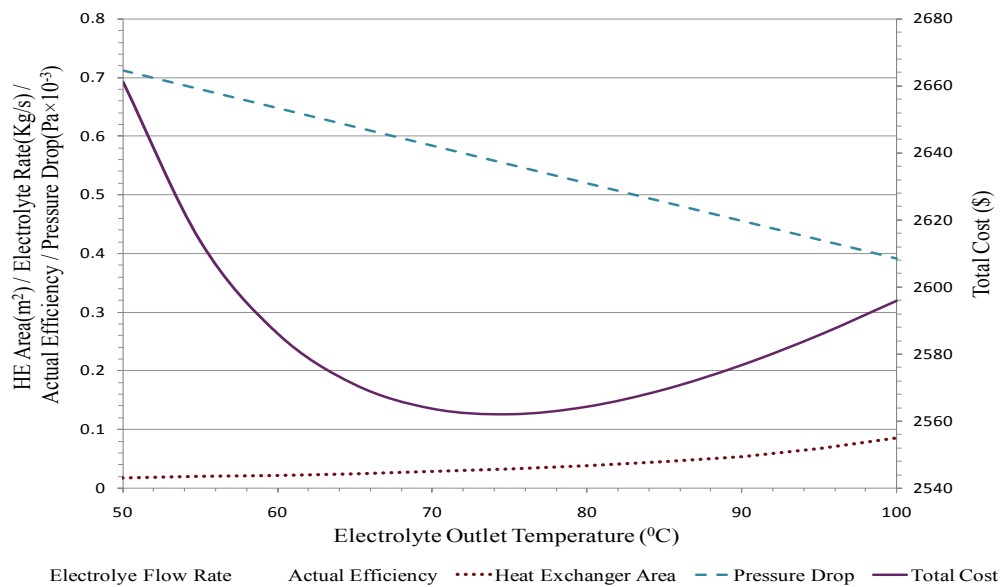


Fig. 7. Change of parameters toward electrolyte outlet temperature

Considering the gradient of cost in Fig.7, by temperature reducing before minimum cost, increasing of cost is more strongly; But after minimum cost by rising of temperature cost increasing is milder; And this suggests that circulating system is more effective than cooling system on total cost (Fig.8 confirm this matter, too).

Fig.8 is depicted to survey parameters variations toward electrolyte inlet temperature to AFC. As seen, with increasing temperature, flow rate of electrolyte and its pressure drop increase; because the electrolyte with increasing the circulation rate can compensate additional heat. Similar to Fig.7, increasing temperature of cell has led to decrease the actual efficiency of

system. Also required heat exchanger area is decreased; because it does not need to cool electrolyte to lower temperature and it needs lesser area.

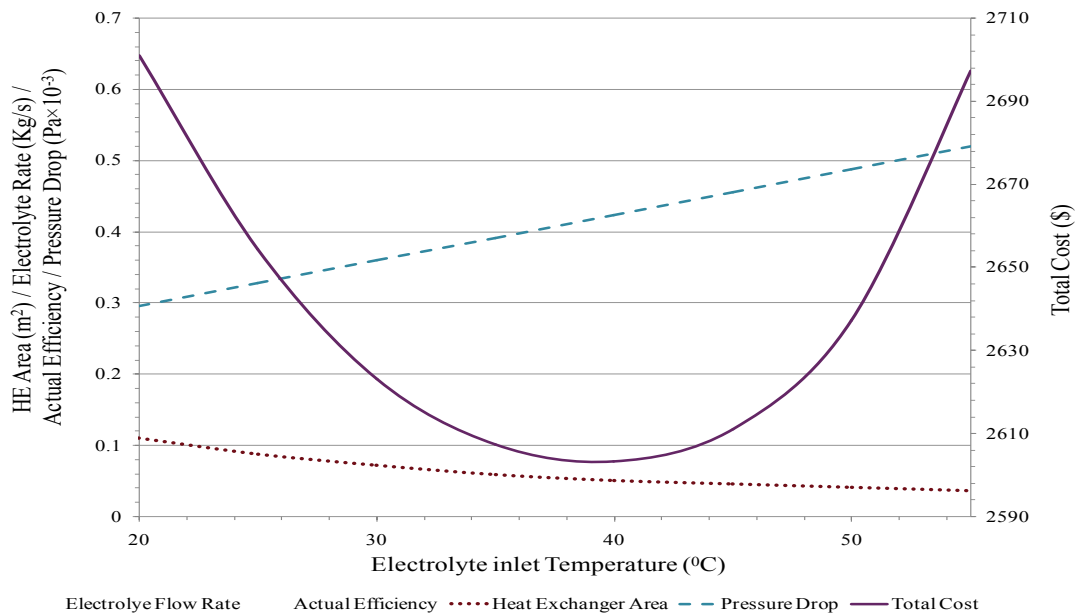


Fig. 8. Change of parameters toward electrolyte inlet temperature

According to the influential parameters plotted in the graphs and change quantities, from it is seen quality viewpoint that priority of items that effect the composite AFC system are for electrolyte pressure drop, electrolyte flow rate and heat exchanger area, respectively and two first items are running cost type, and third item is fixed cost type.

In Fig.7 and Fig.8, the effect of electrolyte input and output temperatures have been evaluated, hence with combining them the effect of ΔT changes can be deduced. Except actual efficiency of system, the changes sense is same with flow rate, pressure drop, heat exchanger area at all values, and also with total cost before and after the minimum point.

5. Conclusions

In the presented research, a 100W alkaline fuel cell with mobile electrolyte and its peripheral equipment have been designed in determined steps to achieve a design model. Presented model has been optimized using GAMS codes to find optimum values of cost model, electrochemical and heat transfer equations.

It was concluded that electrolyte flow rate and its inlet and outlet temperatures, pressure drop, heat exchanger area are some of parameters that effect on cell performance and total cost. Also the efficiency of system reduces toward temperatures rising.

Change of total cost is more sensitive toward input electrolyte temperature rather than output electrolyte temperature. Because input flow controls by peripheral systems; but outlet temperature is a function of fuel cell operation.

Also it was found that running cost is more effective parameter than the fixed cost, in the total cost of systems with similar capacity.

References

- [1] J. Larminie, A. Dicks, Fuel Cell Systems Explained, Second Edition, 2002.

- [2] M.C. Williams, EG&G Technical Services, Fuel Cell Handbook, Seventh Edition, 2004.
- [3] E. Brillas, F. Alcaide, P. Cabot, A small-scale flow alkaline fuel cell for on-site production of hydrogen peroxide, *Journal of Electrochimica Acta*, 2002.
- [4] M. Shen, K. Scott, Power loss and its effect on fuel cell performance, *Journal of Power Sources*, 2005.
- [5] H. ghadamian, Quantitative analysis of irreversibilities causes voltage drop in fuel cell (simulation & modeling), *Journal of Electrochimica Acta*, 2004.
- [6] N. Sammes , *Fuel Cell Technology*, 2006.
- [7] F. Bidault, D.J.L. Brett, P.H. Middleton, N. Abson, N.P. Brandon, A new application for nickel foam in alkaline fuel cells, *Journal of Hydrogen Energy*, 2009.
- [8] M. Schulz, E. Gulzow, G.Steinhilber , Activation of nickel-anode for alkaline fuel cells, *Journal of applied surface science*, 2001.
- [9] G.F. McLean *, T. Niet, S. Prince-Richard, N. Djilali, An assessment of alkaline fuel cell technology, *Journal of Hydrogen Energy*, 2002.
- [10] C. Siegel, Review of computational heat and mass transfer modeling in polymer-electrolyte-membrane (PEM) fuel cells, *Journal of Energy*, 2008.
- [11] J. Holman, *Heat Transfer*, ninth Edition, 2002.
- [12] M.W. Davis, Proposed Testing Methodology and Laboratory Facilities for Evaluating Residential Fuel Cell Systems, 2002.
- [13] F. Barbir, *Fuel cell stack design principles with concepts of micro-mini fuel cells*, 2008.
- [14] R.E. Sonntag, C. Borgnakke, G.J. Van Wylen, *Fundamentals of Thermodynamics*, Sixth edition, 1973.
- [15] I. Verhaert, M.D. Paepe, G. Mulder, Thermodynamic model for an alkaline fuel cell, *Journal of Power Sources*, 2009.
- [16] E.A.D. Saunders, *Heat Exchangers (Designing for heat transfer)*, 1988.
- [17] Yu. G. Chirkov, V. I. Rostokin, Alkaline fuel cells: calculating and comparing overall currents of hydrophobized cathodes with thin regular-structure and thick stochastic-structure active layers, *Russian Journal of Electrochemistry*, 2008.
- [18] P. Gouérec, L. Poletto, J. Denizot, E. Sanchez-Cortezon, J.H. Miners, The evolution of alkaline fuel cells with circulating electrolyte, *Journal of Power Sources*, 2004.
- [19] X.H. Wang, Y. Chen, H.G. Pan, R.G. Xu, S.Q. Li, L.X. Chen, C.P. Chen, Q.D. Wang, Electrochemical properties of $Ml(NiCoMnCu)_5$ used as an alkaline fuel cell anode, *Journal of Alloys and Compounds*, 1999.
- [20] J.H. JO, S.K. MOON and S.C. YI, Simulation of influences of layer thicknesses in an alkaline fuel cell, *Journal of Applied Electrochemistry*, 2000.